CHALMERS
UNIVERSITY OF TECHNOLOGY

Pre-sizing of cooling systems for hybrid-electric aircraft

Knowledge based design tool development

Master's thesis in Mobility Engineering

Oskar Lankamer

DEPARTMENT OF MECHANICS AND MARITIME SCIENCES
CHALMERS UNIVERSITY OF TECHNOLOGY
Gothenburg, Sweden 2025
www.chalmers.se

Master's Thesis in Mobility Engineering

Pre-sizing of cooling systems for hybrid-electric aircraft

Knowledge based design tool development

OSKAR LANKAMER

CHALMERS
UNIVERSITY OF TECHNOLOGY

Department of Mechanics and Maritime Sciences
Division of Fluid Dynamics
Chalmers University of Technology
Gothenburg, Sweden 2025

Pre-sizing of cooling systems for hybrid-electric aircraft
Knowledge based design tool development
Oskar Lankamer

Supervisor: Alain Cuenca, Heart Aerospace AB
Examiner: Carlos Xisto, Department of Mechanics and Maritime Sciences

Master's Thesis 2025
Department of Mechanics and Maritime Sciences
Chalmers University of Technology
SE-412 96 Gothenburg
Sweden
Telephone +46 31 772 1000

Cover: Heart X1 aircraft

Typeset in LaTeX
Gothenburg, Sweden 2025

Pre-sizing of cooling systems for hybrid-electric aircraft
Knowledge based design tool development
OSKAR LANKAMER

Department of Mechanics and Maritime Sciences
Division of Fluid Dynamics
Chalmers University of Technology

Abstract

Hybrid-electric and electric aircraft offer both a solution to the decarbonization of the air-travel sector and a significant challenge for engineers to make them feasible. Component requirements for such aircraft often do not align with what is currently available on the market, necessitating rapid advances in technologies and numerous design iterations.

The cooling-system pre-sizing tool developed during this work aims to serve as the backbone of a Thermal Management System design routine that can be integrated into a larger Multidisciplinary Design Optimization (MDO) network. Besides sizing, it provides estimations of heat transfer, cooling drag, weight, and coolant parameters for a ram-air liquid-cooled system based on component models of various fidelity.

The core of the tool consists of a one-dimensional flow solver and an integral compact heat-exchanger model that analyses user-specified boundary parameters, coupled with three design-optimization algorithms: parametric design-space sweep, genetic algorithm, and SLSQP. In a typical run the routine evaluates about 1 000 designs per 25 s, while the integral heat-exchanger model exhibits a mean absolute percentage error of 1.5 – 7.4 % depending on the flow regime, empowering conceptual design.

Furthermore, CFD-based surrogate models that account for the radiator's influence on the flow inside the preceding diffuser were developed and integrated into the design routine as an approach to increase the fidelity of pre-sizing without continuous CFD.

Finally, the tool was applied to a realistic example of the type-certified aircraft, Pipistrel Velis Electro, to compare its current design with the design from the pre-sizing routine.

Keywords: aircraft cooling, thermal management system, design optimization, pre-sizing tool, hybrid-electric aircraft, surrogate models, cfd

Preface

This report presents the outcome of my master's thesis project carried out at the Department of Mechanics and Maritime Sciences at Chalmers University of Technology in collaboration with Heart Aerospace AB, between February and June 2025.

Acknowledgements

Alain Cuenca, for his unwavering support and insightful project supervision.

Carlos Xisto, for his clear guidance throughout the thesis process and for being an inspiring aerospace-engineering educator at Chalmers.

HA Flight Science Team, for their generous support, the welcoming atmosphere, and the many stimulating conversations and meetings.

Oskar Dahl, for granting access to the Pipistrel Velis Electro aircraft and its flight data.

Oskar Lankamer, Gothenburg, June, 2025

List of Acronyms

Below is the list of acronyms that have been used throughout this thesis listed in alphabetical order:

BMS	Battery Management System
CFD	Computational Fluid Dynamics
ECS	Environmental Control System
GA	Genetic Algorithm
HA	Heart Aerospace
HE	Heat Exchanger
MDO	Multidisciplinary Design Optimization
SLSQP	Sequential Least Squares Quadratic Programming
TMS	Thermal Management System

Nomenclature

Below is the nomenclature of indices, sets, parameters, and variables that have been used throughout this thesis.

Indices

in	Index for parameters at the component inlet
out	Index for parameters at the component outlet
c	Index for the cold fluid parameters (air)
h	Index for the hot fluid parameters (coolant)
f	Index for the fin parameters
t	Index for the tube parameters
∞	Free-flow conditions

Parameters and variables

Roman symbols

A	Surface area used as the reference for U [m^2]
$A_{\mathrm{fr,H}}$	Projected frontal area of one header tank [m^2]
$A_{\mathrm{fr,HE}}$	Frontal area of the core exposed to the air stream [m^2]
$A_{\mathrm{fr},f}$	Frontal area of one fin sheet [m^2]
$A_{c,f}$	Free-flow area through one fin passage [m^2]
$A_{c,\mathrm{H}}$	Flow area available inside all header ports [m^2]
$A_{c,\mathrm{HE}}$	Sum of all flow gaps (free-flow area) in the core [m^2]
$A_{\mathrm{c,t}}$	Flow cross-sectional area of one tube [m^2]
A_f	Heat-transfer surface area of one fin sheet [m^2]
A_{HE}	Total air-side heat-transfer surface area of the core [m^2]

$A_{\mathrm{surf,t}}$	Internal wetted surface area of one tube [m^2]
B	Plate spacing between adjacent fin sheets (fin height) [m]
C	Heat-capacity rate ($C = \dot{m}\, c_p$) [$\mathrm{W\,K^{-1}}$]
C_r	Capacity ratio $C_{\min}/C_{\max}$ [–]
C_{ij}	Inertial loss coefficient (Darcy–Forchheimer) [–]
D	Characteristic length scale (e.g. diameter) [m]
D_h	Hydraulic diameter $4A_{flow}/P_{wet}$ [m]
D_{ij}	Friction loss coefficient (Darcy–Forchheimer) [–]
G	Mass flux [$\mathrm{kg\,m^{-2}\,s^{-1}}$]
H_{core}	Outside height of the fin-tube matrix [m]
I	Turbulence intensity (r.m.s. fluctuations / mean) [–]
L	Tube length between header plates (flow length) [m]
ℓ	Turbulent length scale [m]
L_{core}	Core length between header tanks [m]
NTU	Number of heat-transfer units $AU/C_{\min}$ [–]
N_f	Total number of fin sheets in the core [–]
$N_{fins/\mathrm{tube}}$	Number of fin sheets per tube row [–]
N_{t}	Number of tube rows/columns stacked in the core [–]
Nu	Nusselt number $h4r_h/k$ [–]
Pr	Prandtl number $\mu c_p/k$ [–]
P_k	Production rate of turbulent kinetic energy [$\mathrm{kg\,m^{-1}\,s^{-3}}$]
Re	Reynolds number GD_h/μ [–]
St	Stanton number $h/(Gc_p)$ [–]
S_{ij}	Components of the mean strain-rate tensor [$\mathrm{s^{-1}}$]
T	Static temperature [K]
T_t	Total (stagnation) temperature [K]
V	Local velocity [$\mathrm{m\,s^{-1}}$]
V_f	Flow volume associated with one fin sheet [m^3]
V_{t}	Internal volume of one tube [m^3]
a	External height of a flat tube (z-axis) [m]
a_i	Internal flow height of the tube [m]
c_p	Specific heat at constant pressure [$\mathrm{J\,kg^{-1}\,K^{-1}}$]
f	Fanning friction factor [–]
h	Convective heat-transfer coefficient [$\mathrm{W\,m^{-2}\,K^{-1}}$]

j	Colburn j-factor [–]
k	Thermal conductivity of fluid [$\mathrm{W\,m^{-1}\,K^{-1}}$]
$\dot{m}$	Mass-flow rate [$\mathrm{kg\,s^{-1}}$]
m_c	Fin constant, cold side [$\mathrm{m^{-1}}$]
m_h	Fin constant, hot side [$\mathrm{m^{-1}}$]
n_{seg}	Number of uninterrupted fin segments per sheet [–]
p	Static pressure [Pa]
p_f	Fin pitch (centre-to-centre distance) [m]
p_t	Total (stagnation) pressure [Pa]
q''	Heat flux (heat flow per unit area) [$\mathrm{W\,m^{-2}}$]
q'''	Volumetric heat-generation rate [$\mathrm{W\,m^{-3}}$]
$r_{h,\mathrm{t}}$	Hydraulic radius of the tube [m]
t	Core thickness (equals tube width w) [m]
$t_{c,\mathrm{in}}$	Cold-fluid inlet temperature [K or °C]
$t_{c,\mathrm{out}}$	Cold-fluid outlet temperature [K or °C]
$t_{h,\mathrm{in}}$	Hot-fluid inlet temperature [K or °C]
$t_{h,\mathrm{out}}$	Hot-fluid outlet temperature [K or °C]
v_m	Mean specific volume (core-averaged) [$\mathrm{m^3\,kg^{-1}}$]
w	External width of a flat tube (core thickness) [m]
w_i	Internal flow width of the tube [m]
x	Volumetric flow rate ($x = VA_{\mathrm{fr}}$) [$\mathrm{m^3\,s^{-1}}$]

Greek symbols

α^*	Aspect ratio of the internal duct a_i/w_i [–]
β_f	Specific surface area between plates [$\mathrm{m^2\,m^{-3}}$]
β_{t}	Specific surface area of the tube [$\mathrm{m^{-1}}$]
ε (fluids)	Turbulent dissipation rate of kinetic energy [$\mathrm{m^2\,s^{-3}}$]
ε (thermal)	Surface emissivity (emission/black-body ratio) [–]
$\eta_{f,c}$	Fin effectiveness, cold side [–]
$\eta_{f,h}$	Fin effectiveness, hot side [–]
$\eta_{0,c}$	Overall surface efficiency, cold side [–]
$\eta_{0,h}$	Overall surface efficiency, hot side [–]
μ	Dynamic viscosity [Pa s]
μ_t	Turbulent (eddy) viscosity [Pa s]

ν	Kinematic viscosity (μ/ρ) [$\mathrm{m^2\,s^{-1}}$]
σ	Stefan–Boltzmann constant (5.67×10^{-8} W $\mathrm{m^{-2}\ K^{-4}}$)
σ_k	k-equation turbulent-model constant [–]
σ_f	Fin porosity (free-flow/frontal) [–]
σ_{H}	Header porosity (free-flow/frontal) [–]
σ_{HE}	Core porosity (free-flow/frontal) [–]
σ_{t}	Tube porosity (free-flow/frontal) [–]
τ_f	Fin area ratio (fin area/total) [–]
τ_{t}	Fraction of perimeter on the long sides of the tube [–]
Δf	Thickness of a single fin sheet t_f [m]
$\Delta tube$	Tube wall thickness t_w [m]

Contents

List of Figures

List of Tables

1

Introduction

This master's thesis is a collaboration between Chalmers University of Technology and Heart Aerospace (HA). HA is a Swedish company focused on developing an innovative regional hybrid-electric aircraft to help reduce emissions from air travel [7]. Due to the payload penalty imposed by the current technological limitations of batteries, achieving an excellent aerodynamic design with minimal drag is essential to maximizing the electric range of such aircraft and enhancing its sustainability. One of the systems that can be optimized for drag reduction is the cooling system. A well-designed cooling system not only contributes to lowering the aircraft's drag but also helps minimize its weight. One of the main challenges is that no aircraft with this type of propulsion (parallel hybrid electric) has yet been certified in the CS-25 segment, which accounts for more than 95% of aviation-related CO_2 emissions [3]. Developing effective design methodologies, tools, and guidelines, while also reducing the design iteration time for the cooling system, directly contributes to the advancement of sustainable aviation.

1.1 Background

Due to globalization, creeping climate change, and the increasing demand for resources, the European Commission has set a goal to reduce air transport emissions through the establishment of Flightpath 2050 proclaiming 65% noise reduction, 75% CO2 reduction and 90% NOX reduction [1]. While it remains an important historical and conceptual reference for decarbonization efforts, new frameworks have been developed to build upon it. Recently updated roadmap to achieve this goal is a revised version of Destination 2050, issued by the Royal Netherlands Aerospace Centre (NLR). This report states that reaching net-zero emissions by 2050 is still possible (as of February 2025), but it requires immediate action from both industry and policymakers. Without decisive efforts, achieving decarbonization within the set time frame will become increasingly difficult and, eventually, impossible, as visible in the Figure 1.1 [2].

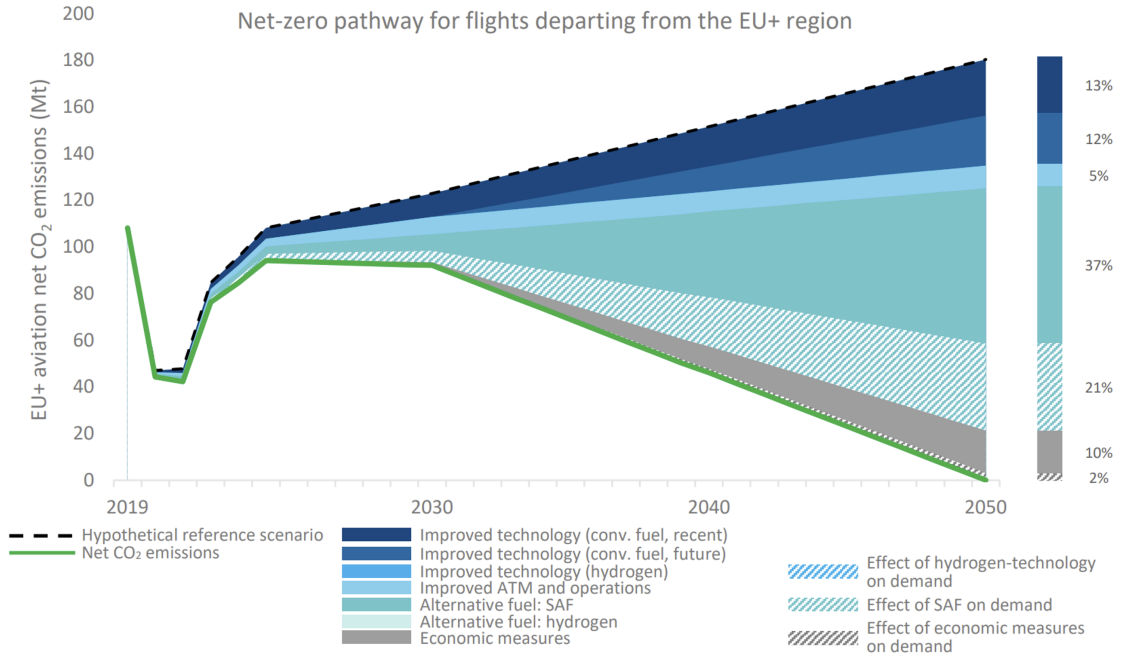

Figure 1.1: Impact of intercontinental flight from the EU+ region between 2019 and 2050 considering possible sustainability measures and their impact on the path to net-zero. [1]

Among other technologies, such as sustainable aviation fuel (SAF) and hydrogen propulsion, hybrid-electric aircraft with battery-powered engines could serve as a stepping stone toward aviation decarbonization. This is because the technological readiness of purely electric propulsion is relatively high compared to hydrogen, and SAF is not entirely emission-free.

Hybrid-electric propulsion (HEP) is particularly feasible for short-range flights of approximately 400 km [11] which contributes to around 6% of passenger aircraft CO_2 emissions [10] which doesn't make it simple solution to the problem of decarbonization. It has recently been reconsidered for longer ranges and larger aircraft by challenging misconceptions in electric aircraft design [5, 6]. That being said, significant breakthroughs are still needed to enhance the potential of this configuration, particularly in improving the volumetric energy density (watt-hours per cubic meter) and gravimetric energy density (watt-hours per kilogram) of batteries as it is the main problem of this aircraft concept [12].

While each component of a Hybrid Electric Propulsion (HEP) system—such as high-efficiency electric motors and advanced battery modules—is designed for optimal performance, integrating them introduces complex thermal management challenges. Engineers must develop a cooling architecture that efficiently dissipates the significant waste heat generated during various flight phases, using effective heat transfer methods like conduction, convection, and radiation. This task is further complicated by the need to minimize overall system weight while adhering to stringent aviation safety standards and reduced amount of conventional fuel that is used as a coolant

in traditional TMS.[15]
Figure 1.2 contains an overview of the TMS technologies. While there are many solutions available to consider, many of them are not at technological readiness level (TRL) to be considered in the aircraft that is scheduled to be in service soon.[15]

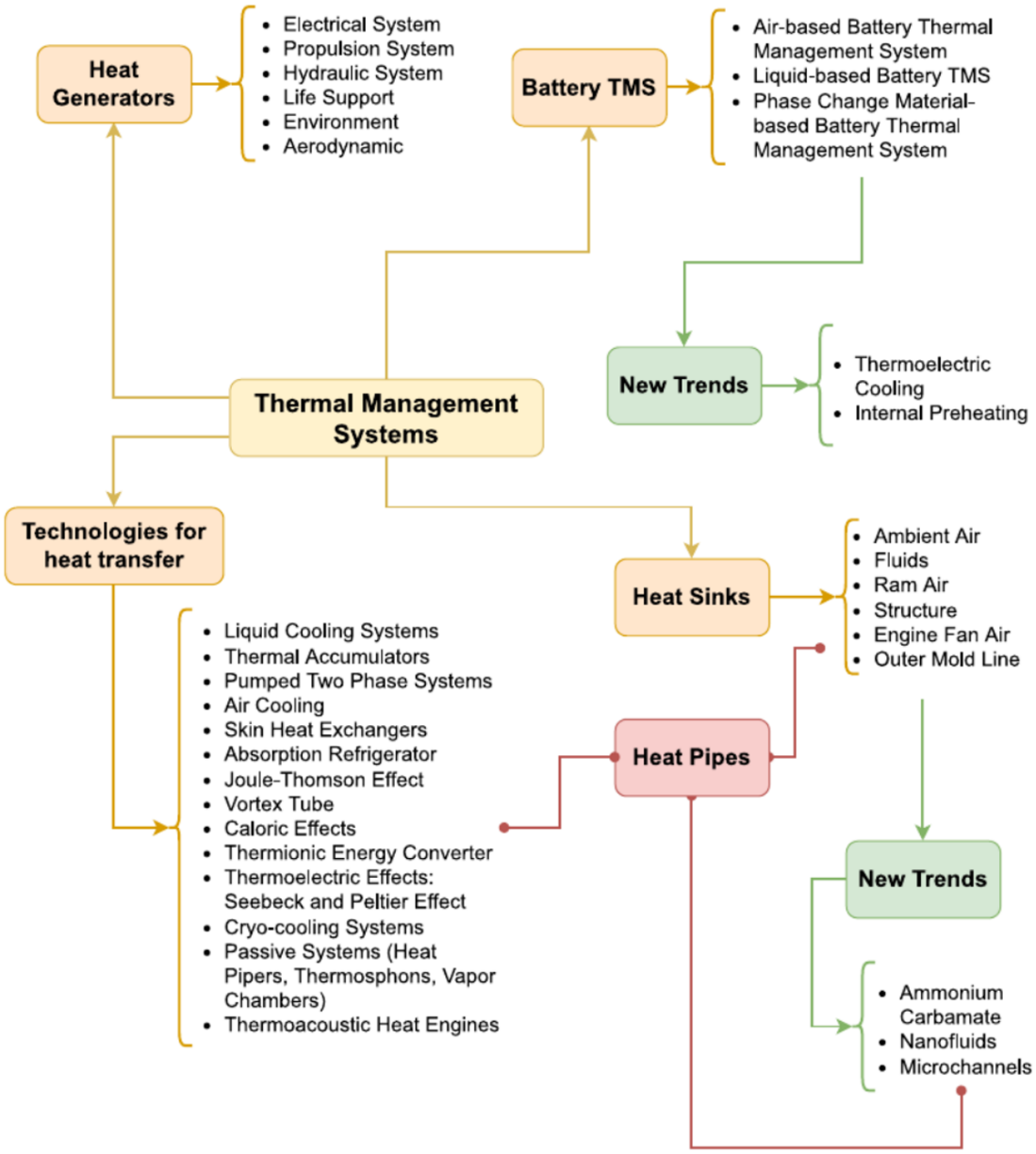

Figure 1.2: TMS solutions and technologies [15]

1.2 Preliminary purpose

In this thesis, the baseline for the components of the cooling system for hybrid-electric aircraft will be the ES-30, developed by Heart Aerospace (HA). The ES-30 features two electric engines that form the electric power unit (EPU), parallel to a pair of turboprop engines, making it an independent hybrid configuration [7]. This

design decreases reliance on the batteries' energy density.

Although the study will be based on data from the currently implemented configuration, potential future configurations will also be considered. This approach aims to make the pre-sizing tool as universal as possible for cooling system design optimization in future hybrid-electric aircraft concepts, which are continuously evolving.

The cooling system will use a two-stage approach. First, critical components are cooled using a liquid coolant, such as water-glycol, engine oil, or fuel, that absorbs heat directly from the components through direct contact or via an indirect method like a coldplate design. Water, in particular, offers excellent thermophysical properties with a specific heat capacity about four times that of air, allowing for compact and efficient heat extraction [15]. Once the coolant has absorbed the excess heat, it is then passed through a ram air cooling stage, where ambient air, drawn in by the aircraft's forward motion, dissipates the stored heat. Example of such cooling loop is presented in the Figure 1.3

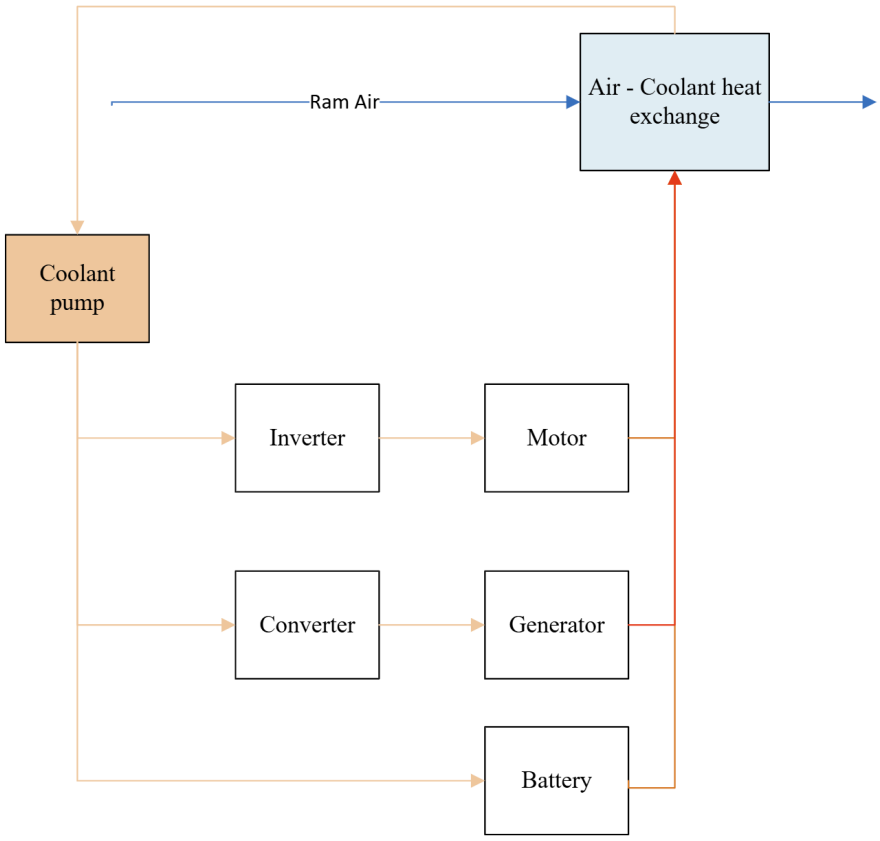

Figure 1.3: Example of ram air, liquid-cooling system. Adapted from [16].

1.2.1 TMS for Future Aircraft

Increased performance of the future aircraft goes in pair with increased heat generation and higher requirements from the cooling systems.

Heat sources

The principal contributor is the gas turbine where friction, compression and combustion increase hardware temperature. During an engine acceleration as much as thirty per cent of the additional fuel energy may be absorbed by casings and discs through heat soakage [13]. Electrified power trains add concentrated low-grade loads that arise in converters, motors and battery packs. Further heat arrives from avionics, environmental control packs and mission equipment. Together these sources push total waste energy toward the megawatt range on advanced platforms [13].

Heat acquisition mechanism

Energy leaves the source through forced oil or air convection, conduction via cold plates or direct liquid impingement on electronic surfaces. The selection depends on allowable component temperature, available pressure head and packaging space. Every method must withdraw heat quickly while limiting the penalty in mass and pumping power [13].

Thermal transport means

After removal the energy travels through networks of pipes, tanks and rotating machinery. Single-phase liquid loops provide high volumetric capacity for long routes. Two-phase or Rankine based cycles lift heat above sink temperature when required. Demonstrator programmes already combine pumps, micro-channel exchangers and phase-change buffers to accept peak loads without oversizing the steady state hardware [13].

Heat rejection mechanisms

Ram-air heat exchangers remain the dominant devices on civil aircraft because outside air offers large thermal capacity during cruise. If altitude or mission restricts ram heat transfer designers employ fuel-cooled oil coolers, skin mounted panels or active refrigeration packs. The rejection unit sets both drag rise and final approach temperature to the sink, hence its sizing drives overall efficiency [13].

Heat sinks

Ambient air, fuel and structure act as terminal sinks. High altitude air is attractive thanks to low static temperature yet demands additional inlet area which increases drag. Fuel absorbs considerable energy and can improve combustion when preheated but is limited by coking. The airframe supplies transient buffer mass although its benefit declines with wider use of composites [13].

Heat sinks

Current research highlights six drivers that challenge conventional layouts: hybrid electric propulsion, ultra-high bypass geared turbofans, high power military sensors and weapons, environmental control systems, integrated power and thermal architectures and supersonic transports that face severe aerodynamic heating. Each driver enlarges or redistributes heat loads and therefore motivates lighter materials, novel exchanger geometries and integrated models [13].

1.2.2 Integrated TMS for HEP

Hybrid electric propulsion converts the thermal design task into a multi-variable optimisation problem that links mass, drag, power demand and reliability. Electric machines, power electronics and batteries release dense heat fluxes that can reach several hundred kilowatts during climb. A competitive system must dispatch this energy to the sinks while adding minimal structural weight and cooling drag [14].

Architecture and layout

Two philosophies are reported in the literature. A centralised scheme channels all waste heat to a single high capacity exchanger which simplifies control but raises frontal area. A decentralised arrangement splits the network into separate branches for batteries, motor drives and environmental packs. This reduces local pipe length and permits staggered operation although it introduces extra pumps and valves. One study that separated battery and motor loops reported a ram-air exchanger mass that was reduced to one fifth of the baseline value because the battery acted as a thermal buffer during transients [14].

Weight drivers

Mass is concentrated in pumps, blowers, heat exchangers and pipework. Adding redundancy lifts component count and has been predicted to increase system weight by about twenty per cent. Micro-channel cores, additive manufactured manifolds and lightweight electric fans promise double digit savings. Every kilogram removed from the loop cuts structural reinforcement and therefore compounds the benefit [14].

Drag and power penalties

Cooling drag rises with the square of ram-air flow rate so inlet and outlet geometry must be considered early in the aircraft design. Variable exit flaps, ram recovery diffusers and boundary-layer ingestion at the exhaust improve total pressure recovery and can trim drag on climb segments. Pump and fan power draw on the same electrical bus that feeds propulsion which makes their efficiency a direct driver of range [14].

Research needs

Progress requires higher heat transfer per unit mass, smart control strategies that schedule load sharing among loops and reliable characterisation of novel sinks such as fuel tanks with integrated phase-change media. Experimental campaigns should validate digital twins that couple aerodynamics, thermal networks and battery degradation in one framework. Addressing these needs will close the current gap in holistic reviews and support the transition from conceptual studies to flight-ready hybrid electric propulsion [14].

1.3 Goals

The first objective of this thesis is to conduct a literature review of cooling system architectures, considering thermodynamics, internal flow through components, their configurations, and integration. Schematic model of the cooling system will be developed to simulate it in terms of heat rejection and aerodynamic drag. This model will then be further extended by incorporating CFD-based surrogate models for some of the components, capturing their aerodynamic characteristics.

Final outcome is the tool that can pre-size the cooling system, considering its drag, heat transfer weight and volume, using those synthesized analytical, empirical and surrogate models while providing design curves for the engineer. Its main role is to speed up conceptual design process that requires many iterations, with compliance to the Multidisciplinary Design Optimization (MDO) philosophy that is on a steady rise, especially in aerospace industry [24] where a lot of tweakable parameters interfere with each other during design.

1.4 Limitations

The study focuses exclusively on subsonic flow. The baseline configuration driving the purpose of the thesis is a regional hybrid electric aircraft, and most of the times, compressibility effects are neglected. Consequently the methodology cannot be extended to transonic cooling systems without implementing compressible flow corrections.

Instead of modeling transient heat generation for each individual component such as the battery, the EPU and the gas turbine, a single aggregate, steady-state heat rejection value is used as the objective function.

The fidelity of the models is limited by the lack of empirical data, and crucial components level validation is emphasized over full system validation at this level of development. In fact, due to the broad scope of the thesis and the need to establish the whole tool from scratch, it was only possible to conduct validation of the radiator model (allowing for real heat rejection estimations) and trumpet diffuser (to create surrogate model coupled with heat exchanger).

Multiphysics simulations such as CFD with comprehensive heat transfer or advanced spectral turbulence models are omitted, being not in the scope of this study.

1.5 Tool overview

Pre-sizing tool has been developed as an objective based code with component classes that contain their internal physical behavior inside their own unique methods and constructor. Each component takes in flow parameters, like total pressure, static pressure, mean velocity and other, further described in the Chapter 3, and outputs the flow state at the outlet based on the isentropic relations. Logic of this 1D flow solver is presented in the Figure 1.4. There is no iteration of one 'size' needed due to the pre-determined geometry and internal parameters of all components except the nozzle, which is sized at the end, to reach the outlet mass flow corresponding to the inlet mass flow, and outlet static pressure corresponding to ambient static pressure. Once the single geometry analysis has been established, this routine is connected

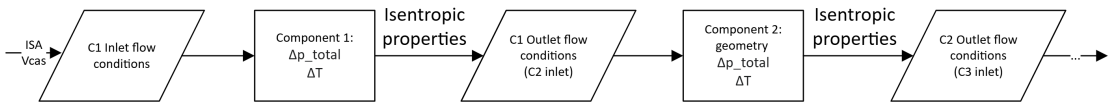

Figure 1.4: Tool's 1D flow solver simplified logic

with various design optimization methods, leading to comparison of the resulting designs from the sweep of geometrical parameters, Sequential Least Squares Programming (SLSQP) gradient-based algorithm and Genetic Algorithm (GA). That comes down to the overall pre-sizing loop visible in Figure 1.5, that can be approached with one of above mentioned methods. Underlying theory and zoom into each of the modeled components and methodologies are presented in Chapters 2 and 3.

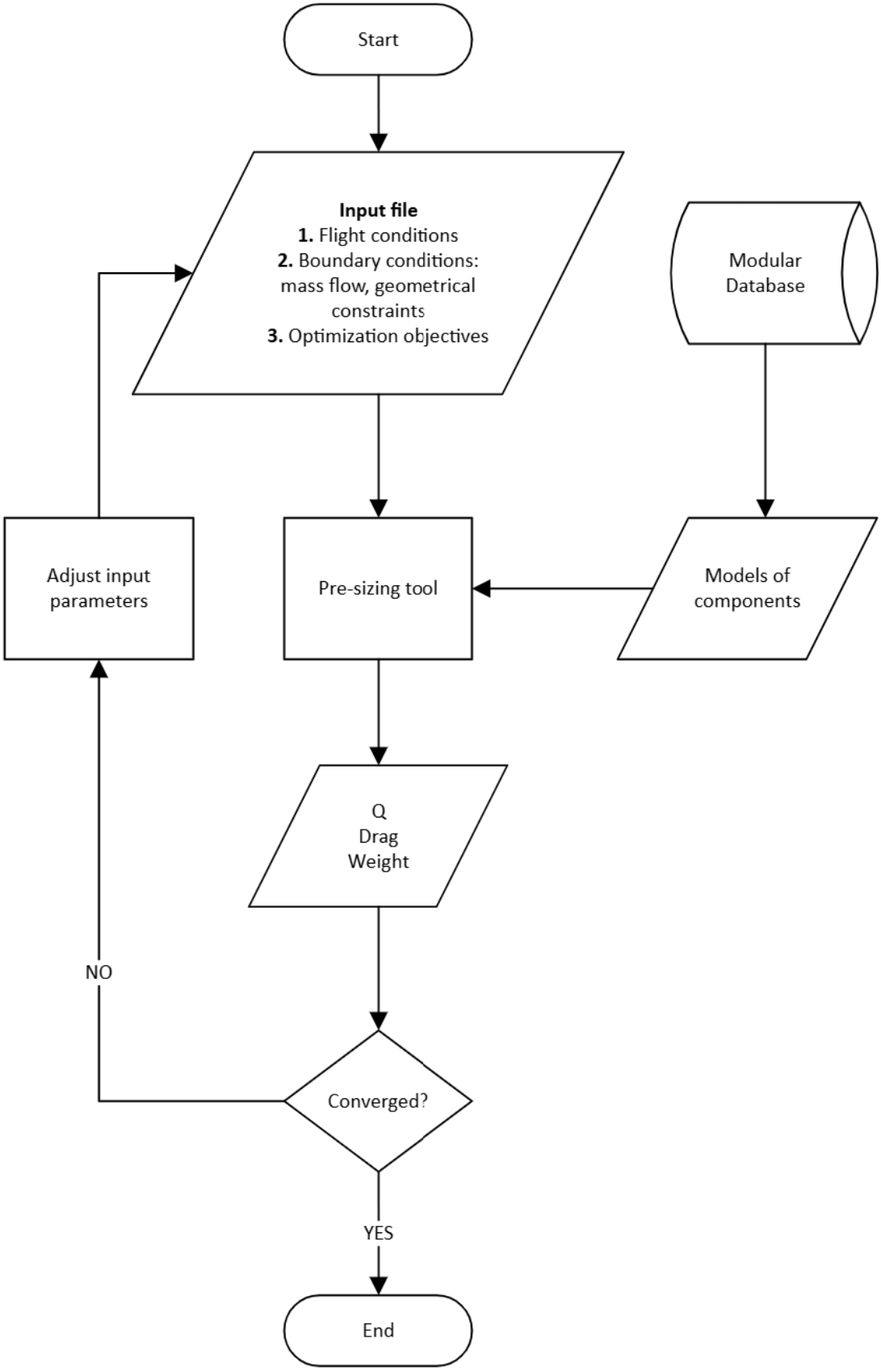

Figure 1.5: Flow chart of the cooling system pre-sizing tool

2

Theory

2.1 Non dimensional numbers

Dimensionless numbers are compact similarity parameters for correlating experimental data and for scaling laboratory results to practical hardware. The present work makes repeated use of the Reynolds, Nusselt, Prandtl and Stanton numbers as defined below based on Rohsenow et al. [25].

2.1.1 Reynolds number

$$\mathrm{Re} = \frac{\rho V D}{\mu} \tag{2.1}$$

The Reynolds number compares inertial and viscous forces. For internal flow the reference length D is taken as the hydraulic diameter D_h while for external flow it is the characteristic body length that governs boundary layer growth. Transition from laminar to turbulent motion occurs near $\mathrm{Re} \approx 2.3 \times 10^3$ in smooth circular tubes and near $\mathrm{Re}_x \approx 5 \times 10^5$ along a smooth flat plate [25].

2.1.2 Nusselt number

$$\mathrm{Nu} = \frac{hD}{k} \tag{2.2}$$

The Nusselt number expresses the ratio of convective to conductive heat transfer across a fluid layer of thickness D. Typical limits illustrate its physical meaning. For fully developed laminar flow inside a tube with uniform wall temperature $\mathrm{Nu} = 3.66$; with uniform wall heat flux $\mathrm{Nu} = 4.364$. For fully developed laminar flow between parallel plates the constant wall temperature limit is $\mathrm{Nu} = 7.541$.Design correlations are often written as the function of Reynolds and Prandtl numbers $\mathrm{Nu} = f(\mathrm{Re}, \mathrm{Pr})$ [25]. A high Nusselt number simply means that convection is far more effective than conduction in transporting heat. In mathematical form:

$$\mathrm{Nu} = \frac{h\,D}{k} \gg 1.$$

In other words, that the convective heat-transfer coefficient h is large compared to the fluid's conductive capacity k/D.

2.1.3 Prandtl number

$$\mathrm{Pr} = \frac{\mu c_p}{k} = \frac{\nu}{\alpha} \tag{2.3}$$

The Prandtl number is the ratio of momentum diffusivity (kinematic viscosity) ν to thermal diffusivity α. Air at ambient conditions has $\mathrm{Pr} \approx 0.7$, water at room temperature has $\mathrm{Pr} \approx 7$ and light lubricating oils may exceed one hundred. When Pr is smaller than unity the thermal boundary layer is thicker than the velocity boundary layer, while the reverse holds when Pr exceeds unity [25].

2.1.4 Stanton number

$$\mathrm{St} = \frac{h}{\rho V c_p} = \frac{\mathrm{Nu}}{\mathrm{Re}\,\mathrm{Pr}} \tag{2.4}$$

The Stanton number measures the fraction of bulk enthalpy transported as heat per unit length of flow development. For turbulent flow over a smooth flat plate in air a useful estimate is $\mathrm{St} = 0.0153\,\mathrm{Re}_x^{-0.25}$ in the range $0.5 < \mathrm{Pr} < 15$ [25]. The Colburn j factor

$$j = \mathrm{St}\,\mathrm{Pr}^{\,2/3}$$

consolidates heat transfer data for many fluids into a single curve that simplifies preliminary design [25].

2.2 Heat Transfer

2.2.1 Mechanisms of heat transfer

Heat is energy that moves because a temperature difference exists. Rohsenow distinguishes three basic modes of transfer [25].

Conduction

Conduction occurs when energy migrates through matter by molecular motion. For steady one-dimensional flow in a plane wall

$$q'' \;=\; -\,k\,\frac{\mathrm{d}T}{\mathrm{d}x}, \qquad \text{(Fourier's law of conduction)} \tag{2.5}$$

where k is the thermal conductivity. In three dimensions the relation is $q'' = -\,k\nabla T$.

Convection

Convection appears when a fluid sweeps across a surface so that

$$q'' \;=\; h\,(T_w - T_\infty), \qquad \text{(Newton's law of cooling)} \tag{2.6}$$

with h the local convection coefficient that links the surface temperature to the conductive gradient in the viscous sub-layer [25].

Radiation

Radiation represents electromagnetic energy emitted by matter at non-zero temperature. A gray surface radiates at $\varepsilon\sigma T^4$ where ε is the emissivity and σ the Stefan Boltzmann constant. Net exchange between two parallel diffuse gray plates is

$$q''_{1\to 2} = \sigma\, F_{1-2}\,(T_1^4 - T_2^4), \tag{2.7}$$

with F_{1-2} the view factor [25]. It's important to mention that many aircraft components experience conduction through the wall together with convection and radiation on the faces. The combination is handled by an additive resistance network. An equivalent radiative coefficient:

$$h_r = \varepsilon\,\sigma\,(T_w + T_\infty)\,(T_w^2 + T_\infty^2) \tag{2.8}$$

allows radiation and convection to be summed in a single overall transfer term [25] but because of this coupling complexity, radiation has been omitted in this work.

2.2.2 Energy conservation

For an incompressible fluid with constant properties the first law expressed for a fixed control volume gives

$$\rho\, c_p\, \frac{\mathrm{D}T}{\mathrm{D}t} = k\,\nabla^2 T + \dot{q}''', \tag{2.9}$$

where ρ is density, c_p specific heat and $\dot{q}'''$ an internal heat source [25]. Viscous dissipation is negligible at the velocities relevant to this thesis. Equation (2.9) supplies the thermal core for the sizing tool that is introduced in later chapters.

2.3 Fluid dynamics

2.3.1 Governing equations

For a Newtonian fluid the conservation statements of continuity and momentum summarised by Malalasekera read [48]

$$\nabla\cdot\,\mathbf{u} = 0, \qquad \rho\,\frac{\mathrm{D}\mathbf{u}}{\mathrm{D}t} = -\,\nabla p + \mu\,\nabla^2\mathbf{u} + \rho\,\mathbf{g},$$

where $\mathbf{u}$ is velocity, p pressure, μ dynamic viscosity and $\mathbf{g}$ body–force density. There are no heat source terms present as the CFD simulations conducted are focused on the flow phenomena in front of the heat exchanger. Nonetheless, it's important to mention that heat transfer into the cold flow has big effect on the aerodynamic performance of the whole system and can increase or decrease drag, dependent on the Mach number at the radiator face. It is so called Meredith effect first covered by Meredith et al. [50]. These governing equations are discretized and solved using Finite Volume Method (FVM) by the ICFD++ software [44].

2.3.2 Turbulence models

Below the critical Reynolds number the motion remains laminar and adjacent fluid layers shear smoothly past one another. Once that threshold is exceeded the flow becomes turbulent, additional Reynolds stresses appear and must be *modelled* rather than resolved [48].

Time–averaging the Navier–Stokes equations introduces six unknown Reynolds stresses that require closure. For the preliminary CFD screening of the diffuser only eddy-viscosity models were considered because they offer a compromise between accuracy and cost.

$k-\varepsilon$ model. The two-equation model of Launder and Spalding solves transport equations for the turbulent kinetic energy k and its dissipation rate ε:

$$\frac{\partial(\rho k)}{\partial t} \;+\; \boldsymbol{\nabla}\cdot(\rho k\,\mathbf{u}) = \boldsymbol{\nabla}\cdot\Big[\Big(\mu + \frac{\mu_t}{\sigma_k}\Big)\,\boldsymbol{\nabla} k\Big] \;+\; P_k \;-\; \rho\,\varepsilon, \tag{2.10}$$

$$\frac{\partial(\rho \varepsilon)}{\partial t} \;+\; \boldsymbol{\nabla}\cdot(\rho \varepsilon\,\mathbf{u}) = \boldsymbol{\nabla}\cdot\Big[\Big(\mu + \frac{\mu_t}{\sigma_\varepsilon}\Big)\,\boldsymbol{\nabla} \varepsilon\Big] \;+\; C_{1\varepsilon}\,\frac{\varepsilon}{k}\,P_k \;-\; C_{2\varepsilon}\,\rho\,\frac{\varepsilon^2}{k}, \tag{2.11}$$

$$P_k \;=\; 2\,\mu_t\,S_{ij}\,S_{ij}, \qquad S_{ij} \;=\; \frac{1}{2}\Big(\frac{\partial u_i}{\partial x_j} \;+\; \frac{\partial u_j}{\partial x_i}\Big) \tag{2.12}$$

The turbulent length scale ℓ is defined by

$$\ell \;=\; C_\mu^{3/4}\,\frac{k^{3/2}}{\varepsilon}. \tag{2.13}$$

In internal ducts it is common to specify an inlet length scale ℓ_{inlet}:

$$\ell_{\text{inlet}} \;=\; 0.07\,D_h. \tag{2.14}$$

Therefore, once k is estimated (for example, from a turbulence-intensity I via

$$k_{\text{inlet}} \;=\; \frac{3}{2}\,(U\,I)^2, \tag{2.15}$$

where U is the mean inlet velocity), the inlet dissipation rate follows as

$$\varepsilon_{\text{inlet}} \;=\; C_\mu^{3/4}\,\frac{k_{\text{inlet}}^{3/2}}{\ell_{\text{inlet}}} \;=\; C_\mu^{3/4}\,\frac{k_{\text{inlet}}^{3/2}}{0.07\,D_h}. \tag{2.16}$$

With C_μ being. Conversely, if $\varepsilon_{\text{inlet}}$ is prescribed, the corresponding turbulent kinetic energy is

$$k_{\text{inlet}} \;=\; \left(\frac{\varepsilon_{\text{inlet}}\,\ell_{\text{inlet}}}{C_\mu^{3/4}}\right)^{2/3} \;=\; \left(\frac{\varepsilon_{\text{inlet}}\,(0.07\,D_h)}{C_\mu^{3/4}}\right)^{2/3}. \tag{2.17}$$

While the k–ε model is robust for free shear layers, it tends to overpredict separation on smooth walls under adverse pressure gradients [48].

The constant C_μ is an empirical model constant in the k–ε closure. It appears in the eddy-viscosity definition:

$$\mu_t \;=\; C_\mu \, \rho \, \frac{k^2}{\varepsilon}\,, \tag{2.18}$$

and was calibrated to reproduce canonical boundary-layer and free-shear-flow data. Its most commonly used value in high-Reynolds-number k–ε implementations is

$$C_\mu \;=\; 0.09. \tag{2.19}$$

In practice, C_μ controls the magnitude of the turbulent viscosity μ_t for given k and ε. A larger C_μ yields higher μ_t (and hence thicker modeled turbulent mixing layers), while a smaller C_μ reduces μ_t. Most textbooks and CFD codes assume $C_\mu = 0.09$.[48]

$k-\omega$ model. Wilcox replaces ε by the specific dissipation rate $\omega = \varepsilon/k$. Because ω is not diffused by viscosity it adapts rapidly near solid walls, giving accurate wall-stress predictions without additional damping functions.[48]

$k-\omega$ SST. The shear-stress-transport blend switches from the original $k-\omega$ formulation in the viscous sub-layer to $k-\varepsilon$ in the log-layer via a distance-weighted blending function. This hybrid keeps the near-wall fidelity of $k-\omega$ while gaining the free-stream insensitivity of $k-\varepsilon$, improving separation onset prediction under adverse pressure gradients.[48]

Spalart–Allmaras model. A single transport equation is solved for a modified eddy viscosity. The model was tuned for attached external aerodynamic flows and converges rapidly on coarse meshes, but it loses accuracy under massive separation.[48]

These Reynolds-averaged closures provide the speed needed for iterative design while capturing the viscous and turbulent mechanisms that govern pressure loss in the cooling-channel network.[48]

2.4 Cooling drag

For fluid mechanics in general, there is limited number of cases for which there is an available analytical solution (mostly laminar flow solutions). Due to that, empirical formulations have to be used when characterizing internal flow components including pipes, diffusers, inlets, outlets and heat exchangers. Their downside is the limitation of such formulas to the specific geometry and flow parameters that experiment's authors used and in the regime that have been also tested by them.[22]

There are two primary parameters that characterize the flow inside the cooling system and its components: the total pressure loss, which represents the energy loss of the flow, and the mass-flow rate, which directly influences heat transfer within the HE and thus determines the overall heat rejection capability.

The drag arising from the cooling installation comprises three main contributions [37]. The first is the core momentum change due to the net acceleration of the cooling airflow. This drag component is given by

$$D_{\text{core}} = \dot{m}\Big(V_\infty - V_{out}\Big) \tag{2.20}$$

Where V_∞ is the free-stream velocity and V_{out} correspond to the local flow speed at the outlet of the cooling system. Equation (2.20) follows directly from a steady, one-dimensional momentum balance over a control volume enclosing the radiator core. By equating the axial drag force to the net difference in momentum flux through the inlet (V_∞) and outlet (V_{out}) planes, and neglecting static-pressure forces.
The second contribution is the cowl drag from the inlet and outlet fairings. This arises from skin-friction drag and pressure drag over the fairing surfaces, as well as the so called spillage drag. This contribution has been summarized as D_{cowl}. There exists also drag contribution due to components interference but small enough to be neglected, focusing only on D_{core} and D_{cowl} [37].

2.4.1 Core drag

Assuming no outlet flap present, air after going through all the components has to recompress to the ambient static pressure in the nozzle. That means the total head loss is reflected fully in the dynamic head difference between inlet and outlet based on the Bernoulli's equation (2.21). For subsonic systems that are considered in this thesis, this equation holds as the flow is in the Mach number regime where no highly pronounced compressibility effects occur [20].

The original equation assumes no losses and states that the total pressure is constant at any point in the flow, but it can be modified with addition of the pressure loss term.

$$P = P_{static} + \frac{1}{2}\rho V^2 + \rho g h = \text{constant} \tag{2.21}$$

$$P_1 + \frac{1}{2}\rho V_1^2 + \rho g h_1 = P_2 + \frac{1}{2}\rho V_2^2 + \rho g h_2 + \Delta P_{\text{loss}} \tag{2.22}$$

Further simplification can be made by assuming that $h_1 = h_2$

$$P_1 + \frac{1}{2}\rho V_1^2 + \ = P_2 + \frac{1}{2}\rho V_2^2 + \Delta P_{\text{loss}} \tag{2.23}$$

Addressing the first, energy of the flow is lost due to friction (dissipation into heat) and local flow behavior inside certain components (recirculation, diffusion).
To describe energy dissipation due to friction, Darcy-Weisbach equation can be used [19]:

$$\Delta P_f = f \cdot \frac{L}{D_h} \cdot \frac{\rho V^2}{2} \tag{2.24}$$

where L is length of the duct.
Although it can be used for many various parameters, it still contains one empirical parameter f, which is determined experimentally and depends on the Re, roughness

and material of the pipe/duct that is being analyzed.[22]

It gets more compliacted for the divergent/convergent geometry where it is not constant throughout the length of the component, and while friction losses still exist, it is more convenient to quantify the total loss over such component using the general formulation of total pressure loss as:

$$\Delta P = \zeta \frac{1}{2} \rho V^2 \tag{2.25}$$

The dimensionless loss coefficient ζ can be determined experimentally or from empirical correlations, and it accounts for factors such as separation losses, wall friction, and turbulence effects.

Further in the thesis section, ways of predicting the total pressure loss empirically or analytically, over relevant types of the components, will be presented and discussed.

2.5 Ducts

Pipes or ducts are the basic internal flow components, but their geometry and roughness can vary which influences the energy loss.

For the flow inside the pipe, equation 2.1 holds and requires specifying only one empirical coefficient - f. If the flow inside the pipe is laminar ($Re < 2000$) then it can be estimated as:

$$f = \frac{64}{Re} \tag{2.26}$$

For the turbulent flow it can be either taken from the literature [19] or calculated using the widely agreed on Moody chart or Colebrook Equation. [22]

$$\frac{1}{\sqrt{f}} = -2.0 \log_{10} \left(\frac{\varepsilon/D}{3.7} + \frac{2.51}{\mathrm{Re}\sqrt{f}} \right) \tag{2.27}$$

where ε is the pipe roughness height (absolute roughness). The equation is implicit in f, meaning it must be solved iteratively. Duct elements have been implemented in the pre-sizing tool for its completeness but they haven't been used in the example design case.

2.6 Inlet

Mostly two types of inlets are used in the aircraft. First one is the simple scoop inlet employed that has been employed for example in Pipistrel Velis electro (Fig. 2.1 and Fig. 3.21) and the other one is the flush (NACA) inlet seen for example in the Heart X1 prototype (Fig. 2.2) [41].

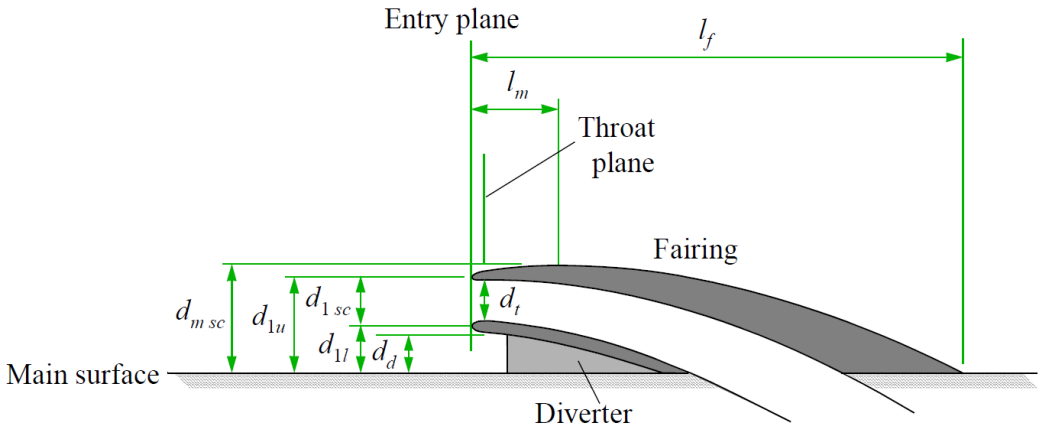

Figure 2.1: Scoop inlet schematic. Adapted from [41]

In general, NACA inlet yields better performance but is more demanding regarding the sizing and sees higher build up of boundary layer due to its flushed nature [41]. Scoop inlet on the other hand, can be located at a d_{l1} distance (Fig. 2.1) exceeding the boundary layer height.

2.6.1 Captured mass flow

For a flight point with true air speed V_∞, static pressure P_∞ and density ρ_∞ the mass flux that would pass the highlight in undisturbed flow is

$$\dot{m}_0 = \rho_\infty V_\infty A_{capture} \tag{2.28}$$

ESDU expresses inlet loading with the ratio

$$\frac{\dot{m}}{\dot{m}_0} \tag{2.29}$$

and shows that boundary-layer development can be collapsed into the single parameter δ/h_{in} [41].

2.6.2 Boundary-layer thickness estimation

As the thesis builds the whole pre-sizing tool from scratch, there is slightly less emphasis on the exact inlet flow behaviour, thus only simplified estimation of boundary-layer blockage influence is assumed throughout.

The boundary-layer thickness δ at the inlet lip is estimated by treating the surface upstream of the lip as a flat plate with zero pressure gradient [20]. Let x be the distance along the surface from the leading edge (or from the point where the boundary layer begins, depending on the inlet location it could be length of the engine nacelle in front of the inlet or length of the fuselage if the inlet is in the fuselage) to the inlet lip. The local Reynolds number based on x is [20]:

$$\mathrm{Re}_x = \frac{\rho_\infty V_\infty x}{\mu_\infty}, \tag{2.30}$$

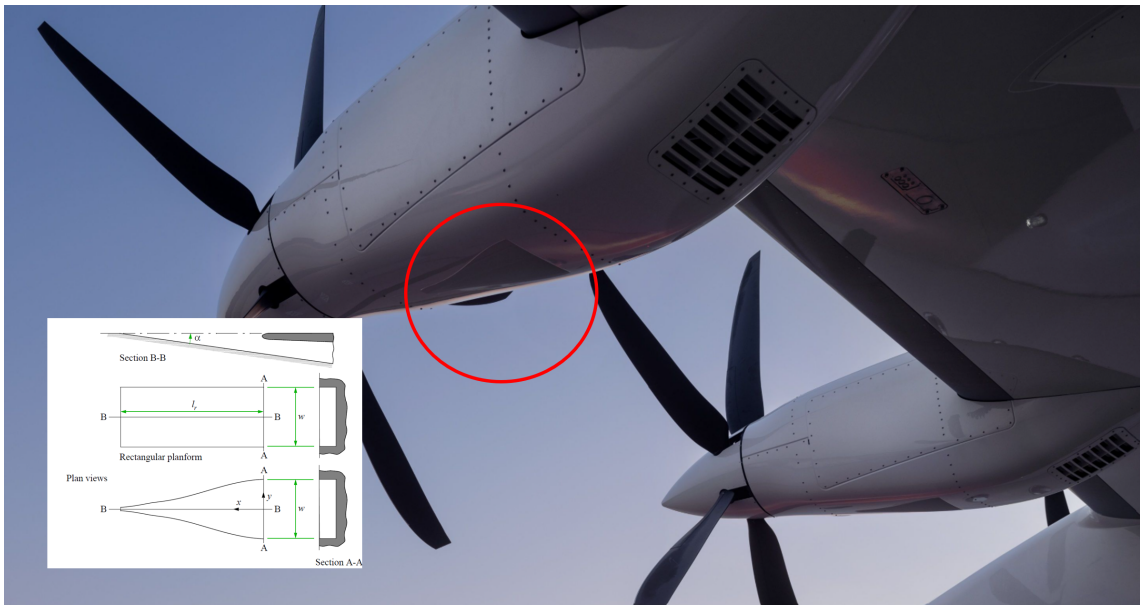

Figure 2.2: NACA inlet in the Heart X1 nacelle with schematic. Adapted from [41] and [9]

where ρ_∞ and V_∞ are the freestream density and true airspeed, and μ_∞ is the dynamic viscosity of the air at that altitude.

If the boundary layer at x remains laminar (typically $\mathrm{Re}_x \lesssim 3 \times 10^5$ on a smooth surface), the 99% developed velocity profile thickness is given by the Blasius solution [20]:

$$\delta_{\mathrm{lam}} = 5 \frac{x}{\sqrt{\mathrm{Re}_x}}. \tag{2.31}$$

If the boundary layer has tripped to turbulence before reaching x (usually $\mathrm{Re}_x \gtrsim 3 \times 10^5$), the 1/7th-power-law approximation applies [20]:

$$\delta_{\mathrm{turb}} = 0.37 \frac{x}{\mathrm{Re}_x^{1/5}}. \tag{2.32}$$

In most subsonic aircraft applications at cruise, the boundary layer is turbulent by the time it reaches the inlet. Once δ is determined, the non-dimensional ratio

$$\frac{\delta}{h} \tag{2.33}$$

is formed, where h is the inlet throat height, as in the Figure 2.3. This ratio is used in in inlet characteristics to determine the total-pressure recovery coefficient ϕ [41].

2.6.3 Total-pressure recovery

Report [41] correlates the ratio of total pressure at the throat to the free-stream value for thin-lip scoops running at the design mass flow. In the range $M \leq 0.8$ the

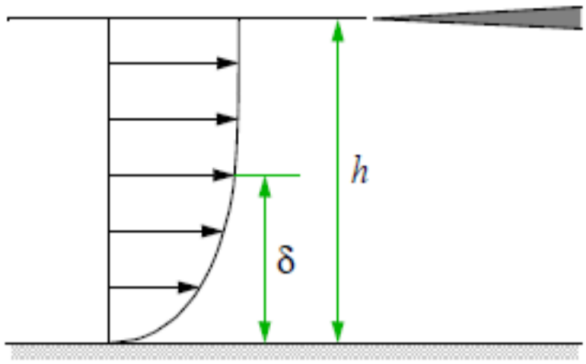

Figure 2.3: Boundary layer in relation to inlet height [41].

data are fitted by

$$\phi = \frac{P_{t,in}}{P_{t,\infty}} = 0.98 - 0.15\,\frac{\delta}{h_{in}}, \quad \zeta_{inlet} = 1 - \phi \tag{2.34}$$

and this expression is adopted by the tool to estimate total pressure drop at the inlet.

If the inlet is placed exactly at the stagnation point, then the the dynamic pressure is 0 and there is theoretically no total pressure loss and the flow inside the system is driven by the static pressure difference between the inlet and the outlet [41].

2.6.4 Propeller effect

More detailed geometry dependent model that accounts for inlet blockage and spillage is a good next step regarding development of the tool. For now it is a good estimation since in a propeller-driven configuration that is analyzed, the propeller slipstream re-energizes the boundary layer and accelerates the inflow to the inlet lip, often thinning or eliminating the natural boundary layer [41]. As a result, one can frequently assume $\dot{m}/\dot{m}_0 = 1$ in the slipstream, since the incoming flow approaches full free-stream momentum. In the end, present version of the tool treats the inlet as if it experiences uniform free-stream conditions and does not include any detailed slipstream re-energization or swirl and pump effects. Those corrections thus should also be incorporated in future development of the pre-sizing tool.

2.7 Diffuser

Flow inside the diffuser is more complicated than the one inside the pipe. Considering that, to quantify the total pressure loss, empirically derived models have to be established for each type of the diffuser and has been done for some geometries for example by Idelchik et al. [19].

Main goal of the diffuser design for the aircraft cooling system, is to provide slowed down, uniform flow distribution at its outlet in order to minimize the pressure drop

at the heat exchanger's core and maximize heat transfer. This requirement comes directly from the core pressure drop formulation, where velocity term contributes in high power [37].
Other performance parameter of the diffuser is the static-pressure recovery coefficient C_{pr}, defined as

$$C_{pr} = \frac{p_{s,\text{out}} - p_{s,\text{in}}}{\frac{1}{2}\rho_{in} V_{in}^2}, \tag{2.35}$$

whose ideal value for uniform, inviscid flow is

$$C_{pr,I} = \left(\frac{A_{\text{out}}}{A_{\text{in}}}\right)^2. \tag{2.36}$$

Engineering Sciences Data Unit (ESDU) report [39] mentions that the actual recovery is reduced below $C_{pr,I}$ by two distinct mechanisms—"insufficiency of diffusion" (non-uniform exit velocity) and "inefficiency of diffusion" (total-pressure loss, $\zeta_{diffuser}$) so that:

$$C_{pr} = C_{pr,I} - \zeta_{diffuser}, \tag{2.37}$$

Moreover, for typical plane-walled diffusers the empirical data become essentially independent of Reynolds number once $\text{Re} \gtrsim 4 \times 10^5$ [39] what was also stated by Gibson et al. [17], and is assumed as an usual case in the ram air cooling systems considered in this thesis.
Short, Wide angle diffusers required for compact and efficient aircraft cooling, by themselves, would always be yielding high energy loss and low static pressure recovery due to highly separated or even jet flow inside them as shown in Figure 2.4 [39]. As an example if we want to fit the cooling system inside the 2 m length nacelle, having 500 mm high heat exchanger, $L/w_1 = 2$ would require 1 m long diffuser duct. Now to land on the edge of the "no appreciable separation" region, the diffuser would have to be (maximally) of an area ratio of about $\frac{A_{out}}{A_{in}} = 1.2$, which assuming the incompressible flow, would yield $\frac{V_{in}}{V_{out}} = 1.2$ which is not enough for high performance cooling system [37].
Regarding above, Several passive and active techniques have been proposed to tame the inherent tendency of short–wide diffusers to separate. The most mature can be grouped into five broad families based on [39, 40]:

1. Geometric tailoring of the wall profile. Separation is most likely to occur in the latter part of the diffuser, once the boundary layer has thickened and the adverse pressure gradient peaks. Bell-shaped duct tries do address that by redistributing the expansion so that the wall angle is highest near the inlet and mildest close to the exit, where the flow is most likely to separate. Inversely, trumpet profiles—the pressure rise is postponed until the core flow has decelerated and can better tolerate it. Gibson showed that this properly optimized trumpet shape, (truncated if applicable) can give even over 50% reduction in the head loss in comparison to straight-walled diffusers, and even more if the last part of expansion (around $17-18°$ is substituted with straight diffuser wall [17]. Mild centre-line curvature (S-shaped or inflected walls diffusers) works on the same principle, trying to apply benefits of

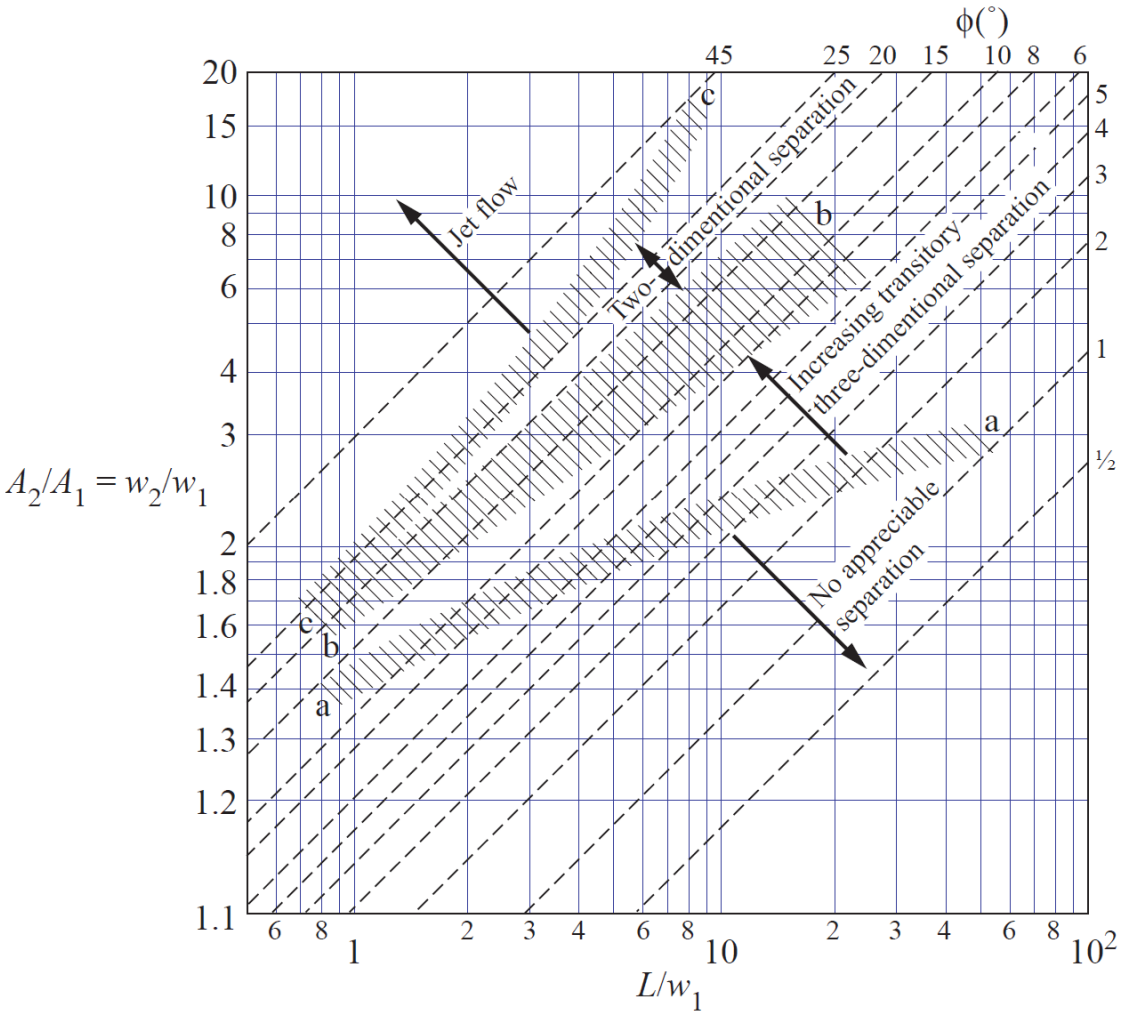

Figure 2.4: Angle and length dependent flow regimes of plane-walled, single-plane expansion diffusers. Adapted from ESDU [39]

both trumpet at the inlet, and bell shape at the outlet.

2. Flow-partitioning devices. Thin dividing vanes or radial splitters break the parent passage into several narrower sub-channels, each operating at a reduced local area ratio (and hence a lower effective wall angle). Two to three vanes in a rectangular diffuser with $2 \lesssim A_{\text{out}}/A_{\text{in}} \lesssim 3$ can halve the total-pressure loss while preserving almost all of the static-pressure rise.

3. Screens and perforated plates. Wire-mesh screens and thin perforated plates can be inserted normal to the flow to inhibit separation by steering the core toward the walls while imposing a controlled static pressure drop after the screen [49, 40, 51]. Authors recommends positioning the first element just upstream of the likely separation plane (or at the plane giving a 20° uniform–angle equivalent) with an initial total pressure-loss coefficient ζ_{screen} dependent on the diffuser and screens position. Additional screens can be spaced evenly to the exit [40, 51]. This flow stabilising

effect is called *filling effect* and is described in more detail in next section, being important part of the numerical investigations of this work.

4. Vortex generators. Small aerofoil vortex generators mounted around the inlet rim promote mixing between the high-momentum core and the boundary layer, delaying separation and improving both static-pressure recovery and flow stability [40]. Available data cover wall half-angles up to 15° and area ratios between 1.9 and 4. Within this envelope the generators are most effective when their height equals roughly the local BL displacement thickness and they are circumferentially distributed at the inlet. Performance gains diminish rapidly beyond these geometric bounds, a trend already highlighted in the broader diffuser review [39].

5. Slot injection and boundary-layer suction. Active control is applied through narrow slots near the diffuser inlet. Injection of a secondary high-speed jet adds momentum to the near-wall flow. Boundary-layer suction removes low-momentum fluid and can raise static-pressure recovery toward one-dimensional ideals over a wider range of wall angles ($5° \leq \phi \leq 45°$) [40]. Both techniques yield markedly flatter exit velocity profiles but require auxiliary air or pumps and careful slot alignment, so they are employed only when passive means cannot meet performance within the available length.

2.7.1 Straight walls diffuser

As an example of the simplest diffuser shape to describe, based on multiple experiments Idelchik et al. [19] derived an empirical formulation (for exapnsion angles $0 < \theta < 40$) for straight walled diffuser's total pressure drop coefficient :

$$\xi_{straight} = 5.30 \left(\tan \frac{\theta}{2} \right)^{1.40} \frac{(v_1 - v_2)^2}{2g} \tag{2.38}$$

2.7.2 Curved walls diffuser

As mentioned in previous paragraphs, efficiency of the diffuser can be increased by making the walls curved, shaped similarly to trumpet [17, 40]. There are different ways to specify such geometry and it's hard to determine the best one in overall as it also changes between the cross-section shapes of the diffuser. Some of them proposed by Gibson et al.[17] are:

$$\frac{dv}{dt} = \text{const} \tag{2.39a}$$

$$\frac{dv}{dx} = \text{const} \tag{2.39b}$$

$$\frac{dP_{\text{total}}}{dx} = \text{const} \tag{2.39c}$$

With a) being uniform retardation, b) uniform diffusion, c) uniform total pressure loss over the length of the diffuser. Geometry developed based on formulation c) has

been chosen as the main, most efficient diffuser component implemented currently inside the design tool, in order not to delve specifically into intricacies of diffuser shape design inside the thesis. Exact formulation is further discussed in the methods chapter.

2.8 Filling effect

A porous element such as a wire-mesh screen or a compact heat-exchanger core can act as a momentum diffuser that spreads the incoming jet and equalises velocity across the section of a wide-angle duct. By flattening the profile it reduces the radial pressure gradients that trigger boundary-layer separation, so the wall flow remains attached even when the cone angle is well above the classical limit for an empty diffuser.[49]

Introducing the screen adds its own total-pressure loss coefficient, denoted ζ_{screen}, yet the attached flow that follows it cuts the loss assigned to the diffuser walls, $\zeta_{diffuser}$. As ζ_{screen} rises from zero the decrease in $\zeta_{diffuser}$ is at first larger, so the combined loss falls. Beyond an intermediate point further increases in screen resistance no longer bring extra stabilisation and the total loss begins to climb again. The design objective is therefore to choose just enough resistance to keep the boundary layer attached while avoiding unnecessary pressure drop in the screen itself.[49]

Placement matters as much as resistance. A first element positioned roughly one inlet diameter downstream of the lip suppresses the primary separation zone, and additional elements spaced progressively downstream maintain filling as the cross-section grows. This staged arrangement lets each element operate at a moderate zeta_screen, keeps the diffuser recovery near its attached-flow ideal, and confines almost all added loss to the porous elements rather than the duct walls [49, 40]. In the cooling-duct layouts studied later in this thesis the heat-exchanger core performs the same role and also benefits from the more uniform flow coming out from the diffuser. Sizing algorithm treats its ζ_{HE} exactly like a porous screen resistance and interpolates the CFD data offsetted $\zeta_{diffuser}$ that includes this phenomena.

2.9 Heat Exchanger

Heat exchangers come in many different forms regarding: transfer process, number of fluids, surface compactness, construction type, flow arrangement, transfer mechanisms and ultimately their function in the process [25], making them hard to describe using one, universal set of equations. Role of a heat exchanger in the cooling system of an aircraft is to transfer the most heat out of the coolant into the air, while creating the least cooling drag [37]. To make the scope smaller while still modern industry relevant, currently implemented types of the heat exchangers are in plate-fin, crossflow configuration, where coolant flows inside the plate doubling as a tube [23], in the direction perpendicular to the cold flow as seen in the Figure 2.5.

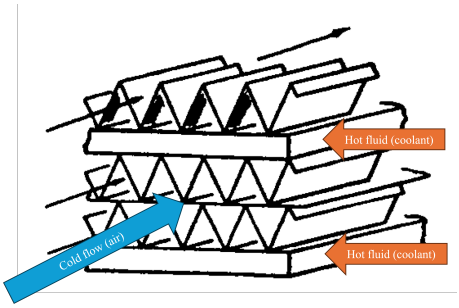

Figure 2.5: Crossflow plate-fin HE example, adapted from [23]

.

Designing and optimizing heat exchanger itself is a complicated task, so the scope regarding HE covered by the pre-sizing tool has been highlighted in the Figure 2.6.

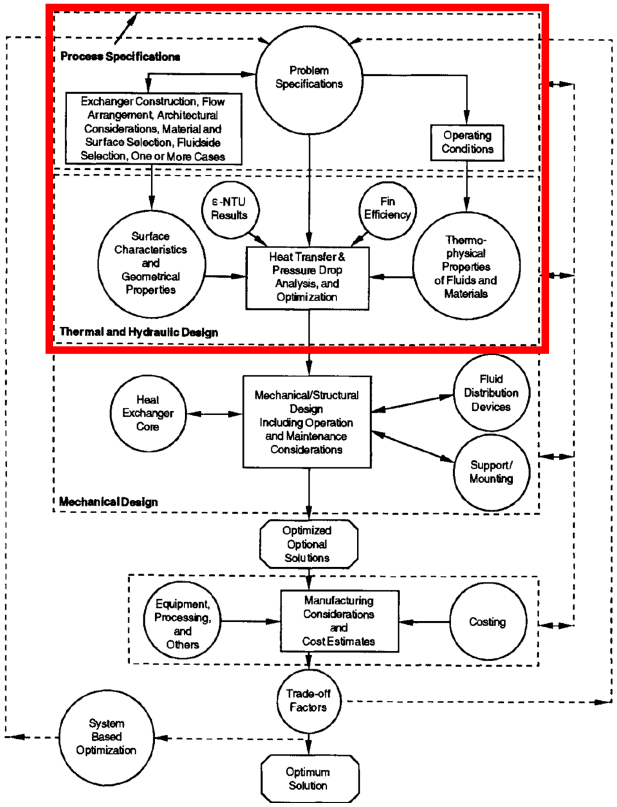

Figure 2.6: HE design methodology, adapted from [23]

.

2.9.1 $\varepsilon - NTU$ method

Popular method to model a heat transfer inside HE is so called $\varepsilon - NTU$ method summarized by Kays and London in the Chapter 2 of [23]. ε stand for efficiency and NTU for number of heat transfer units and can be used to quickly estimate the efficiency of the HE of certain geometry that has been tested before. There

multiple assumptions which allow to arrive at $\varepsilon - NTU$ formulation. Heat transfer that comes out of it can be summarized can be summarized as

$$\dot{Q} \;=\; \varepsilon\, C_{\min}\Big(T_{h,\text{in}} \;-\; T_{c,\text{in}}\Big) \tag{2.40}$$

where $C_{\min}\,(T_{h,\text{in}} \;-\; T_{c,\text{in}})$ term is maximal possible heat transfer $\dot{Q}_{max}$ achievable by the configuration and

$$\varepsilon \;= \phi\Big(\text{NTU},\, C_r, \mathit{flow\,arrangement}\Big) \tag{2.41}$$

is the efficiency of the heat exchanger, and $C_r = \frac{(c_p\dot{m})_{min}}{(c_p\dot{m})_{max}}$ is flow rate capacity ratio of the fluids inside, with $C_{min}\,[\frac{W}{K}]$ pointing the fluid which would undergo the highest temperature change if the heat exchanger was of an infinite size. NTU can be calculated, knowing heat transfer surface A and overall conductance coefficient U as:

$$\text{NTU} \;=\; \frac{U\,A}{C_{\min}} \tag{2.42}$$

NTU just tells how much heat transfer is possible (UA) versus the heat "storage" capabilities of the fluid (C_{min}). Higher NTU in general indicates that there is high heat transfer possibility. NTU, later can be plugged into flow arrangement dependent formulations to get ε, for example:

$$\varepsilon = \begin{cases} \dfrac{1-\exp\Big(-\,\text{NTU}(1+C_r)\Big)}{1+C_r} & \text{(parallel flow)} \\[2ex] \dfrac{1-\exp\Big(-\,\text{NTU}(1-C_r)\Big)}{1-C_r\,\exp\Big(-\,\text{NTU}(1-C_r)\Big)} & \text{(counterflow)} \\[2ex] \dfrac{\text{NTU}}{1+\text{NTU}} & (C_r = 1) \\[2ex] \dfrac{1}{C_r}\Big[\,1-\exp\Big(-\,C_r\,(1-\exp(-\,\text{NTU}))\Big)\Big] & \text{(crossflow, cold unmixed / hot mixed; } C_{\min} = C_c) \\[2ex] 1-\exp\Big(-\frac{1}{C_r}\Big[1-\exp(-\,\text{NTU}\,C_r)\Big]\Big) & \text{(crossflow, cold unmixed / hot mixed; } C_{\min} = C_h) \end{cases} \tag{2.43}$$

to finally be able to calculate the heat transfer from equation 2.40 as a rating problem, for a HE of a given size. It can also be used the other way around, in a sizing problem where for required $\dot{Q}$, heat exchange surface A is calculated.

Whole $\varepsilon - NTU$ method is based on multiple idealisations, mainly regarding change of thermal properties of the fluids. For example U, the overall conductance (reciprocal of resistance) that already lumps together both convection terms (hot and cold fluids through h_h and h_c), fin inefficiency, wall conduction and fouling factors, is taken as the bulk average value for the whole heat exchanger [23]. In reality, it is not constant throughout the core and changes with each step along the tubes and along the thickness of the core.

2.9.2 Pressure drop

Pressure drop at the compact heat exchanger can be described by the below equation:

$$\frac{\Delta P}{P_1} = \frac{G^2}{2g_c P_1}\frac{v_1}{P_1}\left[\underbrace{(K_c + 1 - \sigma^2)}_{\text{entrance effect}} + 2\underbrace{\left(\frac{v_2}{v_1} - 1\right)}_{\text{flow acceleration}} + \underbrace{f\frac{A}{A_c}\frac{v_m}{v_1}}_{\text{core friction}} - \underbrace{(1 - \sigma^2 - K_e)\frac{v_2}{v_1}}_{\text{exit effect}}\right] \tag{2.44}$$

Equation (2.44) describes the pressure drop coefficient across the heat exchanger. The energy lost to friction for a given heat flux depends significantly on the configuration of the fins and tubes within the heat exchanger. In general, fins serve to increase the heat transfer area between the cooling fluid (e.g., air) and the tubes, enhancing convective heat transfer. However, the heat absorbed by the fins must subsequently be conducted efficiently into the coolant flowing within the tubes. Consequently, the conduction resistance of the fins and the physical distance between the fin surface and the coolant can diminish the effectiveness of this configuration. Therefore, the design of compact heat exchangers represents a substantial engineering challenge [23].

Recurring parameter in compact heat exchangers, the porosity σ is defined as

$$\sigma = \frac{A_{open}}{A_{fr}} \tag{2.45}$$

where A_{open} is the total open flow area seen at the face and A_{fr} is the overall frontal area. A value of $\sigma = 1$ means the face is entirely open, $\sigma = 0.5$ means half is open and half is solid, and $\sigma = 0$ corresponds to a completely blocked face. In pressure–drop correlations, the factor $(1 - \sigma^2)$ accounts for the additional loss caused by fluid accelerating through the reduced openings [23].

2.9.3 Integral model

As an approach to enable CFD-derived velocity profile, integral HE model has been implemented, based on the differential energy–balance described in Appendix C of [23], solved numerically by sub-dividing the core into small control volumes and marching the local temperatures and heat rates through the exchanger. An important note is that for now, only cross-flow HE configuration with hot fluid mixed and cold fluid unmixed has been modeled, relying on simplification that coolant's temperature is constant when marching in the core thickness ($x - axis$) direction (coolant is fully mixed in the tubes) [23]. This implementation is described below.

Geometry description

Kays and London measured many fin shapes (plain, wavy, louvered, offset-strip, pin, etc.) and turned the data into two curves that depend only on the flow Reynolds

number Re. First inputs to the model (design vector) are W width, H height and t thickness of the HE. The discrete layout of the fin–tube matrix follows directly from the core envelope and the basic fin/tube dimensions. First, the maximum number of tube rows that can be stacked in the available height H is

$$N_{\text{tube}} = \text{round}\Big(\tfrac{H-b}{a+b}\Big),$$

where a is the external tube height and b the plate spacing. For each row the number of fin sheets that fit across the core length W is

$$N_{fin/\text{tube}} = \left\lfloor \frac{W}{p_f} \right\rfloor,$$

with p_f the fin pitch, so the total fin count becomes

$$N_f = \Big(N_{\text{tube}} + 1\Big)\, N_{fin/\text{tube}}.$$

These numbers fix all remaining geometrical properties as

$$\begin{aligned} H_{\text{core}} &= N_{\text{tube}}\,(a+b) + b, \\ A_{\text{fr,HE}} &= H_{\text{core}}\, W, \\ A_{c,\text{HE}} &= N_f\, A_{c,f}, \\ A_{\text{HE}} &= N_f\, A_f\, \tfrac{t}{l_u}, \\ \sigma_{\text{HE}} &= \tfrac{A_{c,\text{HE}}}{A_{\text{fr,HE}}}. \end{aligned}$$

For the header tanks the projected frontal area, visible from the coolant side, is $A_{\text{fr,H}} = H_{\text{core}}\, t$ and the corresponding flow area is $A_{c,\text{H}} = N_{\text{tube}}\, A_{c,\text{tube}}$, giving the header porosity

$$\sigma_{\text{H}} = \tfrac{A_{c,\text{H}}}{A_{\text{fr,H}}}.$$

Then we define Re, using properties of either one fin channel for the cold side or one tube on the hot side, as

$$\text{Re} = \frac{G\, D_h}{\mu}, \qquad \text{with} \quad G = \frac{\dot{m}}{A_c}\ \text{(mass velocity)} \tag{2.46}$$

Using Re we can look up from the graphs (applying cold-fluid and fins conditions):

A. Heat-transfer (Colburn) factor j

$$j(\text{Re}) = \text{St}\, Pr^{2/3}, \qquad \text{with} \quad \text{St} = \frac{h}{\rho\, V\, c_p}. \tag{2.47}$$

Higher j means more heat can be transferred for the same airflow. This formulation combined with the definition of Stanton number allows for calculation of thermal conductance at the cold side h_c.

B. Friction (Fanning) factor f

$$f(\mathrm{Re}) = \frac{2\,\Delta p}{\rho_c\, V_c^2}\left(\frac{D_{h,f}}{t}\right), \tag{2.48}$$

A lower f means that the hypothetical fan would need less power to force the airflow through the duct. Friction factor is used to calculate the core-friction term of Eq. 2.44.

C. Goodness ratio Φ

$$\Phi(\mathrm{Re}) = \frac{j}{f^{1/3}}, \tag{2.49}$$

The best fin shape at the design Re is the one with the largest Φ.

Practical fin-selection guidelines [23]:

1. Compute the design Reynolds number with Eq. (2.46).
2. Read $j(\mathrm{Re})$ and $f(\mathrm{Re})$ for each fin type from the Kays–London charts [23].
3. Pick the fin that gives the highest Φ in Eq. (2.49). If two fins give almost the same Φ, choose the one with the lower f (smaller pressure drop).

The selected fin-type parameters are then sent to the heat-exchanger model and used for further computations.

Capacity Rates

The hot- and cold-side capacity rates are

$$C_h = \dot{m}_h\, c_{p,h}, \qquad C_c = \dot{m}_c\, c_{p,c}, \qquad C_{\min} = \min(C_h, C_c) \tag{2.50}$$

The smaller of the two is denoted $C_{\min}$ and gives the theoretical maximum heat transfer

$$\dot{Q}_{\max} = C_{\min}\left(T_{h,\mathrm{in}} - T_{c,\mathrm{in}}\right). \tag{2.51}$$

Local Convective Coefficients

For every slice the local Reynolds number is evaluated on each side (Eq. 2.46). To determine the Fanning factor and Nu on the tube (liquid-coolant) side three different formulations, depending on the flow regime, have been used.

Table 2.1: Tube–side correlations for the Fanning factor f_h and Nusselt number Nu_h used in the integral model.

Flow-regime on coolant side	Correlation for f_h and Nu_h
$Re_h < 2{,}000$ (laminar, Nikuradse test)	Fully developed laminar flow in rectangular duct with entrance-length correction [25]
$2{,}000 \leq Re_h \leq 4{,}000$ (transition)	Taborek blending formulation [25]
$Re_h > 4{,}000$ (turbulent, experimental [18])	Gnielinski correlation [18]

On the fin (gas) side a Colburn power law $j(Re)$ and Fanning friction $f(Re)$ from the Kays–London data are applied. The elemental resistances are

$$R_c = \frac{1}{\eta_{0,c} h_c A_{c,\Delta}}, \qquad R_w = \frac{\delta_w}{k_w A_{w,\Delta}}, \qquad R_h = \frac{1}{\eta_{0,h} h_h A_{h,\Delta}},$$

where $A_{c/w/h,\Delta}$ is the surface area of the slice and η_0 the overall-surface efficiency. Cold-fluid properties are refreshed slice-by-slice, while liquid properties are updated along each tube-length increment. Coefficients needed for cold side resitances are:

$$h_c \;=\; \mathrm{St}_c \, G_c \, c_{p,c} \tag{2.52}$$

$$m_c \;=\; \sqrt{\frac{2\,h_c}{k_w\,\delta_f}}, \qquad \eta_{f,c} = \frac{\tanh(m_c\,l_c)}{m_c\,l_c}, \qquad \eta_{0,c} = 1 - \tau_f\Big(1 - \eta_{f,c}\Big) \tag{2.53}$$

where m_c is the classical fin constant as defined in Kays and London [23]. Hot side resistance coefficients are similarly:

$$h_h \;=\; \mathrm{Nu}_h \, \frac{k_h}{D_{h,\mathrm{tube}}} \tag{2.54}$$

$$m_h \;=\; \sqrt{\frac{2\,h_h}{k_w\,\delta_t}}, \qquad \eta_{f,h} = \frac{\tanh(m_h\,l_h)}{m_h\,l_h}, \qquad \eta_{0,h} = 1 - \tau_t\Big(1 - \eta_{f,h}\Big) \tag{2.55}$$

Marching Energy Balance

With $R_\Delta = R_c + R_w + R_h$ the local conductance is $U_\Delta A_\Delta = 1/R_\Delta$. The heat increment and the cold-side temperature rise of the slice are

$$\mathrm{d}\dot{Q}_\Delta = (T_h - T_c)\, U_\Delta A_\Delta, \qquad \mathrm{d}T_{c,\Delta} = \frac{\mathrm{d}\dot{Q}_\Delta}{C_c / N_{\mathrm{fin/tube}}}.$$

The hot-side temperature drop is found analogously with C_h. The solver loops over the N_{row} fin-tube pattern columns and N_x x-direction slices per column, updating fluid properties after each step.

Effectiveness and Duty

At the outlet the integrated duty is $\dot{Q} = \sum \mathrm{d}\dot{Q}_{\Delta}$; the effectiveness is $\varepsilon = \dot{Q}/\dot{Q}_{\max}$. The numerical result has been verified to converge to the closed-form ε–NTU relation when the properties are treated as average. This comparison has been presented later in the HE model validation section of the results chapter.

Pressure Drop

For completeness, the model also estimates the dimensionless pressure-loss coefficients ζ_c (fin passages) and ζ_h (tubes plus headers). Regarding that, only the gas side is considered in the thesis and has been described here with the tube side pressure drop included in code, to use in the future transient analysis of the coolant flow and design on that side.

After integrating the heat transfer, the gas-side pressure loss is evaluated with the individual coefficients that appear in Eq.2.44 introduced earlier:

$$v_1 = \frac{1}{\rho_c}, \qquad v_2 = v_1 \frac{T_{c,\mathrm{out}}}{T_{c,\mathrm{in}}}, \qquad v_m = \tfrac{1}{2}\,(v_1 + v_2). \tag{2.56}$$

Using these specific volumes and the core porosity $\sigma_{\mathrm{HE}} = A_{c,\mathrm{HE}}/A_{\mathrm{fr,HE}}$ the dimensionless terms in Eq.2.44 become

$$\begin{aligned} \zeta_{\mathrm{entr}} &= 1 - \sigma_{\mathrm{HE}}^2 + K_c, \\ \zeta_{\mathrm{acc}} &= 2\left(\frac{v_2}{v_1} - 1\right), \\ \zeta_{\mathrm{core}} &= f_c \frac{A_{\mathrm{HE}}}{A_{c,\mathrm{HE}}} \frac{v_m}{v_1}, \\ \zeta_{\mathrm{exit}} &= -\Big(1 - \sigma_{\mathrm{HE}}^2 - K_e\Big) \frac{v_2}{v_1}. \end{aligned} \tag{2.57}$$

They are summed to give the core-based coefficient

$$\zeta_c \;=\; \zeta_{\mathrm{entr}} + \zeta_{\mathrm{acc}} + \zeta_{\mathrm{core}} + \zeta_{\mathrm{exit}}, \tag{2.58}$$

and finally converted to the frontal-velocity reference:

$$\zeta_{\mathrm{HE}} \;=\; \frac{\zeta_c}{\sigma_{\mathrm{HE}}^2} \tag{2.59}$$

so that the total pressure drop reported by the model is

$$\Delta p = \zeta_{\mathrm{HE}} \frac{\rho_c\, V_{\mathrm{c,in}}^2}{2}. \tag{2.60}$$

2.10 Nozzle

After passing through the HE, flow has to be re-accelerated through the nozzle in order to reach ambient static pressure at the outlet [37]. Because of the favorable

pressure inside the nozzle, flow is unlikely to separate so the nozzle itself accounts for a very small total pressure drop. Its area can be sized as

$$A_{nozzle} = \frac{\dot{m}}{\rho_\infty V_{out}} \tag{2.61}$$

and in relation to heat exchanger area would result in contraction ratio

$$CR = \frac{A_{HE}}{A_{nozzle}} \tag{2.62}$$

It should be chosen so at the design conditions it converts excess static pressure to the ambient conditions. As the tool is using flow marching approach, total pressure might drop below ambient static pressure, which means that it is impossible to realize and the system is effectively stalled, resulting in high drag (C_D due to spillage is maximum for $\frac{\dot{m}}{\dot{m}_0} = 0$ [41]) which is seen by the optimizers. Similar case is when the $P_{t,out} = P_\infty$ which results in $V_{out} = 0$ since the whole dynamic pressure has been spent to push the air through the system. It results in the maximal drag as per equation 2.20 and no cooling due to no mass flow. Regarding that there should be at least small dynamic pressure margin at the outlet to make the cooling system work.

2.11 Outlet

Outlet is a final component of the system and can have a significant on the whole design [42]. If designed aligned with the flow, allows for the lower total pressure loss due to less abrupt mixing with the free-stream [42].

Regular outlet has $c_p = 0$ meaning the flow recompresses to ambient static pressure, but applying louvers, flap, or shaping it in such way, that the free-stream is separated in proximity of the outlet resulting in $c_p < 0$, allowing for more pressure drop inside the cooling system for the cost of increased external drag caused by the outlet modification [43].

Due to limitations of the thesis, outlet is assumed as an ideal with no total pressure drop, with the whole total pressure drop that is happening in the nozzle and at the outlet, lumped in constant ζ_{nozzle}.

2.12 Total drag

For a scoop-type auxiliary inlet the external drag coefficient is decomposed, following [41], as

$$C_D \;=\; C_{D,\text{datum}} + C_{D,\text{skin}} + C_{D,\text{diverter}} + C_{D,\text{profile}} + C_{D,\text{spillage}}\Big(\dot{m}/\dot{m}_0\Big), \tag{2.63}$$

where the individual contributions are summarised in Table 2.2.

Table 2.2: Interpretation of the drag terms in Eq. (2.64)[41].

Coefficient	Physical origin
$C_{D,\text{datum}}$	Baseline pressure drag at the design mass flow
$C_{D,\text{skin}}$	External skin friction on the fairing surface
$C_{D,\text{diverter}}$	Momentum loss on a boundary-layer diverter
$C_{D,\text{profile}}$	Pressure drag due to the fairing profile itself
$C_{D,\text{spillage}}$	Additional drag when captured mass flow differs from the natural stream tube

Following ESDU 86002 the external drag of a sharp-lip scoop inlet is written

$$C_D \;=\; C_{D,\text{datum}} + C_{D,\text{spillage}}(\dot{m}/\dot{m}_0)\,, \tag{2.64}$$

where the constant datum term represents the form drag of the fairing at full mass flow, and the spillage term models the bluff-body penalty that appears as the stream-tube increasingly bypasses the inlet.
Introducing the tabulated spillage factor $k_{\text{sp}}(\dot{m}/\dot{m}_0)$ the second term is expressed

$$C_{D,\text{spillage}} = (1 - k_{\text{sp}}) \left(C'_D - C_{D,\text{datum}}\right) \left(1 - \dot{m}/\dot{m}_0\right),$$

so it vanishes at the design point and reaches the full increment when the inlet is completely starved. Skin-friction drag of the fairing surface and any boundary-layer-diverter drag have been omitted because they are installation-dependent and will be added in future refinements.

In the present pre-sizing tool only the datum and spillage terms are retained and have to be scaled with $\frac{A_{in}}{S_{wing}}$V before summing with the coefficient from the cooling drag. Skin friction and diverter penalties are application-dependent and should be introduced in the future refinement of the inlet model.

The spillage contribution is estimated by

$$C_{D,\text{spillage}} \;=\; \left(1 - k_{\text{sp}}\right) C'_D \left(1 - \dot{m}/\dot{m}_0\right), \tag{2.65}$$

where k_{sp} is the mass-flow factor tabulated in Fig. 7 of [41]. When the inlet captures the full stream tube ($\dot{m} = \dot{m}_0$) the term vanishes; under stalled conditions ($\dot{m} = 0$) it reverts to the maximum penalty C'_D for the chosen Mach number.

2.13 Linearly spaced parameters sweep

One of the tool's function is to perform a simple parameter sweep of the heat exchanger's width, thickness and height. It is implemented using Python's linspace function and defines each parameter vector as

$$w_0 = \Big(w_{0,1},\, w_{0,2},\, \ldots,\, w_{0,N}\Big), \qquad w_{0,i} = w_{0,\min} + \frac{i-1}{N-1}\Big(w_{0,\max} - w_{0,\min}\Big), \qquad i = 1, \ldots, N,$$

$$t_0 = \Big(t_{0,1},\, t_{0,2},\, \ldots,\, t_{0,N}\Big), \qquad t_{0,i} = t_{0,\min} + \frac{i-1}{N-1}\Big(t_{0,\max} - t_{0,\min}\Big), \qquad i = 1, \ldots, N,$$

$$h_0 = \Big(h_{0,1},\, h_{0,2},\, \ldots,\, h_{0,N}\Big), \qquad h_{0,i} = h_{0,\min} + \frac{i-1}{N-1}\Big(h_{0,\max} - h_{0,\min}\Big), \qquad i = 1, \ldots, N.$$

2.14 International Standard Atmosphere

International Standard Atmosphere (ISA) formulation, which governs inlet air properties, is applied for the troposphere (up to approximately 11 km), where the temperature is assumed to decrease linearly with altitude. The temperature at a specified height h is given by:

$$T(h) = T_0 - Lh \tag{2.66}$$

where $T(h)$ is the temperature at altitude h, $T_0 = 288.15$ K is the standard sea-level temperature, and $L = 0.0065$ K/m is the standard temperature lapse rate.
Based on this temperature variation, the corresponding static pressure is calculated using the barometric formula with a linear temperature gradient:

$$P(h) = P_0 \left(1 - \frac{Lh}{T_0}\right)^{\frac{gM}{RL}} \tag{2.67}$$

where $P(h)$ is the static pressure at altitude h [Pa], $P_0 = 101325$ Pa is the sea-level standard atmospheric pressure, $g = 9.80665$ m/s^2 is the gravitational acceleration, $M = 0.0289644$ kg/mol is the molar mass of dry air, and $R = 8.3144598$ J/(mol·K) is the universal gas constant. These expressions assume an ideal gas behavior and hydrostatic equilibrium in the atmosphere. They provide the necessary boundary conditions for the Computational Fluid Dynamics (CFD) studies conducted in the thesis as well as the pre-sizing tool [26].

3
Methodology

3.1 Tool's structure

Cooling system pre-sizing tool has been written in Python. The main structure consists of a components database file where each type of component is implemented as an object with unique initialization requirements and inherent properties that are later used for analysis, like width, height, length, coolant type, geometry of the fins to be used inside the heat exchanger. Most important scripts that build into the tool have been listed in Table 3.1.

Table 3.1: Overview of Python Scripts and Their Functions

Script	Function
`main.py`	Running modes, optimizers, tying together other parts of the tool.
`components.py`	Logic of component models, 1D solver.
`properties.py`	ISA, coolants, materials, and fin geometries, digitized performance curves.
`zeta_extraction.py`	Creates and saves an interpolator from previously extracted CFD `.dat` files.
`velocity_graphs.py`	Functions for creating an interpolator for velocity profiles from CFD `.dat` files.
`interpolator_zeta.py`	Functions for loading the saved `.pkl` interpolator and performing ζ interpolation.
`interpolator_velocity.py`	Functions for loading the saved velocity interpolator and performing velocity interpolation.

Components are then combined into the full cooling system where properties of the flow are calculated at each component outlet based on the input data flowing from the upstream component. Inlet components have input data based on the flight conditions estimated using ISA atmosphere as a function of altitude, ISA temperature deviation, and speed of the aircraft (for now no discrepancy between CAS and TAS).
As seen in Figure 1.4, each component class contains a main `compute` method which takes flow data from the component's inlet and uses the implemented mathematical model to calculate output flow conditions based on the isentropic relations explained in the theory section.

The outlet class has imposed static pressure equal to the ambient static pressure, and outlet flow velocity is calculated based on that condition and the isentropic relations. Outlet mass flow is then matched with the inlet mass flow by adjusting the nozzle contraction ratio. After that, the tool estimates total cooling drag of the system and its weight. If an outlet flap, that creates negative c_p through separation at the outlet is considered in the system, it can be also accounted for through this outlet boundary condition.
This is the logic of the `analyze` method implemented in the main class that combines the components. The design process consists of multiple calls of this method and adjustments to the sizing of the system in order to reach the desired heat transferred by the heat exchanger while minimizing cooling drag or weight, which is further described in the next section.

3.2 Sizing and optimization

Main goal of the pre-sizing tool is to allow for fast and accurate estimation of design to find the best and feasible one considering the chosen goals. To empower this function, three methods have been introduced.

As both $\dot{Q}$ and drag are outputs from the `analyze` method of the full cooling system, it simplifies implementation to only adjusting inherent size parameters of previously initialized HE component and calling the `analyze` method that also adjusts other components' geometry based on the new HE size. This sets up HE as the center of the design that governs the size of other components.

3.2.1 Parameter sweep

First and allowing the highest flexibility for the designer method is the parameters sweep. It is a simple method that relies on specifying the design space (available volume, required $\dot{Q}$ etc.) and sweeping it. The result is a cloud of designs located at $\dot{Q}$ $vs.Drag$ drag plot. Taking minimum $Drag$ value for each $\dot{Q}$ creates a curve of best designs that can be then evaluated further by the designer based on the more specific trade-off factors like volume and weight.

3.2.2 Gradient-based SLSQP Algorithm

Sequential Least Squares Quadratic Programming algorithm is a gradient based method of finding the minimum of given objective function, applied using the

$$\texttt{minimize}(objective(x), x_0, method = SLSQP, bounds, constraints(x))$$

SciPy function, formulated based on its documentation [46]. It is investigated as it has been used in similar previous works like TMS design by OpenConcept et al.[27].

Most important requirement of the cooling system that can't be surpassed is the heat rejected by the heat exchanger. That's why this parameter has been used as a

constraint for the optimizer by using input heat required to be transferred from the coolant to the flow. This relation has been formulated as difference between required heat rate and heat rate of the current design, and normalized with the required heat rate [46].

$$constraint = \frac{(Q_{current} - Q_{required})}{Q_{required}} = 0$$

Objective is the function that is supposed to be minimized so it is the drag force. Both objective and constraint are functions of the design vector x which contains parameters that are manipulated by the optimizer [46]. In problem definition presented in this thesis:

$$x = [HE_{width}, HE_{thickness}, HE_{height}]$$

x_0 is a guess vector which is initial sizing of the HE that has to be declared by the user of the tool. Then bounds for the size of HE have to be established for all 3 dimensions depending on the desired volume, weight or allowed design space. In gradient-based optimizing algorithms of non-linear functions its choice can affect the results of the optimization as the multi-variable non-linear objective function most likely has multiple local minimums that can be pitfalls for the algorithm. It can be solved by using non-gradient optimization algorithms, f.e. genetic.[24]

3.2.3 Gradient-free Genetic Algorithm

One of the gradient-free evolutionary algorithms, the genetic algorithm, has been implemented and tested for its reported ability to explore highly non-convex design spaces without the need for gradient information [24]. The GA is implemented with the open-source `DEAP` package [47], and its structure follows the official library examples, with modifications limited to the problem-specific encoding and fitness evaluation routines.

Encoding and population

Each individual is a vector of three continuous decision variables

$$\mathbf{x} = \begin{bmatrix} w & t & h \end{bmatrix},$$

where w is the plate width, t the plate thickness, and h the fin height. A real-valued, bounded representation is used so that genetic operators can work directly on physically meaningful parameters. The initial population of $N_{\text{pop}} = 60$ individuals is sampled uniformly within the geometric bounds defined by the design space.

Fitness function and constraint handling

For each candidate, the analysis module returns the net drag penalty D and the heat rejected Q. Drag is the primary metric to be minimised, but thermal requirements

impose a hard constraint $\dot{Q} \geq \dot{Q}_{\mathrm{req}}$. Constraint violation is incorporated through a penalty so that the scalar fitness reads

$$f(\mathbf{x}) \;=\; D(\mathbf{x}) \;+\; \lambda \,\max\!\Big\{0,\; Q_{\mathrm{req}} - Q(\mathbf{x})\Big\}, \tag{3.1}$$

where $\lambda = 10^{6}\,\mathrm{N/W}$ ensures diverging designs are always ranked worse than the targeted one.

Genetic operators and parameters

Selection is tournament based (size $k = 3$), favouring fitter individuals while maintaining diversity. New offspring are generated by simulated binary crossover ($p_{\mathrm{c}} = 0.9$) and polynomial mutation ($p_{\mathrm{m}} = 0.2$, distribution index $\eta = 20$), both already provided in the `DEAP` toolbox and left unchanged [47]. Elitism passes the best $N_{\mathrm{elite}} = 2$ solutions unaltered to the next generation to prevent loss of quality.

Termination and convergence behaviour

The run stops after $G_{\max} = 80$ generations or when the relative improvement in the best fitness falls below 10^{-4} for 15 consecutive generations, whichever comes first. Empirically, convergence is usually reached in fewer than 60 generations, i.e. under 7 000 calls to the analysis routine. Throughout the search, candidate solutions scatter over the drag–heat-rejection plane. Post-processing step plots this design cloud and highlights the final optimum with a red marker for visual insight into the GA's exploratory behaviour (see Fig. 3.1).

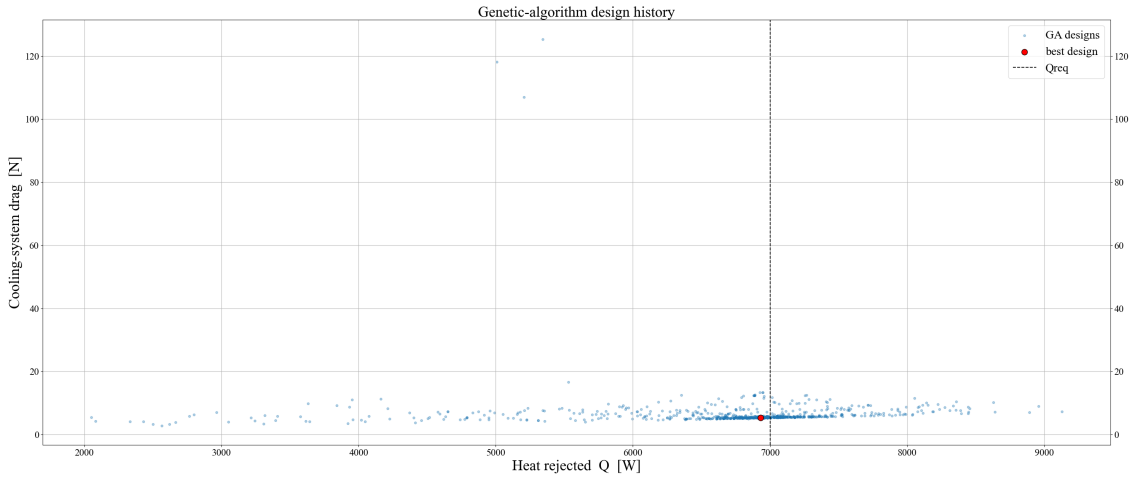

Figure 3.1: History of genetic algorithm - example from the tool

The resulting optimiser is therefore both robust and transparent, requiring only problem-specific changes, while relying on the thoroughly tested operator implementations documented in the underlying library [47].

3.3 Computational Fluid Dynamics studies

Numerous CFD analyses were concluded in the thesis to create the surrogate models that contribute to idea of increasing the fidelity of the pre-sizing routine.
Geometries used inside the computations were created using Python scripts and NX while discretization and pre-processing were done inside the Linux environment using Metacomp's MIME and ICFD++ respectively. Solving itself was done in the CFD++ solver that was setup on the Amazon Web Service (AWS), taking advantage of cloud computing. Although this technological stack wasn't supporting any geometrical sweep by itself, necessary scripts have been written to maximally automatize cloud solving (Bash scripts), pre and post-processing (Python and Tecplot macros).

3.3.1 Curved diffuser

As the basis for all subsequent CFD analyses conducted in this thesis, an initial study of a curved diffuser geometry was carried out, based on the rectangular, trumpet-shaped pipe geometry derived by Gibson et al. [17]. He designs the shape to minimize energy loss in such a pipe with constant head loss per unit length yielding the best results.

He showed mathematically (and verified experimentally) that a curved, trumpet-shaped profile, where the divergence increases along the length, offers reduced pressure loss compared to both straight taper pipes and sudden expansions. The theoretical derivation led to an equation for such a pipe formulated as:

$$y^2 \frac{dy}{dx} = K(x - x_1) \tag{3.2}$$

The constant K has to be calculated for each diffuser geometry based on its inlet and outlet half-breadths y_1 and y_2, its length l, and a shape coefficient of -1.25, as:

$$K = \frac{1}{l}\left\{y_1^{-1.25} - y_2^{-1.25}\right\} \tag{3.3}$$

Using K, the y coordinates for each x can be calculated to get one half of the diffuser, using equation (3.4), with the other half mirrored across the x-axis:

$$y_1^{-1.25} - y^{-1.25} = K(x - x_1) \tag{3.4}$$

One of the geometries that has been tested by Gibson in his experiments has been chosen as an example. It is a single-plane diverging pipe with area ratio of 4, square inlet section of height and width equal to 1.329 *inch* (33.75 mm) and length limited by the equivalent aspect-ratio straight diffuser with total divergence angle $\phi = 30°$ as has been plotted in Figure 3.2.
Gibson has conducted his experiments with inlet mean flow velocities between 0.56 and 6 $\frac{m}{s}$, resulting in a Reynolds numbers, that he claims, make the resultant total pressure drop coefficient *Re* independent as the flow is in fully turbulent regime.

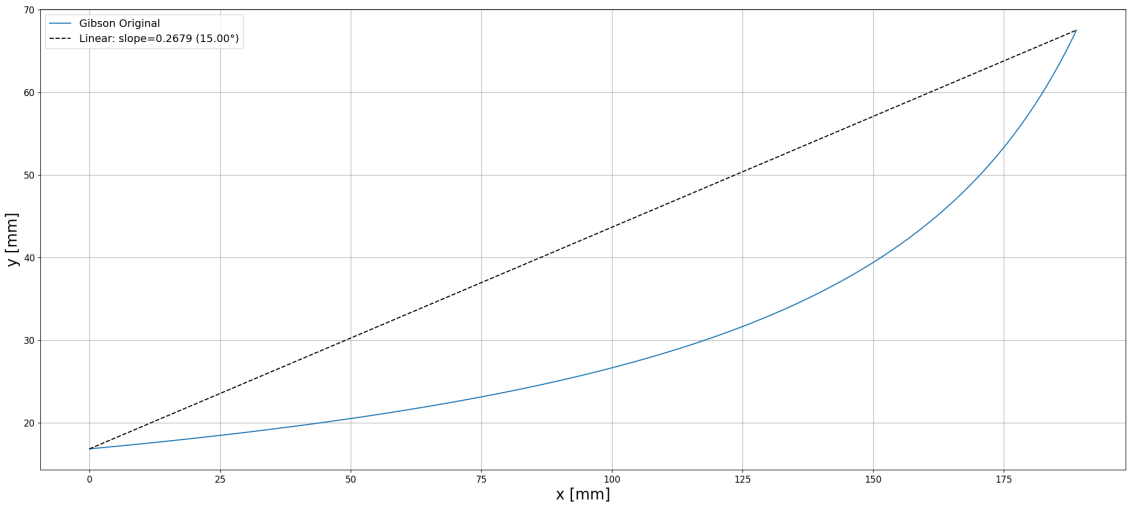

Figure 3.2: Half of the curved diffuser geometry $AR = 4,\ \phi = 30°$

To perform validation, massflow averaged data has been extracted at internal boundaries defined immediately at the diffuser inlet and outlet. Most important for the study were the total pressures $p_{t,\text{in}}$, $p_{t,\text{out}}$, and dynamic pressures q_{in}, q_{out}. The dynamic pressure is related to the local mean velocity by

$$q_{\text{in}} = \tfrac{1}{2}\,\rho\,V_{\text{in}}^2, \quad V_{\text{in}} = \sqrt{\frac{2\,q_{\text{in}}}{\rho}}, \tag{3.5}$$

and likewise for the outlet plane. CFD++ then computes mass-flow-weighted average stagnation pressures on each of the defined planes [44]:

$$\overline{p_{t,\text{in}}} = \frac{\displaystyle\int_{A_{\text{in}}} p_t(z,y)\,\rho\,V_n(z,y)\,dA}{\displaystyle\int_{A_{\text{in}}} \rho\,V_n(z,y)\,dA}, \quad \overline{p_{t,\text{out}}} = \frac{\displaystyle\int_{A_{\text{out}}} p_t(z,y)\,\rho\,V_n(z,y)\,dA}{\displaystyle\int_{A_{\text{out}}} \rho\,V_n(z,y)\,dA}. \tag{3.6}$$

For 2D case that would simplify to 1D integral over dz.
Diffuser loss coefficient ($\zeta_{diffuser}$) has been defined as

$$\zeta_{diffuser} = \frac{\overline{p_{t,\text{in}}} - \overline{p_{t,\text{out}}}}{q_{\text{in}}}. \tag{3.7}$$

We also computed the actual head-loss,

$$\Delta p = \overline{p_{t,\text{in}}} - \overline{p_{t,\text{out}}}, \quad h_\ell = \frac{\Delta p}{\rho\,g}, \tag{3.8}$$

and normalized it by the theoretical sudden-expansion head:

$$\Delta h_{\text{ref}} = \frac{\left(V_{\text{out}} - V_{\text{in}}\right)^2}{2\,g}, \tag{3.9}$$

to obtain Gibson's percentage loss [17]:

$$\text{Loss}(\%) = 100\,\frac{h_\ell}{\Delta h_{\text{ref}}} = 100\,\frac{\Delta p/(\rho g)}{(V_{\text{out}} - V_{\text{in}})^2/(2g)} = 100\,\frac{2\,\Delta p}{\rho\left(V_{\text{out}} - V_{\text{in}}\right)^2}. \tag{3.10}$$

With this definition our implementation will try to reproduce Gibson's reported head-loss of 38 % for the $AR = 4$ curved diffuser, thereby validating and establishing the CFD setup that will be used for further computations inside the thesis.

Computational domain and mesh
All meshes were generated using the MIME module of ICFD++. 2D mesh has been set to be predominantly quadrilateral with a certain global cell size. Firstly, mesh study has been conducted for 4 meshes listed in Table 3.2. As the analysis will use exact solution up to the viscous walls, prism layers with first cell height of 0.004 mm and inflation ratio of 1.15 are kept through all the simulations, assuring $y^+ < 1$.

Table 3.2: Summary of CFD mesh parameters

Case	1	2	3	4
Cell size [mm]	2	4	8	16
Cells [–]	120000	53000	26000	13660

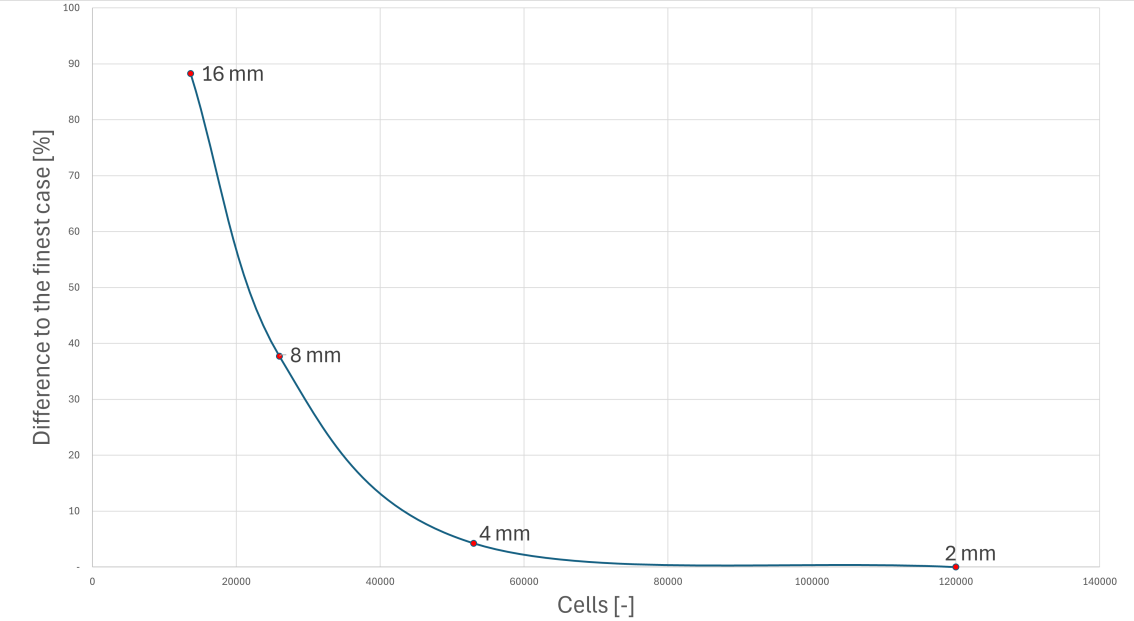

Figure 3.3: Results of mesh convergence study

It is visible that already between 4 and 2 mm cells there is only small change and the curve is asymptotically approaching 0 for the 2 mm (finest case), meaning no meaningful further improvement of the solution's accuracy can be gained through the mesh refinement. Furthermore, after analysing results of the 2D mesh study using $k - \omega\, SST$ model, computations with realizable $k - \varepsilon$ and Spalart-Allmaras (SA) models were conducted for the finest mesh.

In general, the domain was sized based on the hydraulic diameter of the outlet duct visible in Figure 3.4, to ensure full velocity profile and momentum boundary layer

development inside the inlet duct as well as to allow for complete static pressure recovery downstream of the diffuser as suggested in [39].

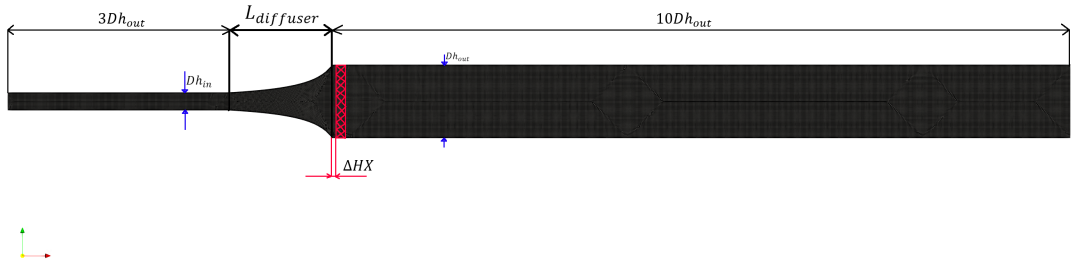

Figure 3.4: Sizing of the domain for the CFD study of the trumpet-shaped diffuser with optional heat exchanger

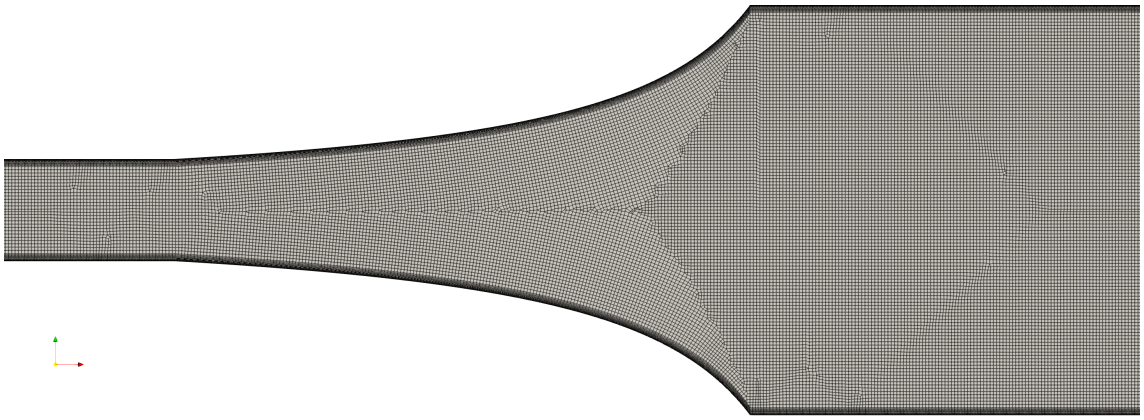

Figure 3.5: Close-up view of the diffuser mesh

3.3.2 Diffuser and heat exchanger coupling

To conduct the analysis of the coupling between the heat exchanger's pressure drop coefficient and the flow inside the diffuser, a CFD study has been conducted using the same curved shape of the diffuser and the same domain sizing criteria as specified in Figure 3.4.

Heat exchanger has been modeled as a porous media physical source term activated in the red-crossed region in Figure 3.4. This source term in ICFD++, is based on the Darcy–Forchheimer law, which models it using inertial loss and friction loss factors as [44]:

$$S_i = \sum_{j=1}^{3} D_{ij}\,\mu\,u_j \;+\; \sum_{j=1}^{3} C_{ij}\,\frac{1}{2}\rho\,|\vec{u}_j|\,u_j \tag{3.11}$$

Second, the inertial part of the momentum loss term accounts for the energy loss caused mainly by turning the flow and forcing it through the porous media. It is

proportional to the velocity squared, which in turn gives much higher influence on the pressure drop than the first, friction term. Because of that, low air viscosity and assumed compactness of the heat exchanger, it is often neglected in similar works and thus has been assumed as $D_{ij} = 0$ in this thesis.
Regarding the inertial loss coefficient C_{ij}, its values were adjusted in conjunction with the heat exchanger, which was set up to have a thickness of 100 mm. This results in $C_{xx} = 10$ in order to obtain a total pressure drop coefficient of 1 across the HX. In directions perpendicular to the flow, C_{yy} and C_{zz} are set to values three orders of magnitude higher ($10^3 \cdot C_{xx}$) to account for the flow-turning behavior characteristic of compact heat exchangers, as has been done for example by Patrao et al. [30].
In reality, both C_{ij} and D_{ij} highly depend on the internal design of a particular HE, especially the geometry of the fins and channels that the air flows through (boundary layer interruptions), which is impossible to predict for new geometries without initial experimental analysis and characterization of that certain fins–tubes configuration. Geometries used in this thesis have been experimentally tested by Kays and London in [23]. According to them, for ram-air cooled systems, the total pressure drop coefficient ζ_{HX} has values between 5 and 50, so for this range of ζ_{HX} the diffuser geometries will be analyzed as an approach to establish surrogate models that give better ζ_{total} predictions inside the pre-sizing tool.
In total, 20 geometries with 4 ζ_{HX} values each were tested, giving 80 data points.

Table 3.3: Parameter ranges for AR, L/h, and ζ used in the study.

	AR	L/h	ζ
Range	4–7	1–2	5–40

Initial conditions
Flow boundary conditions were set to achieve the desired inlet velocity relative to the cruise speed, and an outlet static pressure corresponding to the atmospheric static pressure as defined by the International Standard Atmosphere (ISA) model at a given altitude, described in the theory section.

Table 3.4: Applied boundary conditions.

Boundary	**Boundary condition**
Inlet	Static temperature and velocity
Outlet	Static pressure
Walls	Viscous walls
Heat exchanger	Porous media

The two–equation *k–ω shear–stress–transport* (SST) turbulence model is adopted in the present diffuser study owing to its proven ability to resolve near-wall behaviour while switching to *k–ε* in free stream. This choice was made based on initial CFD studies of the trumpet-shaped diffuser conducted in this thesis with the Spalart–Allmaras (SA) model also giving similar results. It should be mentioned

that the SA model could give a more realistic separation point of the flow inside the diffuser, as investigated by Coletti et al. [29]. This approach could be studied regarding the future tool development. The chosen k–ω SST model, has for example been employed by Cerantola et al. [28] in their experimental review of previous numerical investigations of short annular diffusers.

To initialize the solver, the turbulence kinetic energy k and the specific dissipation rate ω are prescribed from the inlet velocity scale U_{ref}, a prescribed turbulence intensity I, and an integral length scale l. The corresponding expressions are

$$k = \frac{3}{2}\left(U_{\mathrm{ref}}\, I\right)^2, \tag{3.12}$$

$$\omega = \frac{\sqrt{k}}{C_\mu^{1/4}\, l}, \tag{3.13}$$

where $C_\mu = 0.09$ is the standard closure constant [48]. Typical values used in this work are $I = 1$–5% and $l = 0.07\, D_{\mathrm{h}}$. These estimates provide physically consistent initial turbulence levels that facilitate numerical convergence while accurately reflecting the expected inlet conditions.[44]

Results

Most important results to be extracted from the simulation, for application in the tool, are the total pressure drops between the stations at the inlet and outlet ζ_D of the diffuser as well as the actual pressure drop at the HE ζ_{HE}. The sum of these two gives ζ_{total}, which describes the pressure drop of the diffuser/HE coupled system and is the main head loss of the cooling flow that governs system performance. The other substantial result is the friction loss explained in the theory section on the pipe/duct element.
Another result of interest is the velocity profile at the HE inlet. It gives important information on the uniformity of the flow into the heat exchanger. Highly uniform flow is desirable since both total pressure loss and heat transfer depend on velocity, and it is most efficient to use all wetted surfaces of the HE equally.
Because of that unique velocity profile, a difference exists between the pressure drop calculated for the HE (imposed as the inertial resistance of the porous media) and the actual pressure drop that occurs at the HE. This difference is quantified. Based on both results for all 80 data points, surrogate models are later created for use during the pre-sizing.

3.4 Models implementations

3.4.1 Analytical and empirical models

Components have been implemented as explained in the theory section, based on empirical models derived from experiments combined with analytical approach like

shown for the heat exchanger model using integration approach.

Validation of heat exchanger

As a main focus in the tool was to estimate heat exchange and pressure drops accurately (leading to drag), HE models implemented in the tools were validated against experimental test data of commercially available heat exchanger. For the purpose of validation exact working conditions of that test were initialized at the heat exchanger inlet. Available data on test conditions and geometry is presented in Table 3.5.

Table 3.5: Heat Exchanger Geometry and Test Conditions

Parameter	**Value**
Core thickness	32 mm
Fin height	8 mm
Fins per inch	21 fpi
Core dimensions	500 mm × 480 mm × 32 mm
Test fluid	Water–glycol (50/50)
Coolant flow rate range	0.5, 1, 2, 3 L/s
Mean face velocity range	2, 4, 7, 10 m/s
Coolant inlet temperature	90 °C
Air inlet temperature	25 °C

Tubes inside the validation model were chosen as 2.319 mm high with 0.2 mm (Aluminum 3003-O [52]) walls as one of the standard values for similar fin-tube configuration [23].

3.4.2 Surrogate models

Surrogate model is a knowledge-based component model implemented into a system of components to either decrease the computational overhead of each optimization loop or increase the physical accuracy of the design tool [24]. Using the diffuser–HX interference as an example, there is an upstream effect of the HX on the flow inside the diffuser which cannot, to the author's best knowledge, be described by analytical or empirical equations from open literature. Therefore, each output design would require CFD analysis to correct the pressure drop in the diffuser—this change arises from the flow-stabilizing effect that the HX has on it—and to account for the resulting velocity profile and its uniformity at the HX inlet.

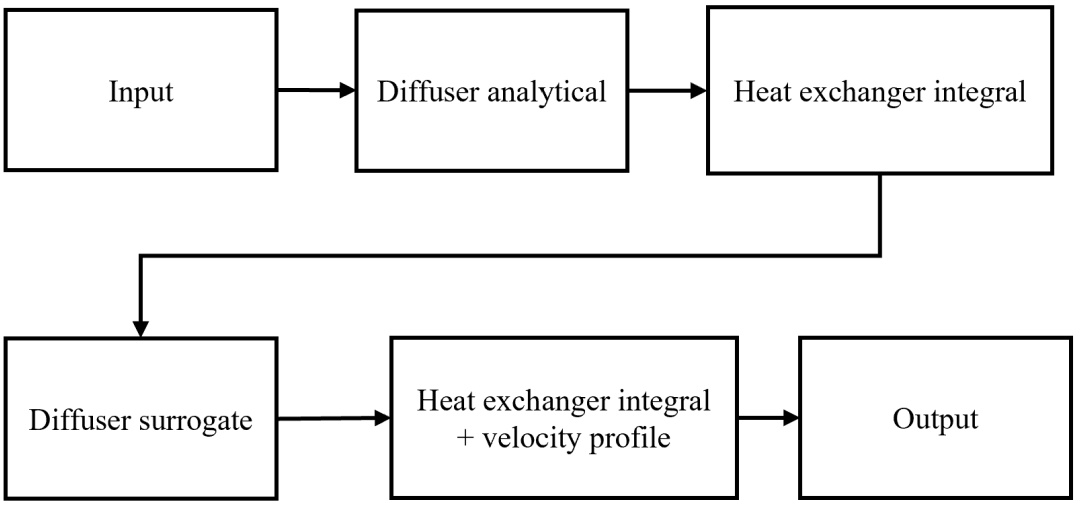

Figure 3.6: Evaluation of surrogate models based on first analytical estimation.

A possible way of increasing fidelity of the tool, without running CFD simulations during optimization, is to establish a surrogate model based on a CFD sweep of curved diffuser geometries and HX pressure drop coefficients. This coupling has been modeled and simulated as part of this thesis and is further discussed in the results section.

Heat exchanger and diffuser — velocity profile
Figures 3.9–3.8 present results for the trumpet diffuser with expansion ratio $AR = 4$ and length ratio $L/h = 1$ for minimum and maximum imposed ζ_{HX}.
To assess the uniformity of the velocity profiles obtained from each diffuser configuration, a nondimensional *non-uniformity coefficient* ψ is computed and displayed at the top of each velocity profile figure. This metric quantifies the proportion of the total kinetic energy associated with velocity deviations from the cross-sectionally averaged value. The coefficient is defined as

$$\bar{V} = \frac{1}{L}\int_0^L V(z)\,\mathrm{d}z \tag{3.14}$$

$$\psi = \frac{\int_0^L \frac{1}{2}\left[V(z) - \bar{V}\right]^2 \mathrm{d}z}{\int_0^L \frac{1}{2}V(z)^2\,\mathrm{d}z} \tag{3.15}$$

In the numerical implementation, the velocity profiles are discretized into $N = 50$ uniformly spaced points along the vertical axis. Assuming $\Delta z = L/(N-1)$, the coefficient is evaluated using the midpoint rule:

$$\psi \approx \frac{\sum_{i=1}^{N} \frac{1}{2}(V_i - \bar{V})^2\,\Delta z}{\sum_{i=1}^{N} \frac{1}{2}V_i^2\,\Delta z} \tag{3.16}$$

where $\bar{V} = \frac{1}{N}\sum_{i=1}^{N} V_i$. The Δz factors cancel, allowing an efficient dimensionless evaluation of profile uniformity.

It is noticeable that increased pressure drop at the HX evens out the flow inside the diffuser and increases its uniformity at the HX inlet. That exact behaviour is impossible to model analytically; thus a surrogate model is established.
First, a simple polynomial fitting approach is used, where each discrete velocity profile is approximated by a fourth-order polynomial:

$$V(z) \approx a_0 + a_1 z + a_2 z^2 + a_3 z^3 + a_4 z^4$$

determined through a least–squares fit to the CFD-computed values. Instead of interpolating all 50 velocity samples for every combination of AR, L/h, and ζ, only the five polynomial coefficients $\{a_k\}_{k=0}^{4}$ are stored and interpolated across the design space. This strategy yields a compact surrogate model that greatly reduces memory requirements and interpolation cost, yet reconstructs the approximated profile. This technique, although simple and lightweight, struggles for more extreme geometries, where the flow is more non-unfirom as visible in the figure 3.11.

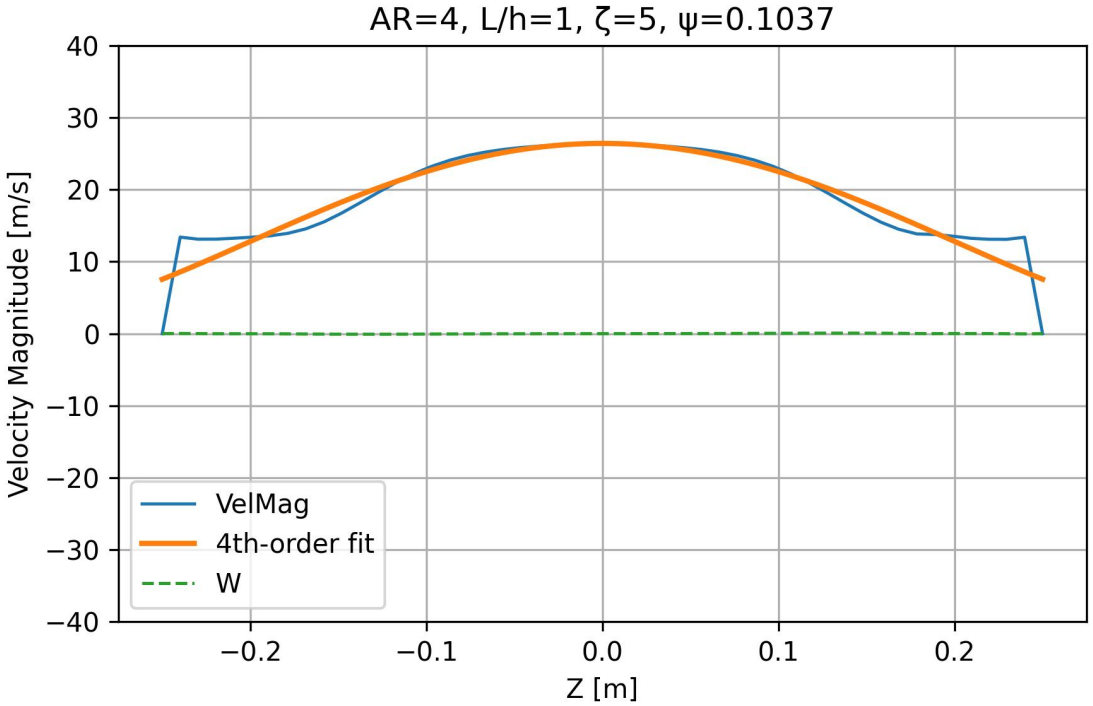

Figure 3.7: Velocity magnitude profile, W component and 4th order interpolation at the HX face. AR=4, L/h=1, $\zeta_{HX} = 5$

To account for that, another, more robust approach of building the interpolator out of 4D data, has been developed for the use inside the pre-sizing tool based on SciPy's `RegularGridInterpolator` function [45]. In principal, all line profiles extracted from the parametric sweep were assembled into a four–dimensional data tensor. For every CFD run a one–dimensional velocity-magnitude profile

$$V\big(Z;\,\mathrm{AR},\,L/h,\,\zeta\big), \qquad Z \in [0, 0.5]\ \mathrm{m},$$

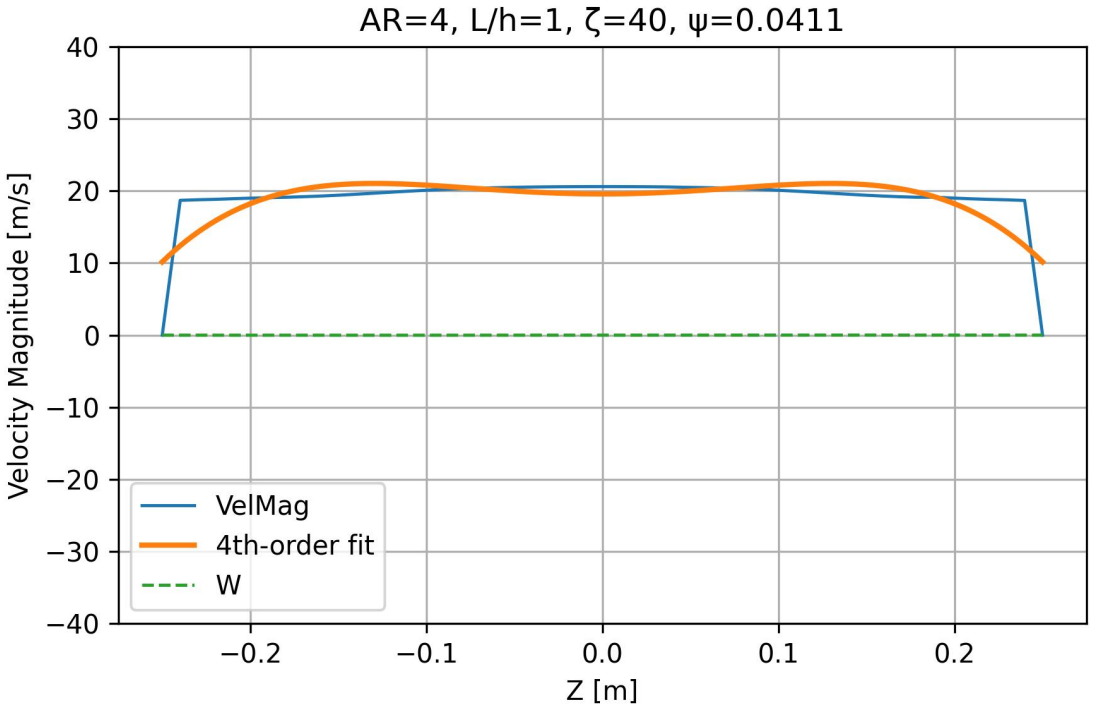

Figure 3.8: Velocity magnitude profile, W component and 4th order interpolation at the HX face. AR=4, L/h=1, $\zeta_{HX} = 40$

is extracted on the diffuser *2D mid-span plane at the inlet face of the heat-exchanger*. The 50 equally-spaced sample points span the full channel height from the lower wall ($Z = 0$) to the upper wall ($Z = 0.5$ m) and therefore represent the flow that actually impinges on the HX core.

Placing every profile on a regular parameter grid produces a four-dimensional data tensor

$$V_{ijkm} \;=\; V\Big(Z_m;\ \mathrm{AR}_i,\ (L/h)_j,\ \zeta_k\Big), \qquad m = 0 \ldots 49,$$

where the three indexing directions correspond to the design variables summarised in Table 3.6. The resulting array has the shape (4, 5, 4, 50), i.e. 4000 scalar values.

Table 3.6: Parameter grids used to assemble the "interpolator cube".

Index	Design variable	Discrete levels in this study
i	AR — diffuser inlet aspect ratio	4, 5, 6, 7
j	L/h — diffuser *length / HX height* ratio	1.00, 1.25, 1.50, 1.75, 2.00
k	ζ — imposed HX total-pressure coefficient	5, 10, 20, 40

For every Z_m slice the 3-D block V_{ijkm} is fed to SciPy's `RegularGridInterpolator`, yielding fifty trilinear interpolants $\mathcal{I}_m(\mathrm{AR}, L/h, \zeta)$. A complete profile at an arbitrary design point is reconstructed by evaluating all 50 interpolants and, if necessary, linearly interpolating along Z to any requested location.

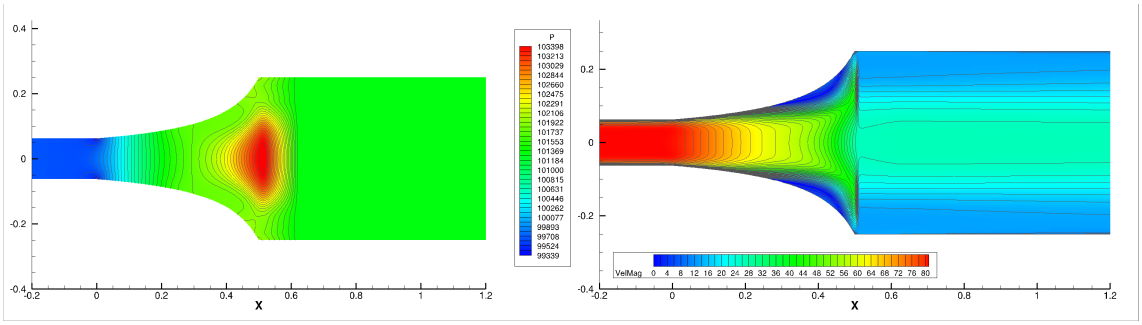

Figure 3.9: Static pressure and velocity magnitude contour plots. AR=4, L/h=1, $\zeta_{HX} = 5$

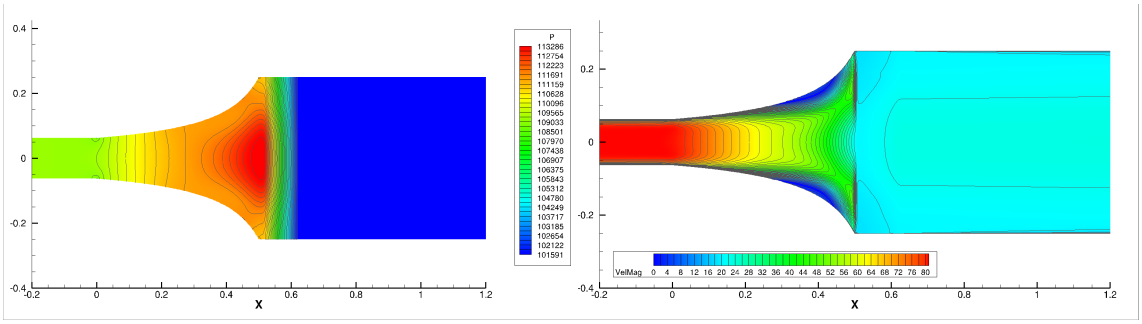

Figure 3.10: Static pressure and velocity magnitude contour plots. AR=4, L/h=1, $\zeta_{HX} = 40$

To avoid undocumented extrapolation the present work *clips all query coordinates to the nearest available grid point*:

$$(\mathrm{AR},\, L/h,\, \zeta) \;\longrightarrow\; \Big[\mathrm{clip}(\mathrm{AR}),\; \mathrm{clip}(L/h),\; \mathrm{clip}(\zeta)\Big].$$

Whenever clipping occurs a console notice is issued, ensuring full traceability. The final pickled data package occupies only 32 kB yet permits instant retrieval of a physically consistent velocity profile for any geometry inside, or just outside the tested envelope.

In the Figures 3.14 and 3.15 example interpolated velocity profiles are plotted as a dashed line in between actual CFD data points, that are plotted as solid lines. It is visible, especially for higher aspect ratio case, that using this type of surrogate model is more accurate and could be further refined by accumulating data points for more geometries and imposed inertial resistance coefficients.

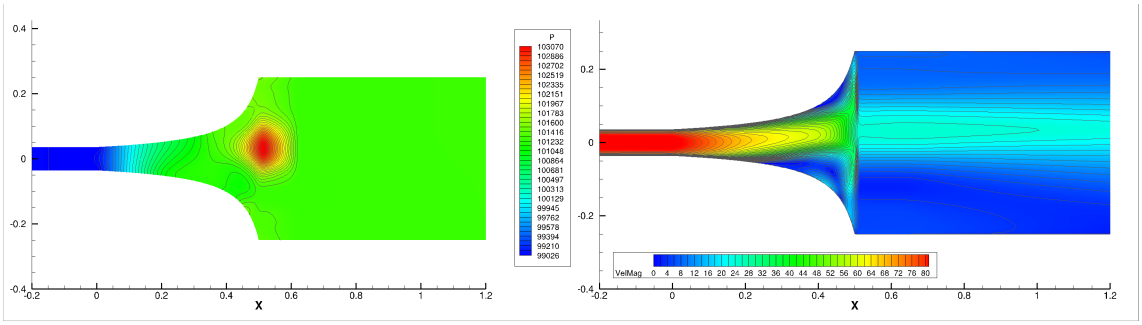

Figure 3.11: Static pressure and velocity magnitude contour plots. AR=7, L/h=1, $\zeta_{HX} = 5$.

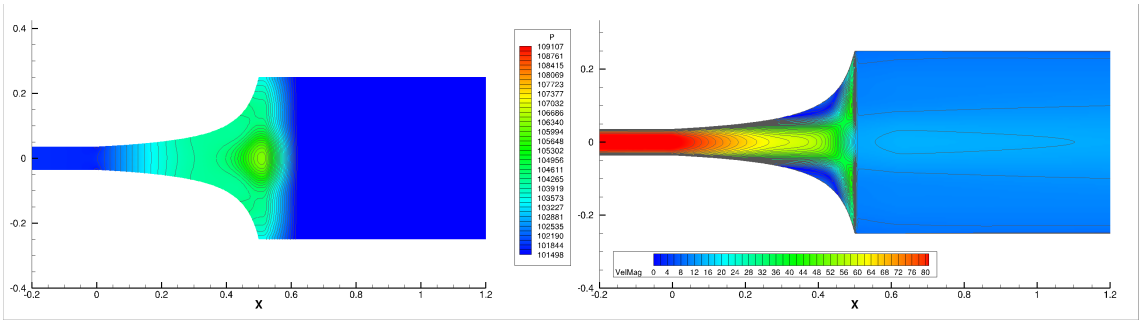

Figure 3.12: Static pressure and velocity magnitude contour plots. AR=7, L/h=1, $\zeta_{HX} = 40$.

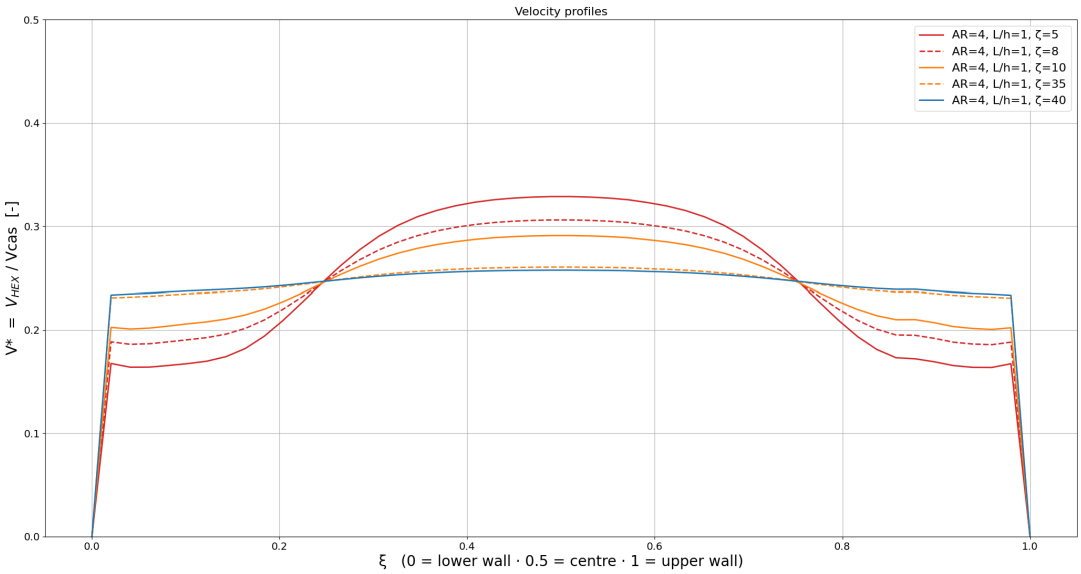

Figure 3.14: Velocity profiles interpolation examples at the HX face. AR=4, L/h=1.

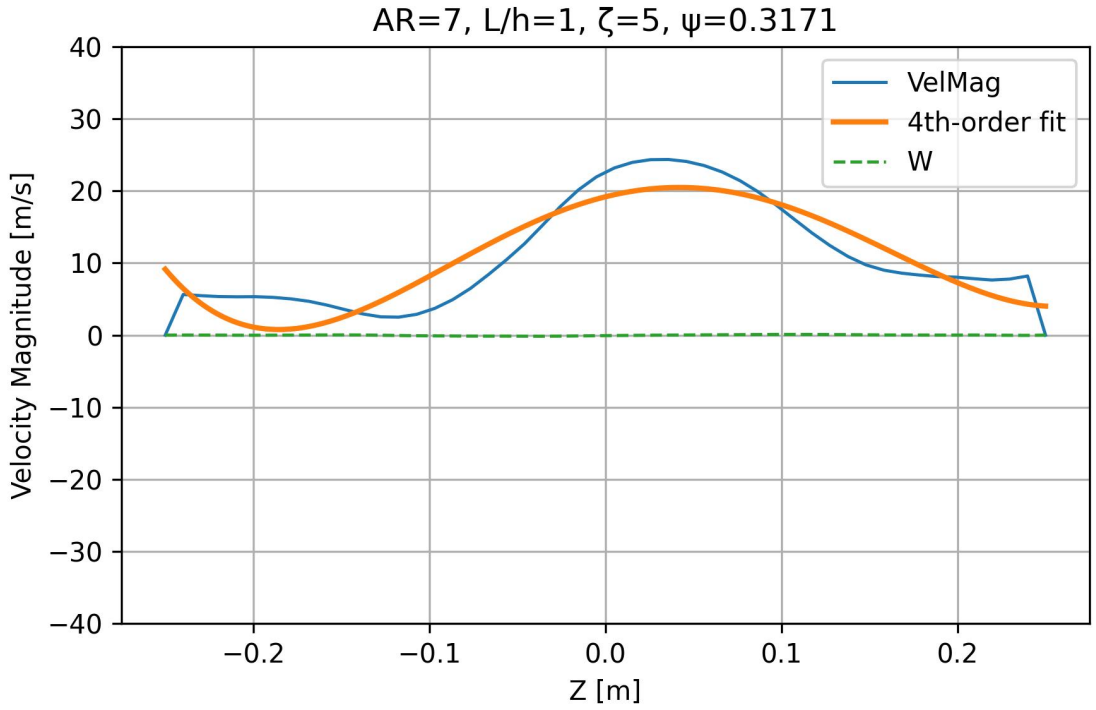

Figure 3.13: Velocity magnitude profile, W component and 4th order interpolation at the HX face. AR=7, L/h=1, $\zeta_{HX} = 5$.

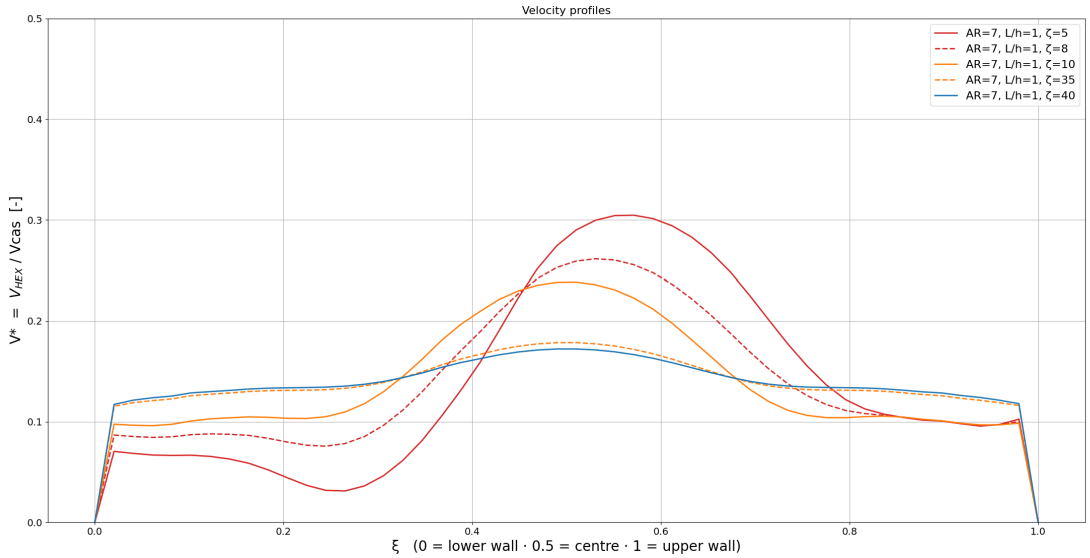

Figure 3.15: Velocity profiles interpolation examples at the HX face. AR=7, L/h=1.

This velocity profile is used inside the implemented integral HX model to determine velocity at each *cell* center of the discretized heat exchanger as,

$$V(x, y, \frac{z}{z_{max}}) = \frac{V_{HEX}(\frac{z}{z_{max}})}{V_{CAS}} V_{CAS} \tag{3.17}$$

assuming the interpolated profile is spread along *z-axis*, perpendicular to the flow.

Pressure drop coefficient
As described in section 2.8, *filling effect* has an influence on the flow inside the diffuser resulting in changed loss of energy in the flow based on the downstream porous element [49].

Using the same methodology of building the interpolator as for the velocity profile, pressure drop coefficient interpolator is created and implemented inside the tool. Example of interpolation between CFD data points for imposed porous media resistance coefficient derived from $\zeta = 20$ is presented in the Figure 3.16. It correctly interpolates the values in-between for diffuser with Area Ratio of 4.5 and is implemented in the pre-sizing code. It is furthered checked with $\zeta = 0$ simulations in the results chapter.

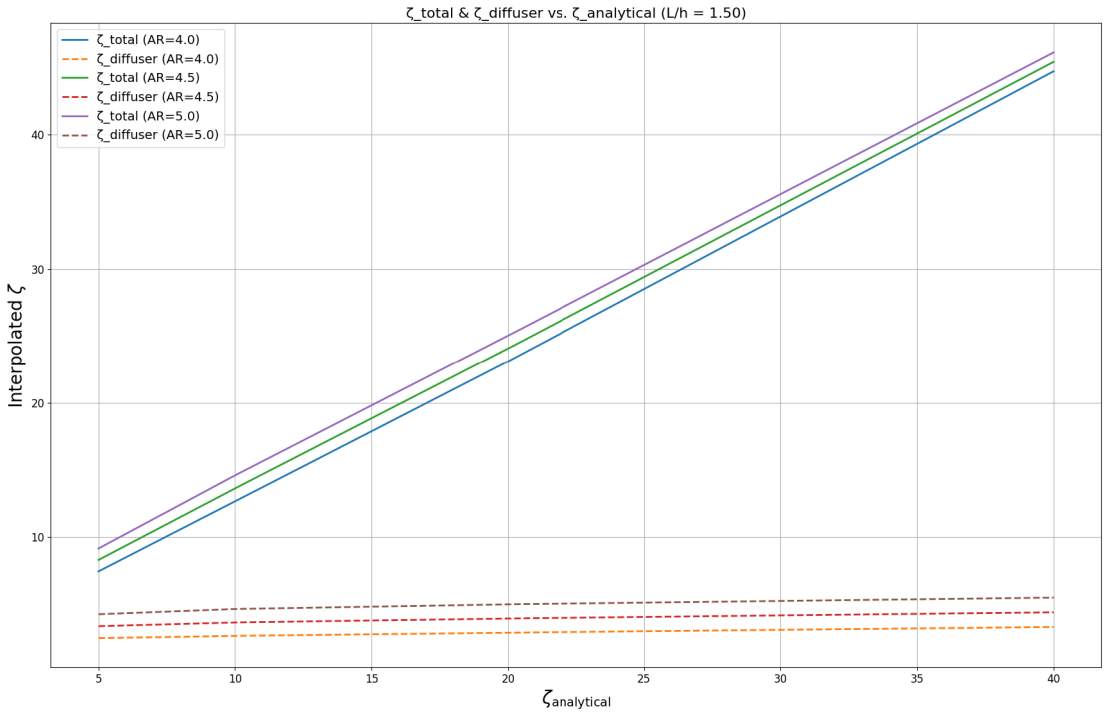

Figure 3.16: Pressure drop coefficients example interpolation for 3 area ratios

As visible in the Figures 3.17-3.18, ζ_{total} decreases with L/h (effective length of the diffuser) and increases with its area ratio as expected. Slopes of the ζ_{total}, and $\zeta_{diffuser,q2}$ (related to thedynamic pressure of the heat exchanger inlet), also indicate that the contribution of the diffuser to ζ_{total}, is noticeably smaller even at higher AR.

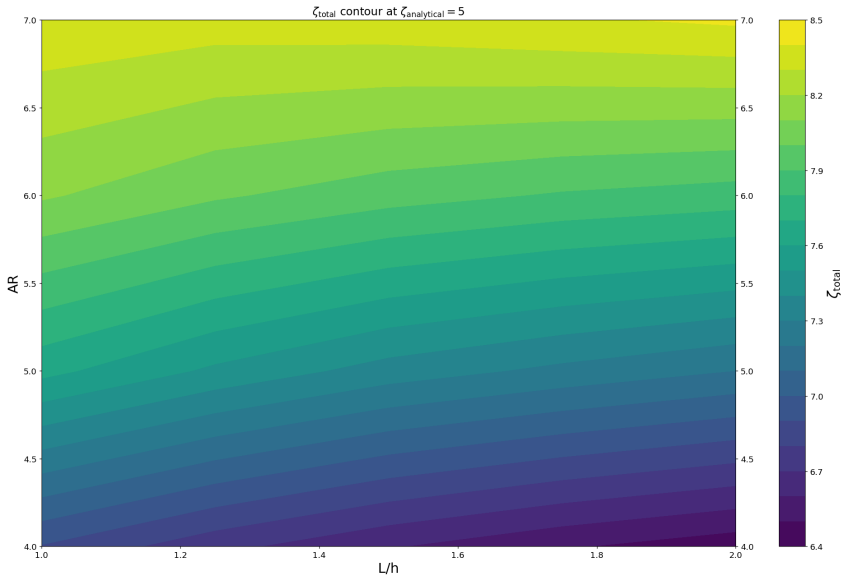

Figure 3.17: Total pressure drop coefficient contour plot for imposed $\zeta_{HE} = 5$

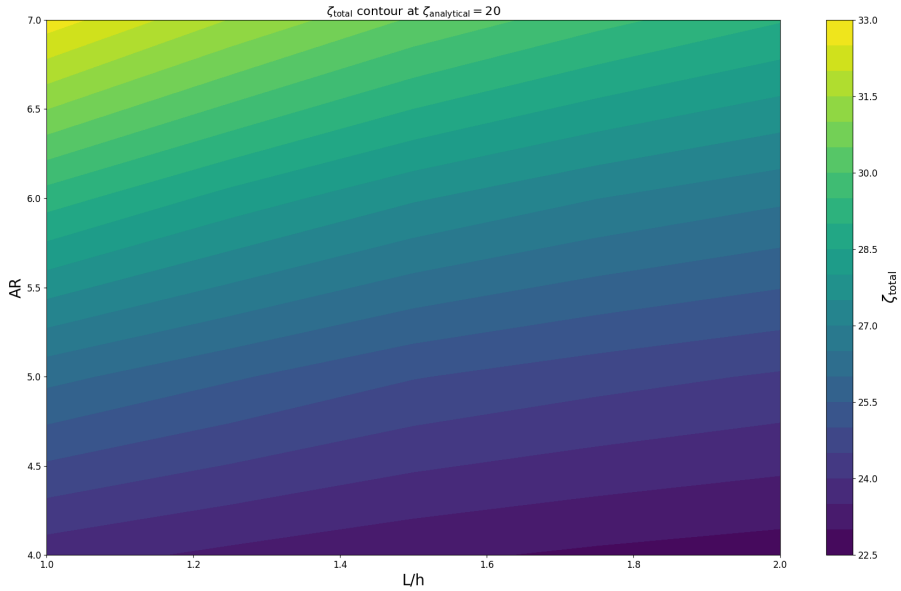

Figure 3.18: Total pressure drop coefficient contour plot for imposed $\zeta_{HE} = 20$

3.5 Weight estimation

Weight estimation has been based on the geometrical characteristics of fins and tubes with same single material chosen for both of them. Tubes, fins and header plates have been approximated with simple geometrical shapes like hollow cylinders, cuboids and thin sheets of certain shape.

3.6 Heat transfer requirements

The first step in designing the cooling loop is to determine the total heat rate $\dot{Q}_{\text{req}}$ that must be removed from the coolant by the heat exchanger. In this thesis, we use a steady-state approach, so $\dot{Q}_{\text{req}}$ is simply the sum of the waste heat produced by each cooled component:

$$\dot{Q}_{\text{req}} = \sum_i \dot{Q}_i = \dot{Q}_{\text{motor}} + \dot{Q}_{\text{battery}} + \dot{Q}_{\text{inverter}} + \cdots + \dot{Q}_{\text{other}}. \tag{3.18}$$

For each component i, the heat it generates is the difference between its input power P_i and the useful power output. Equivalently,

$$\dot{Q}_i \;=\; P_i\Big(1-\eta_i\Big), \quad \text{for example,} \quad \dot{Q}_{\text{motor}} = P_{\text{motor}}\Big(1-\eta_{\text{motor}}\Big). \tag{3.19}$$

This steady-state model does not track the gradual warming of the coolant as it passes from one component to the next. In practice, that temperature rise affects both the heat transfer rate and the maximum allowed temperature for each device. In general when designing a system, the coolant temperature leaving the main heat exchanger, $T_{\text{HE,out}}$, should be low enough to meet the most restrictive temperature limit of any component in the loop with some margin and on a hot day ISA conditions, like have been done for example during the study of the regional jet X-57 by NASA [38]. The impact of this assumption is discussed in the design case section of this chapter.

3.7 Design case

To evaluate the tool's performance and provide an example application, the proposed design case is based on the Pipistrel Velis Electro aircraft. It has been chosen as it's certified and flying example of an electric aircraft. It is using certified E-811 Engine with a lot of data needed for cooling design available in the type-certificate data sheet (TCDS) issued by EASA for Pipistrel Vertical Solutions d.o.o. for model 268MVLC of the engine [31].

3.7.1 Defining operating conditions

The most important parameters to consider from TCDS, are power ratings, temperature limits and coolant flow rate and type.

Table 3.7: Technical Characteristics of the E-811 Electric Engine [31]

Parameter	**Value**
Dimensions	
Motor Diameter	268 mm
Motor Width	91 mm
Power Controller Dimensions	245 × 126 × 230 mm
Installation	Motor and power controller can be installed independently
Dry Weight	
Motor Weight	22.7 kg
Power Controller Weight	7 kg
Power Ratings	
Maximum Take-off Power (MTOP)	57.6 kW at 2500 rpm under 400 Vdc (limited to 90 seconds)
Maximum Continuous Power (MCP)	49.2 kW at 2350 rpm under 400 Vdc
Coolant Specification	
Coolant Requirement	50% water + 50% glycol (G12+ automotive grade)

Crucial factor that is missing in the type certificate, is the efficiency of the E-811 engine, as based on it required heat transfer rate is calculated. It can be assumed based on the information that the engine combines 268 MV LC VHML motor with H300C power controller (inverter). The designation "268 MV LC VHML" as used in the Pipistrel E-811 type certificate corresponds directly to the EMRAX 268 axial-flux permanent-magnet motor family. In the EASA TCDS, the E-811 engine is specified as combining "a 268 MV LC VHML motor and a dedicated H300C power-electronics controller," and is described as an "axial flux synchronous permanent magnet electric motor" [31]. On the manufacturer's side, EMRAX's product documentation lists the EMRAX 268 motor as available in High-Voltage (HV), Medium-Voltage (MV) and Low-Voltage (LV) variants, each offered in air-cooled (AC), combined-cooled (CC) or liquid-cooled (LC) configurations. Thus, "MV LC" decodes most likely to "Medium-Voltage, Liquid-Cooled," and the suffix "VHML" follows EMRAX's internal naming convention for that exact MVLC rotor assembly [32]. By matching the nomenclature in the EASA TCDS with EMRAX's published motor variants, one confirms that the 268 MV LC VHML is indeed the certified EMRAX 268 motor used in the Velis Electro. EMRAX 268 data specification states in the Figure (3.19 an efficiency of $90 - 96\%$ [32]. That corresponds to the following heat transfer requirements:

Table 3.8: Operating Limitations of the E-811 Electric Engine [31]

Parameter	**Limitations**
Ambient Operating Temperature	-20°C to +40°C
Motor Temperature Limit	110°C (at MCP and MTOP)
Controller Temperature Limit	70°C (at MCP and MTOP)
Motor Speed Limit (MCP)	2350 rpm
Motor Speed Limit (MTOP)	2500 rpm
Torque Limit (MCP)	200 Nm
Torque Limit (MTOP)	220 Nm
Pressure Limits	Not applicable
Max Controller Current	311 A (220 Arms)
Max Continuous Current	226 A (160 Arms)
Voltage Range (Input)	250 Vdc (min) to 400 Vdc (max)
Coolant Temperature Limit	60°C (at controller inlet)
Minimum Coolant Flow	5.5 l/min
Time Limited Dispatch	Not approved; all systems must be functional before flight
ETOPS Capability	Not applicable

Table 3.9: Heat Rejection of the E-811 Engine for Efficiency Range 90–96%

Condition	**Power (kW)**	$\dot{Q}_{motor}$ **@90% (kW)**	$\dot{Q}_{motor}$ **@96% (kW)**
Continuous	49.2	$49.2 \times (1 - 0.90) = 4.92$	$49.2 \times (1 - 0.96) = 1.97$
Take-off (90 s)	57.6	$57.6 \times (1 - 0.90) = 5.76$	$57.6 \times (1 - 0.96) = 2.3$

Although the take-off value at 90% efficiency will be used for sizing the system in this design scenario, it is crucial to consider other significant factors that influence the selection of cooling system components.
Those factors include the actual flight conditions, as they determine the mass flow through the cooling system, total pressure at the inlet and temperature of the air. The velocity of the aircraft during take-off is lower compared to climb; however, cruise conditions require less power. Therefore, both the required and available heat rejection vary throughout the aircraft's mission. Most previous studies on similar topics, such as [27] or [30], sized components using the Top of Climb (ToC) as the design point. It is also important to check both ambient operating temperature ranges and check the design for both dT_{ISA} that give -20°C and $+40$°C.

Table 3.10: ΔT_{ISA} deviations for limiting ambient temperatures

Actual Temperature T_{amb} [°C]	$\Delta T_{\mathrm{ISA}} = T_{\mathrm{amb}} - 15\,^{\circ}\mathrm{C}$ [°C]
-20	$-20 - 15 = -35$
$+40$	$+40 - 15 = +25$

Another important parameters are the maximal temperature of the coolant at the inlet to the H300C controller and minimum coolant's flow rate. First one is the out-

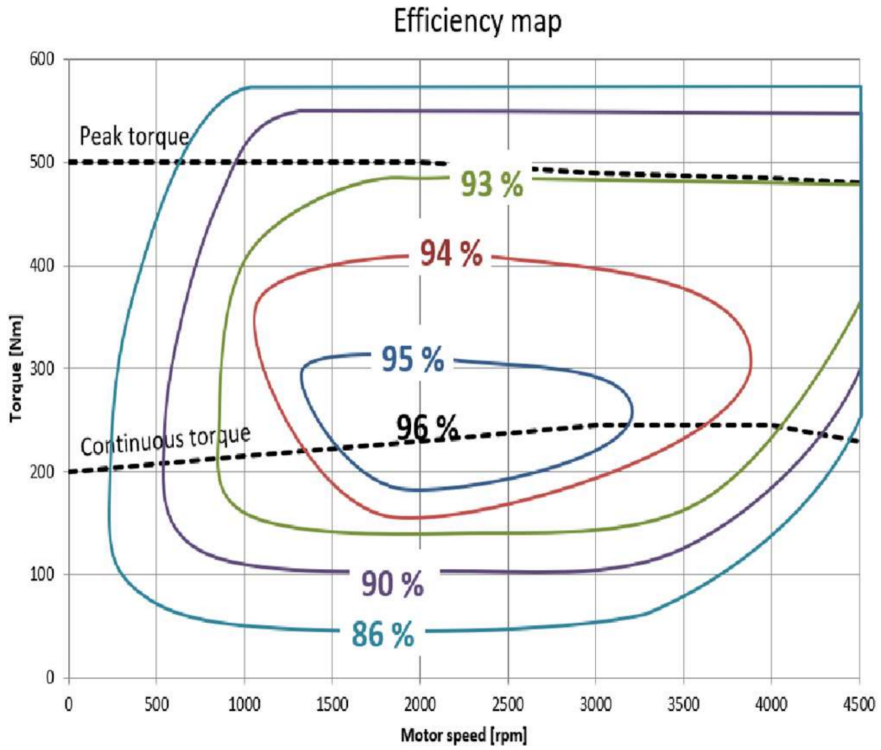

Figure 3.19: EMRAX 268 efficiency map [32]

put from the design tool while the flow rate has to be imposed before the analysis and depends on the exact pump model used in the Velis Electro aircraft.
In conclusion, the system should maintain the coolant outflow from the heat exchanger at ambient temperature below 60°C when the aircraft is operating at Top-of-Climb (ToC) conditions with a 40°C ambient temperature.

Wing area $S_{wing} = 9.51\ m^2$ will be used for drag coefficient calculations.

$$c_d = \frac{Drag}{q_\infty * S_{wing}} \tag{3.20}$$

Engine cooling system

First of the implemented cooling loops is the engine cooling system, visible in the Figure 3.20.

Although no official information on the sizing of the system, except the operating parameters presented in previous paragraph, is available, thanks to the courtesy of the pilot Oskar Dahl it was possible to access the Pipistrel Velis Electro hangared at the Säve airport and take rough measurements of the external components (inlets) and make estimations of the heat exchanger used. Most relevant take outs, regarding the sizing are pictured in the Figures 3.21 and 3.22.

Based on the measured geometrical data, and heat exchanger height estimation it was possible to recreate similar *inlet–diffuser–HE* configuration in NX to get an

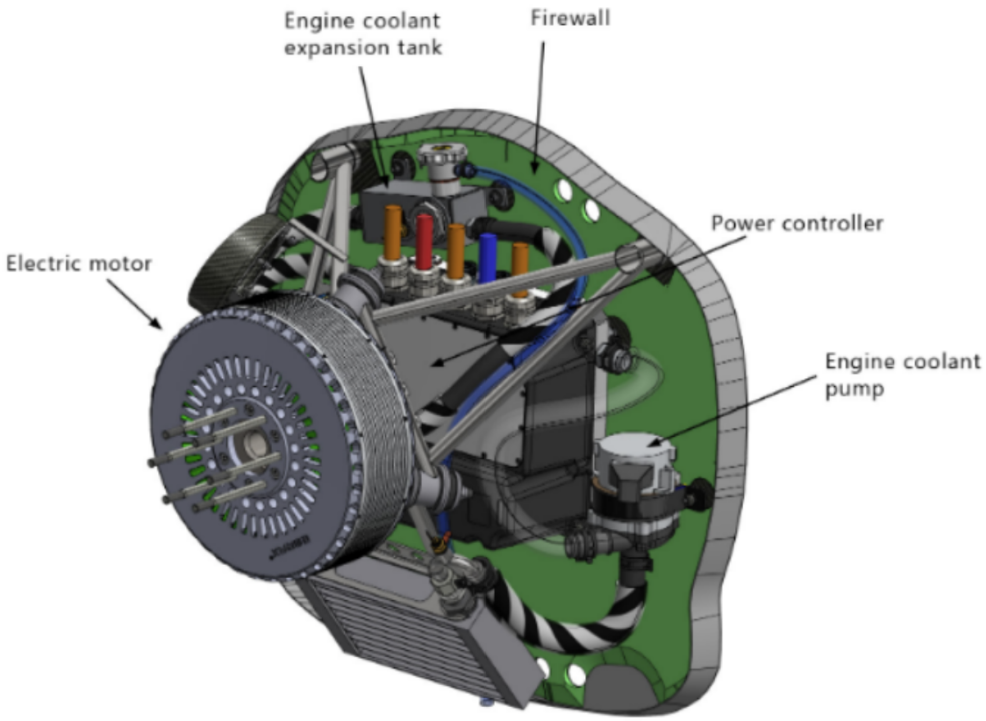

Figure 3.20: Velis Electro Engine Cooling System components highlighted [34].

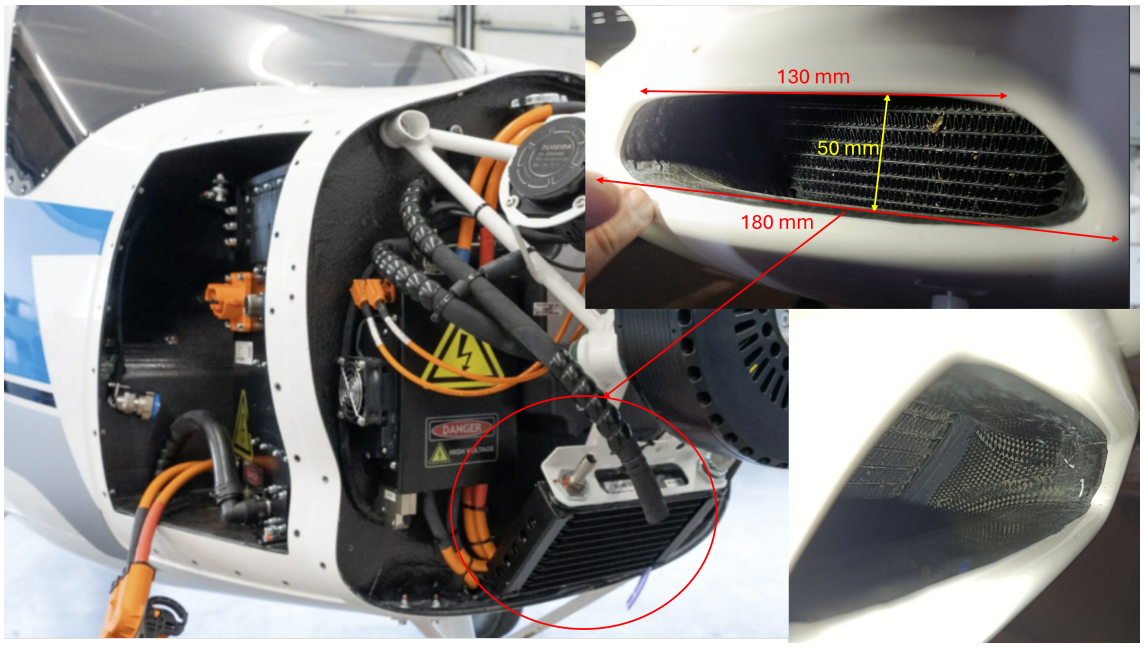

Figure 3.21: Composite image of the Velis Electro open engine compartment [36], with inlet photos, courtesy of Oskar Dahl (Säve Airport May 2025).

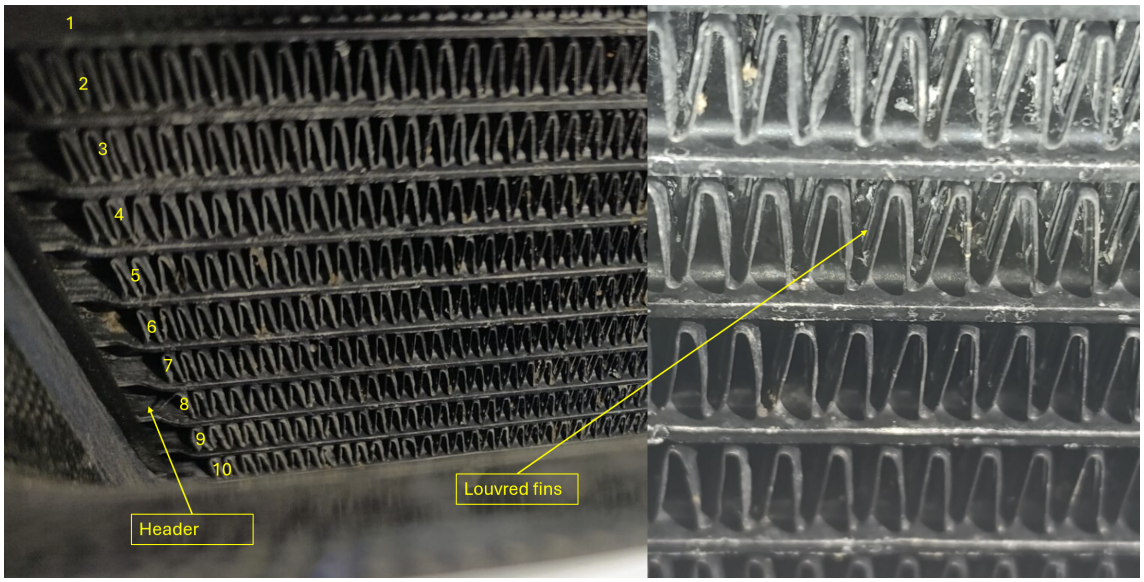

Figure 3.22: Velis Electro Engine Cooling System radiator, courtesy of Oskar Dahl (Säve Airport, May 2025).

approximate AR of the diffuser (3.23). Although this approximation is rough, it allows for further assumption, that the heat exchanger's frontal area is in fact 180 x 180 mm square, with 40 mm thickness based on the proportions on the photos.

$$AR = \frac{27000}{8000} \approx 3.38$$

For the reverse analysis, fin geometry has been chosen as one similar (from Kays and London [23]) to the louvered fins visible in the HE photo (Figure 3.22). With 10 fin-tube patterns and 180 mm total height, that would result approximately in 18 mm per pattern, giving about 15.3 mm fin height (proportions at the photos). Unfortunately this size couldn't be exactly matched with any geometry tested by Kays et al. [23] so the number of fins and tubes won't be aligned with the original design. As visible in the Figure 3.21, HE is tilted in order to fit it into the given geometrical constraints of the Velis Electro cowling without compromising heat transfer surface. For a semi-circular entry ($width^2/A_{in} \simeq 2.5$) Fig. 5 of [41] gives $C_{D,\text{datum}} \approx 0.26$. At the other extreme (zero flow) [41] shows that the term $C'_D - C_{D,\text{datum}}$ is about 0.4 at $M \approx 0.2$, giving 0.66 in case of complete spillage (related to the inlet area).

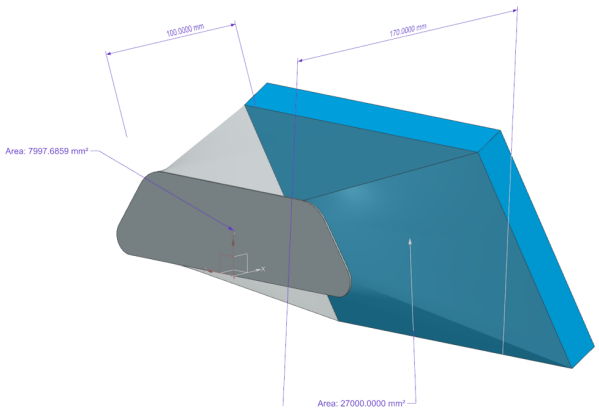

Figure 3.23: *Inlet–diffuser–HE* geometry approximation in NX.

BMS

Second part of Velis Electro's thermal management, pictured in the Figure 3.25, employs a liquid-cooling loop featuring a radiator and two electrically driven pumps arranged in series, situated just behind the aft battery pack. Cooling air enters through an intake on the left side of the fuselage and exits beneath the aircraft. To support battery temperature control during charging, a pair of high-power axial fans is mounted downstream of the radiator (Figure 3.21 [35]). Their operation is regulated and monitored by the Battery Management System (BMS) [33]. Although mentioned here for the completeness of the TMS description, this cooling loop won't be part of the comparison as the fan-augmented flow is not currently implemented in the pre-sizing tool but is a valid point for the future development of the software.

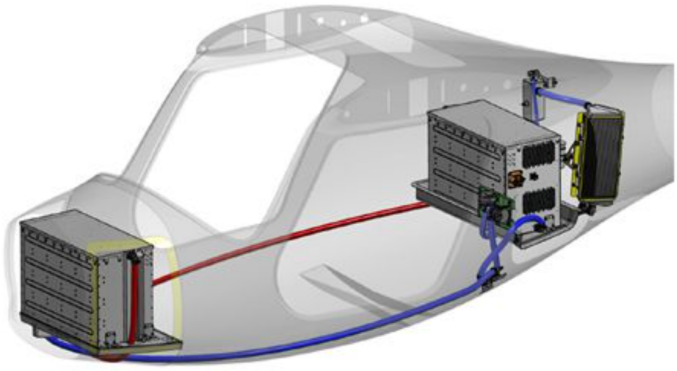

Figure 3.24: Velis Electro battery cooling system [35].

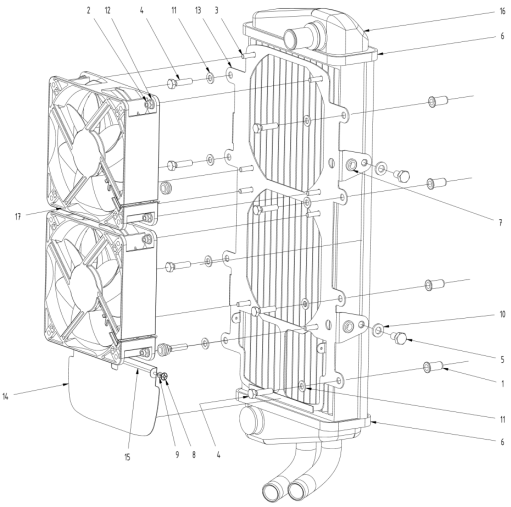

Figure 3.25: Velis Electro radiator and fans assembly in the BMS cooling loop [35].

3.7.2 Flight data

Besides access to the hardware, Oskar Dahl has also provided an example of the data file logged throughout the whole flight mission of the Velis Electro. It has been plotted in the Figure 3.26 and gives and outlook on some of the components' temperatures that are important to evaluate current design of the cooling system. Especially informative is the behaviour of coolant temperature for certain motor power levels as it never reaches limit temperature for both motor and the inverter for take-off ambient temperature around $OAT = 15\ °C$, but if the $\Delta ISA = 25\ °C$ has been considered per TCDS of the motor [31], coolant temperature at the inverter inlet could be close to its limit of 60 $°C$ at the top of climb.

Until reaching cruise altitude of 3000 m, temperatures are steadily rising, which means that the heat exchanger is not rejecting enough heat. Temperatures start to level off around the 15th minute of the flight, after the motor power (throttle) has been reduced to around 20 kW which is the cruise stage.
Comparing mean motor's $RPM = 1750$ during that stage and mean $Torque = 400\ Nm$ (Fig. 3.27) with the efficiency map (3.19), yields around 94% efficiency. That gives heat rejected by the motor around $\dot{Q}_{motor} = 20 * (1 - 0.94) = 1.2\ kW$. Another contribution is from the inverter which can be estimated as

$$\dot{Q}_{inverter} = \dot{m}_{coolant} c_{p,coolant} (T_{inverter,\,out} - T_{inverter,\,in}) = 0.1* \tag{3.21}$$

Given a water–glycol 50/50 coolant with density and specific heat at 25°C:

$$\rho = 1123\ \mathrm{kg/m^3}, \tag{3.22}$$

$$c_p = 3277\ \mathrm{J/(kg\,K)}. \tag{3.23}$$

As coolant flow rate is not disclosed anywhere in the logged data, minium volumetric

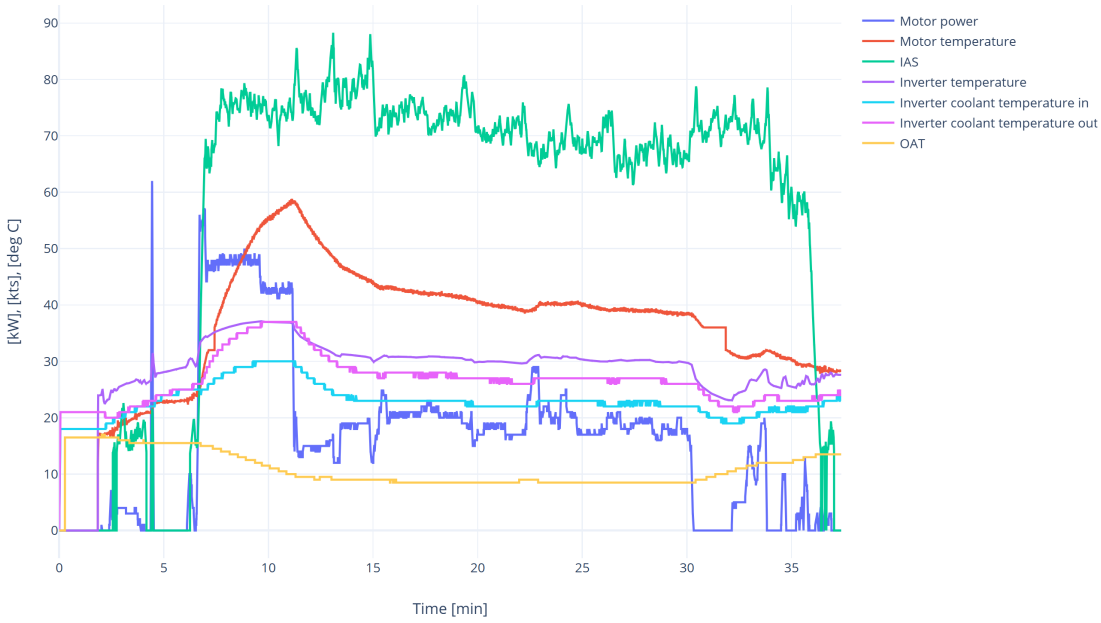

Figure 3.26: Velis Electro flight data - temperatures, power. Courtesy of Oskar Dahl

flow rate from TCDS is taken [31]

$$\dot{V} = 0.1\ \mathrm{L/s} = 0.1 \times 10^{-3}\ \mathrm{m^3/s} = 1.0 \times 10^{-4}\ \mathrm{m^3/s}. \tag{3.24}$$

Hence the mass-flow rate through the inverter is

$$\dot{m} \;=\; \rho\,\dot{V} \;=\; 1123\ \mathrm{kg/m^3} \;\times\; 1.0 \times 10^{-4}\ \mathrm{m^3/s} \;=\; 0.1123\ \mathrm{kg/s}. \tag{3.25}$$

The coolant inlet mean temperature is $T_{\mathrm{in}} = 23\,^{\circ}\mathrm{C}$ and the outlet temperature is $T_{\mathrm{out}} = 27\,^{\circ}\mathrm{C}$, so

$$\Delta T \;=\; T_{\mathrm{out}} - T_{\mathrm{in}} \;=\; 27 - 23 \;=\; 4\ \mathrm{K}. \tag{3.26}$$

The heat-rejection rate from the inverter at steady state is therefore

$$\dot{Q}_{inverter} = 0.1123\ \mathrm{kg/s} \;\times\; 3277\ \mathrm{J/(kg\,K)} \;\times\; 4\ \mathrm{K} \tag{3.27}$$

$$= 1.47\ \mathrm{kW}. \tag{3.28}$$

Giving $\dot{Q}_{total} = 2.67\,kW$. Important unknown value, which is exact coolant mass flow used in the loop, could change that heat transfer estimation quite significantly. Another thing is coolant temperature after the motor. If it assumed equal to the motor temperature itself, then coolant temperature drop at the HE from 40 to $23°C$ would require $\dot{Q}$ of around 7 kW which is much higher than the value calculated in the beginning. Due to to this ambiguity, higher of the two will be assumed as the design value.

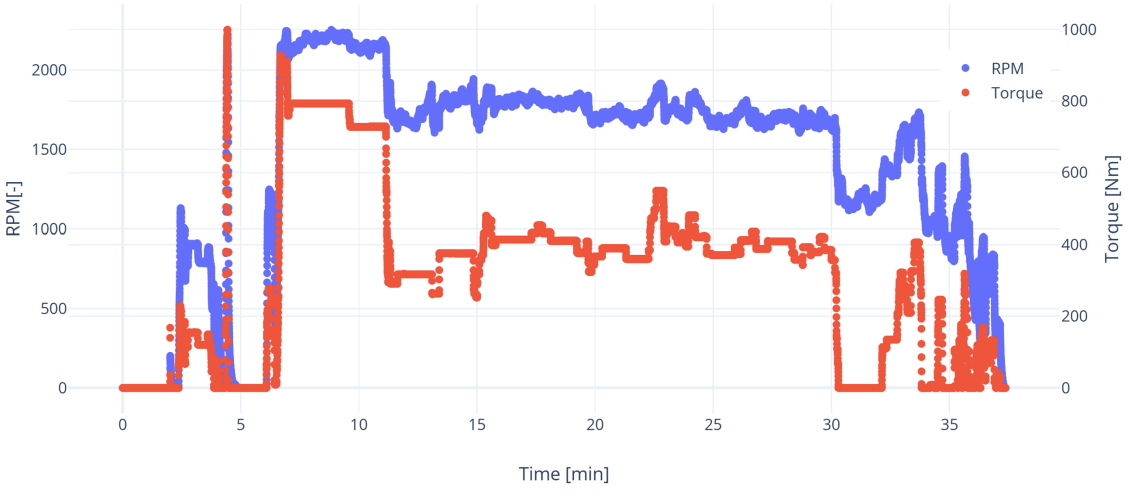

Figure 3.27: Velis Electro flight data - Torque and RPM. Courtesy of Oskar Dahl

Outlet

Outlet that is employed at Velis (Fig. 3.28) makes the flow going out of the cooling better aligned with the freestream [42]. This allows for better static pressure recovery and lower loss of total pressure as the re-compression continues in the free stream, similarly to the off-surface pressure recover [20]. This type of outlet, together with two landing gear supports might also cause recirculation, which results in a zone of negative pressure, which can be modeled in the design tool using negative c_p at the outlet. As that outlet's pressure coefficient isn't exactly known, three design estimations for $c_p = [0, -0.1, -0.2]$ will be analysed. In general, lowered static pressure at the outlet creates suction that helps to pull the flow through the systems that otherwise would be starved.

Figure 3.28: Velis Electro outlet. Courtesy of Oskar Dahl.

Most of the information about the Velis Electro presented in previous sections will

be used to compare and discuss the output geometry and thermal characteristics of the design coming from the tool to the approximation of the system employed at the Velis Electro.

4
Results

4.1 Validation

In this section results of the validation with experimental studies, are presented, for main methodologies driving the design tool.

4.1.1 Integral heat exchanger model

Test results are provided for fins whose exact geometry is not fully specified. Consequently, the model employs fins from the Kays and London databank that most closely match the tested configuration. As a result, a perfect agreement between the model predictions and test data is not anticipated.

Two of the implemented models gave slightly different results between data points as for example at the coolant massflow of 3 liters per second visible in the Figure 4.1. $\varepsilon - NTU$ matched first two data points with very small error and fell off at heat rejection prediction for two highest velocities, heavily under-predicting heat exchange at 10 m/s by 13.5% and mean absolute percentage error (MAPE) over all data points of 5.5%. On the contrary, integral heat exchanger model over-predicted heat exchange at lower velocities but matched closer the heat transfer for the higher ones achieving lower MAPE of 3.65% at this coolant mass flow.

Important validating point of these results is that integral model aligns with $\varepsilon - NTU$ formulation if marching properties update is turned off, and bulk average properties are used instead.

Although 3.7% seems to be of a quite good accuracy (experimental data states 5% error measurement error) for a pre-sizing tool, it is important to look at the whole range of the analysed data presented in Tables 4.1–4.3. Most of the heat rejection MAPE are between 2–4% while pressure drop coefficient is in general poorly predicted, especially for the velocity of 2 m/s. Regarding above, error for the velocity of 7 m/s is surprisingly low, raising question if there is a way to tweak the model to work better at certain velocities. Exact behavior of this integral model regarding $\dot{Q}$ and ζ_{HE} is visible in the Figures 4.2–4.4.

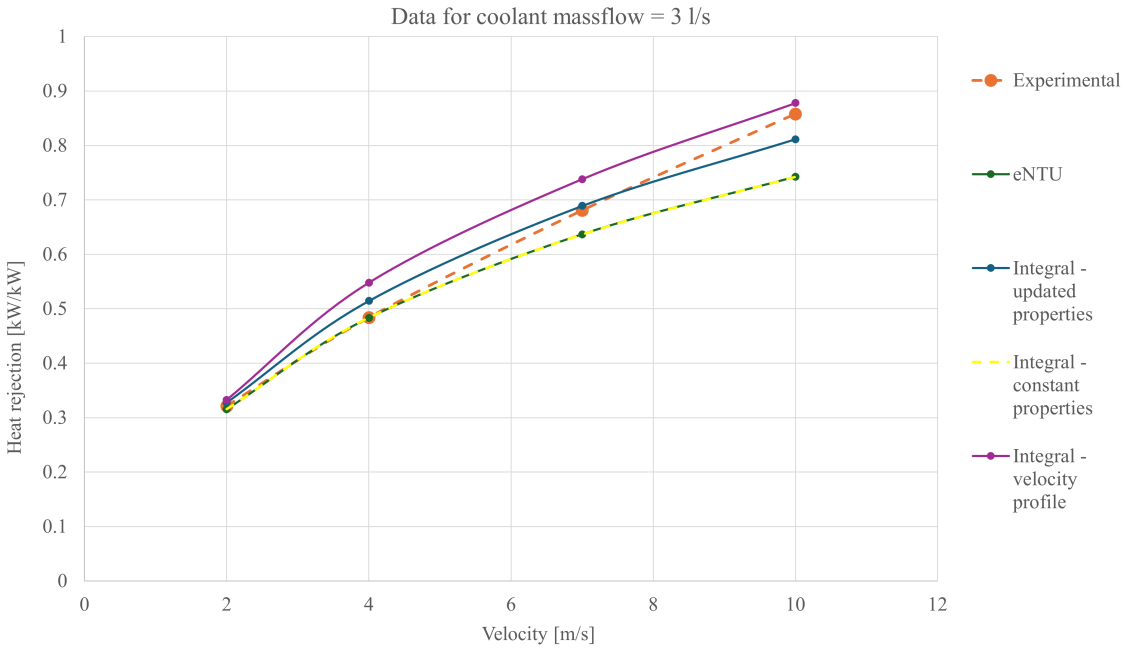

Figure 4.1: Comparison of heat exchanger models for one coolant mass flow with experimental data

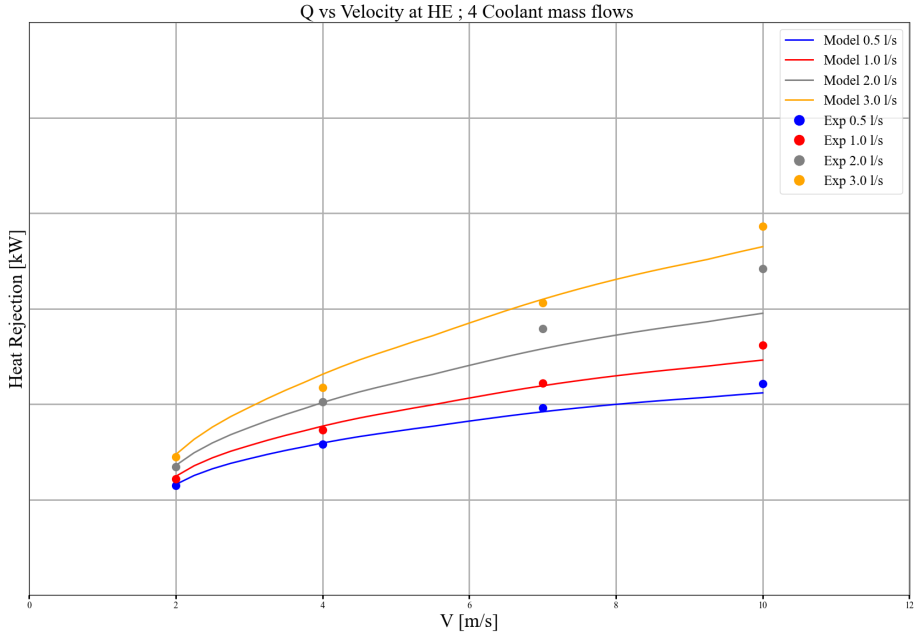

Figure 4.2: Comparison of heat exchanger models for fixed coolant mass flows with experimental data - heat rejection

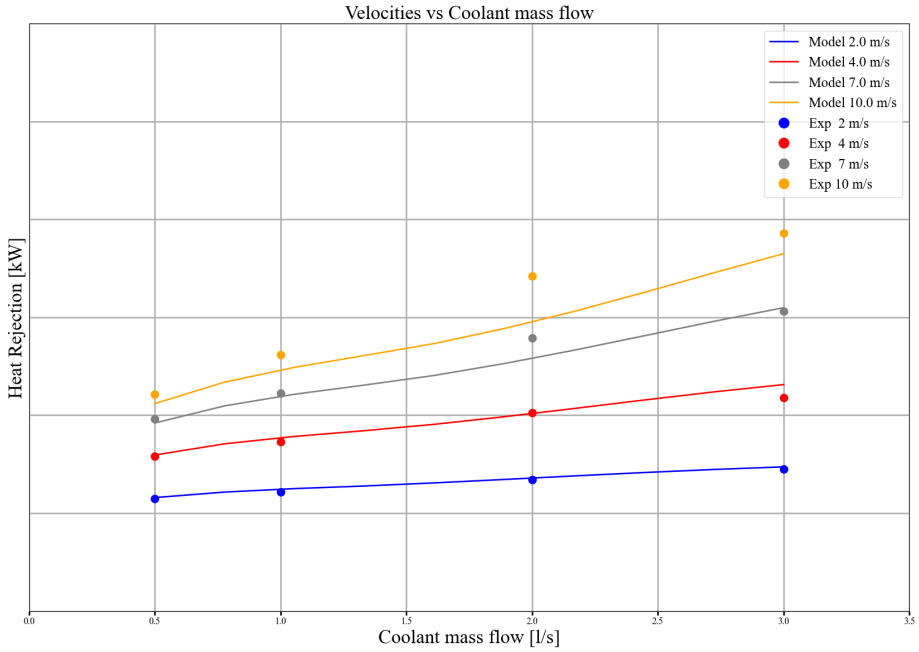

Figure 4.3: Comparison of heat exchanger models for fixed velocity with experimental data - heat rejection

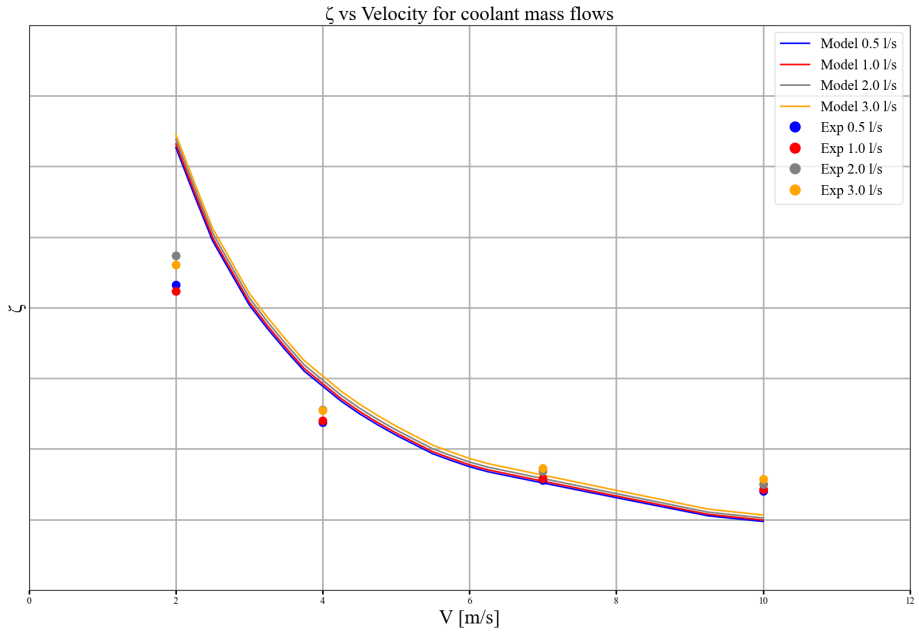

Figure 4.4: Comparison of heat exchanger models for fixed coolant mass flows with experimental data - total pressure drop coefficient

Table 4.1: Relative percentage error of heat rejection versus velocity for tested coolant mass flows

Mass flow (l/s)	$V = 2\,\mathrm{m/s}$	$V = 4\,\mathrm{m/s}$	$V = 7\,\mathrm{m/s}$	$V = 10\,\mathrm{m/s}$	MAPE (%)
0.5	0.91	0.98	-2.08	-4.27	2.06
1.0	2.17	2.39	-1.32	-5.94	2.96
2.0	1.19	-0.32	-7.51	-13.70	5.68
3.0	1.74	6.25	1.14	-5.48	3.65

Table 4.2: Relative percentage error of heat rejection versus coolant mass flow for tested velocities

Velocity (m/s)	$qv = 0.5\,\mathrm{l/s}$	$qv = 1.0\,\mathrm{l/s}$	$qv = 2.0\,\mathrm{l/s}$	$qv = 3.0\,\mathrm{l/s}$	MAPE (%)
2	0.91	2.10	1.19	1.74	1.49
4	0.98	2.29	-0.29	6.25	2.45
7	-2.08	-1.44	-7.45	1.14	3.03
10	-4.27	-6.06	-13.62	-5.48	7.36

Table 4.3: Relative percentage error of pressure drop coefficient versus velocity for tested coolant mass flows

Mass flow (l/s)	$V = 2\,\mathrm{m/s}$	$V = 4\,\mathrm{m/s}$	$V = 7\,\mathrm{m/s}$	$V = 10\,\mathrm{m/s}$	MAPE (%)
0.5	30.79	11.72	-1.15	-12.55	14.05
1.0	33.35	11.92	-0.99	-12.76	14.76
2.0	24.36	9.28	-2.90	-13.62	12.54
3.0	27.85	10.78	-2.74	-14.28	13.91

Integral model with velocity profile

Implementing velocity profile (Fig. 4.6) for the $AR = 4, L/h = 2$ diffuser to get test matching flow conditions at HE face, further increased overshoot of the heat transfer and resulted in MAPE of 6.8%, with peak error at the velocity of 4 m/s (Fig. 4.1) and the lowest of 2.3%. for 10 m/s. Sharp rise in the velocity on the sides comes from the data sampling in the post-processing of the CFD results, which extracted velocity of 0 at the wall, and next point already inside the developed profile, missing the exact profile development behavior (Fig. 4.5) and interpolating linearly between those points. This issue could be solved by refining the CFD data sampling (especially near the walls) while extracting the data for the future implementations.

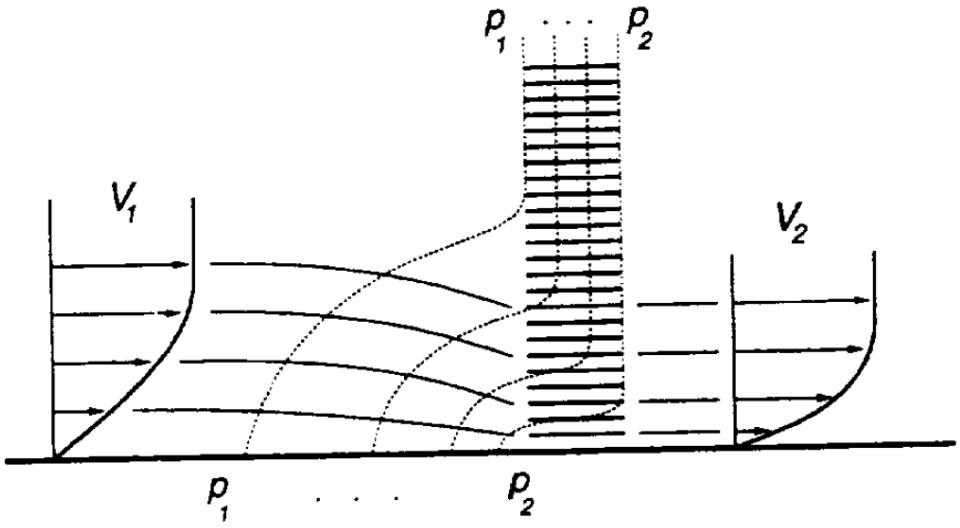

Figure 4.5: Boundary layer velocity profiles in proximity of HE. Adapted from Drela [37]

Conclusions

Important difference this model has while comparing to the experimental setup, is that this profile has been only implemented for the HE flow arrangement where the tubes are running vertically, while the experimental results (as well as both $\varepsilon - NTU$ and analytical integral model) have tubes running horizontally. It makes the balance between number of fins per tube and number of tubes slightly different yet is a necessary simplification, with implementing other flow arrangements for this integral model left as an important point for the future development. Implementing this velocity profile for the horizontal tubes would have to include the difference in local mass flow on top and bottom side of the tube, while tubes running vertically make simplifications in this regard possible.

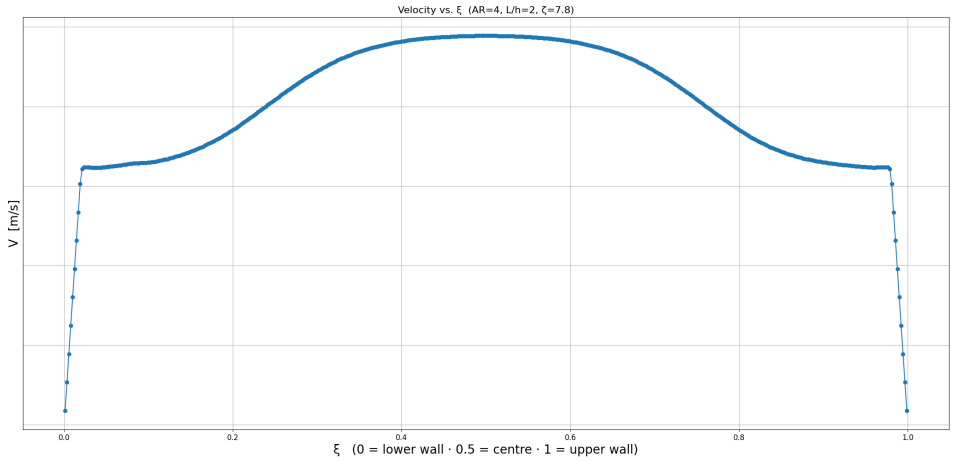

Figure 4.6: CFD-based interpolated velocity profile at the HE face for $V_{HE} = 10\frac{m}{s}$

Conclusions

Integral formulation with constant thermal properties aligns with the $\varepsilon - NTU$ code which indicates proper implementation of the integral model. Furthermore, regular integral model provides a satisfactory initial estimate of heat exchanger performance without requiring computationally expensive and time-consuming CFD simulations. The discrepancies observed in predictions of ζ_{HE} are likely due to differences between the fin geometry and layout assumed in the model and those of the tested heat exchanger, which are largely unknown. $\varepsilon - NTU$ method alone, provides good enough foundations for initial pre-sizing.

Integral model infused with CFD-derived velocity profile, diverges slightly from the results of $\varepsilon - NTU$ and keeps a trend of overshooting the heat transfer for all the data points, which seems to be influenced mostly by the marching local Nu_h formulation. Another possible reason of difference in results might come from the exact properties of the tubes (material, thickness) which can influence the results. Tubes implemented in the models are 3003-O aluminum alloy but material and thickness are not disclosed in the results of an experiment and are influencing the heat transfer by wall terms contribution to local overall heat transfer coefficient U.

4.1.2 Diffuser CFD

Validation of the diffuser against Gibson's experiments [17], as introduced in section 3.3.1, shows that the computation using finest 2D mesh and k-ω SST turbulence model outputs the lowest absolute error of 3.51% relative to the experimentally measured diffuser loss of 38%. Comparison between turbulence models has been summarized in Table 4.4.

Table 4.4: CFD model loss and error comparison for different turbulence models

Turbulence model	k-ε	k-ω SST	Spalart-Allmaras
Loss [%]	27.90	39.33	30.98
Error [%]	26.57	3.51	18.48

Error of this magnitude is very satisfactory considering the analysed diffuser is experiencing the region of separated flow visible in the Figure 4.7 and the computations were in 2D domain.

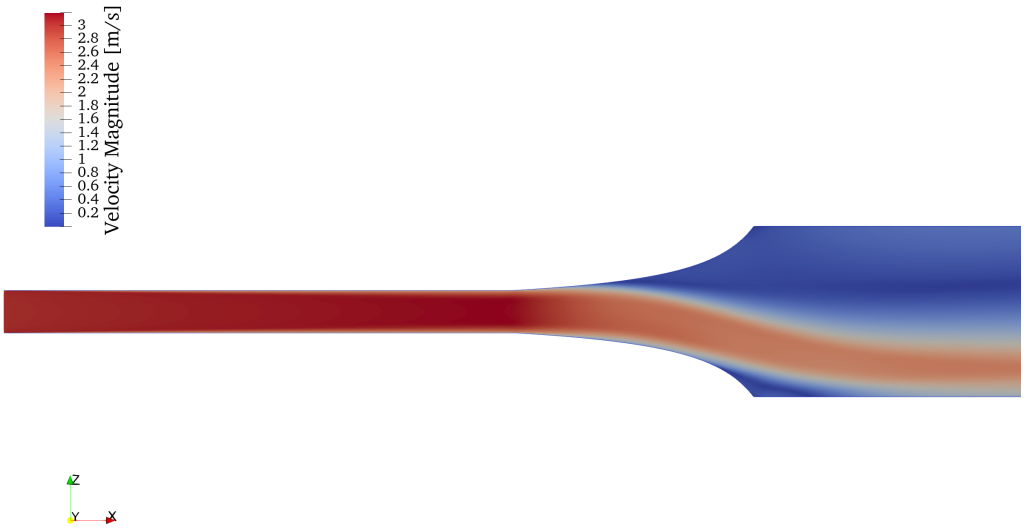

Figure 4.7: Velocity magnitude contour plot for the diffuser CFD methodology validation.

4.1.3 Conclusions

Analysing y^+ values indicates correct choice of the first prismatic layer height as it reaches maximally 0.63 at the inlet, where the boundary layer hasn't seen growth yet. Furthermore, although not exactly the same case, as there was no porous element inside, this results are the foundation for the choice of the setup for the future analyses that surrogate models developed for the tool are based on.

4.2 CFD studies

Numerous CFD analyses were conducted in order establish proposed concept of surrogate models and provide foundational idea for future development of the knowledge based tool.

4.2.1 Diffuser - heat exchanger coupling

As already introduced in the section 3.4.2 on the methodology of surrogate models creation, ζ_{HE} makes impact on the flow inside the diffuser, as explained in the theory of the filling effect. For moderate total pressure drops imposed at the HE, $\zeta_{diffuser}$ drops and then again rises, when the ζ_{HE} is further increased. This effect for the diffusers of AR 4 and 7 has been plotted in the Figure 4.8.

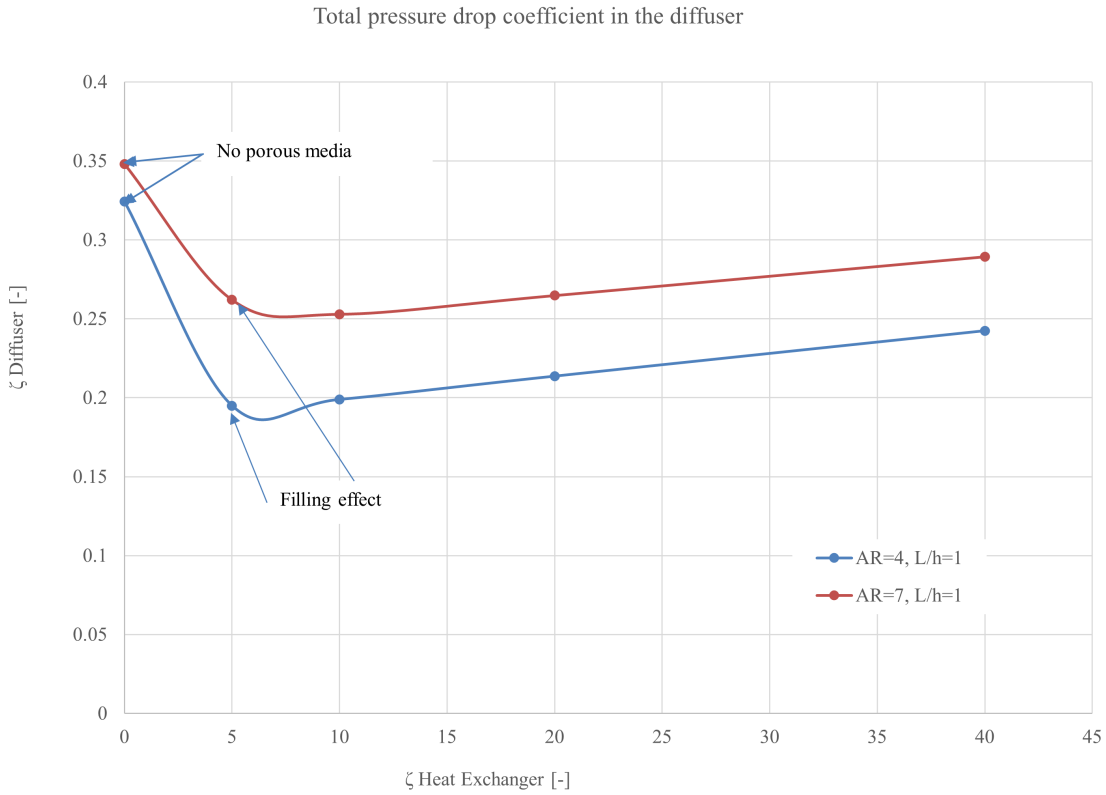

Figure 4.8: $\zeta_{diffuser}$ vs. ζ_{HE} from CFD computations for two area ratios

Velocity profile analysis, done in section 3.4.2 and also visible in the compound Figure 4.9 leads to further conclusion that increasing the pressure drop, decreases the flow non-uniformity which according to theory results in higher performance of heat exchanger regarding both pressure drop and heat transfer [37, 30]. Figure 4.9 shows how heat exchanger turns the flow into purely axial direction (W=0), and how increased ζ_{HE} decreases non-uniformity Ψ, mostly by decreasing the magnitude of the velocity component that is perpendicular to the $x - axis$.

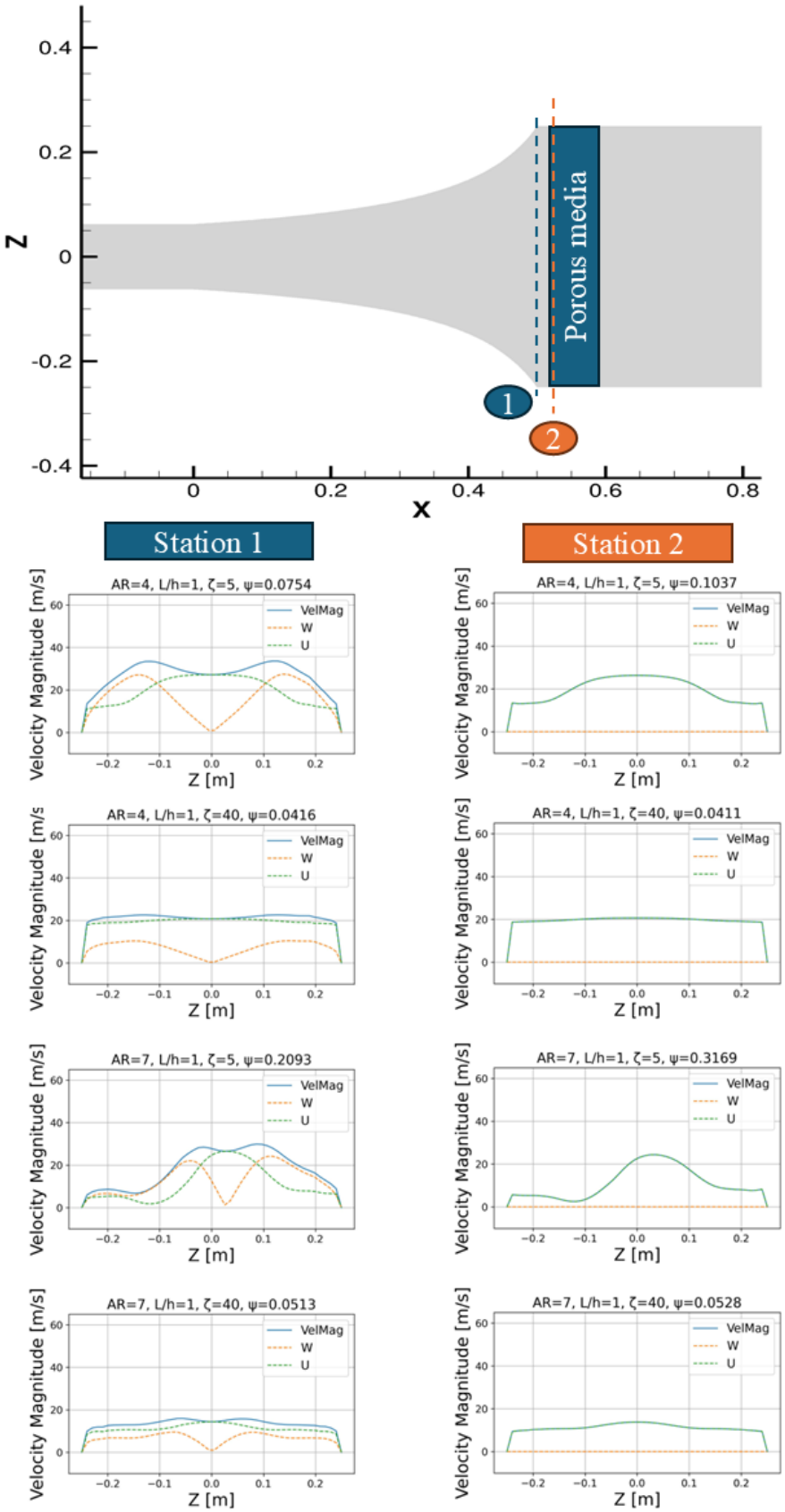

Figure 4.9: Velocity profiles components and magnitude comparison at diffuser outlet (Station 1) and exactly at the HE inlet (Station 2)

4.3 Design for Velis Electro

Pre-sizing tool has been run in 2 different modes in order to compare the design routines and evaluate accuracy of the genetic algorithm. Initial parameters related to geometry included constant inlet height of 50 mm, diffuser length ratio of $L/h = 1.5$ and $c_{p,out} = [0, -0.1, -0.2]$. Atmospheric conditions are for the cruise flight described as part of the design case methodology. To cool down the water-glycol coolant to $23°C$ from $40°C$ coming out of the motor, the required design needs to provide 7 kW of heat rejection, so this is the required amount that the algorithms are searching for.

4.3.1 GA vs. Sweep

Sweep of the x design vector components chosen based on the design of Velis, discussed in chapter 3

$$x = [HE_{width}, HE_{thickness}, HE_{height}]$$

with parameters defined as 35 linearly spaced values between:

$$\begin{aligned} w_{0,\min} &= 0.15, \quad w_{0,\max} = 0.30, \\ t_{0,\min} &= 0.01, \quad t_{0,\max} = 0.04, \\ h_{0,\min} &= 0.15, \quad h_{0,\max} = 0.35. \end{aligned}$$

As visible in the Figure 4.10, there is a clear front of the best designs which should

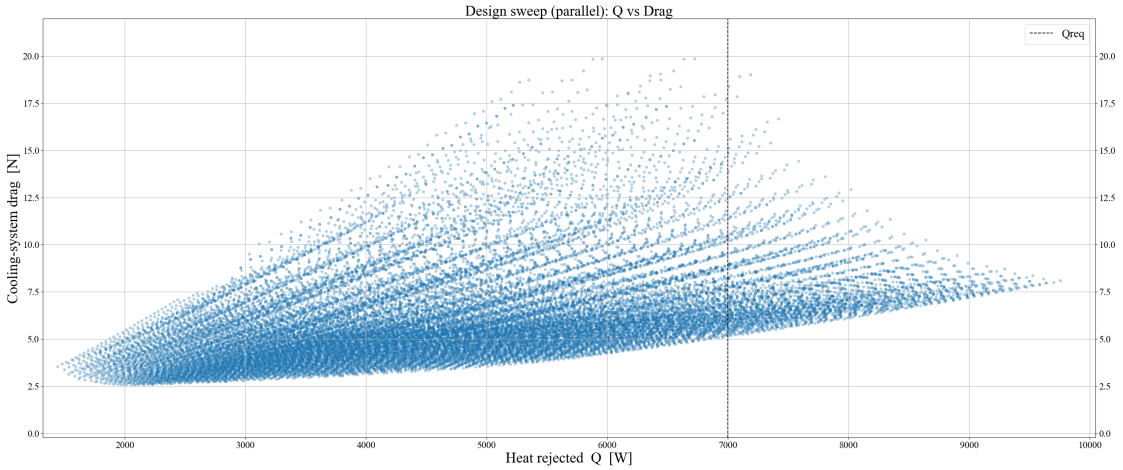

Figure 4.10: Cloud of designs at $c_{p,outlet} = 0$ - parameters sweep

be clear indication for the designer, which design is the best considering cooling drag. In the background, there is also core weight that should be taken into secondary consideration, depending on which parameters is limiting the design. Following this logic, design that realizes required cooling has been chosen from the front of the best designs in proximity of the Q_{req} line. That is an example of manual evaluation. Similar plot, but containing history of the GA is in the Figure 3.1. Designs from those two approaches has been compared in Table 4.5 in order to evaluate accuracy of GA in terms of design automatization.

Table 4.5: Comparison of design outputs at $c_{p,\text{out}} = 0$ for Genetic Algorithm vs. Parametric Sweep

Metric	Genetic Algorithm	Parametric Sweep
Q [kW]	6.931	6.997
Drag [N]	5.33	5.14
$\Delta C_d[d.c.]$	7.58	7.3
Weight [kg]	2.15	2.48
$T_{\text{coolant,in}}$ [°C]	40	40
$T_{\text{coolant,out}}$ [°C]	22.77	22.60
w [m]	0.224	0.191
t [m]	0.032	0.040
h [m]	0.350	0.343

Heat Transfer (Q)

Design chosen from the parametric sweep achieves $Q = 6.997\,\text{kW}$, which is approximately $0.066\,\text{kW}$ (1%) higher than the Genetic Algorithm solution at $Q = 6.931\,\text{kW}$.

Aerodynamic Drag

The drag produced by the Normal Sweep design is $5.14\,\text{N}$, while the Genetic Algorithm converged to design yielding $5.33\,\text{N}$. In other words, the design extracted from the sweep has roughly 3.7% lower drag.

Total Drag Coefficient

Both approaches produce nearly identical total drag coefficients: $C_{d,\text{cooling}} = 7.58\ d.c.$ for the Genetic Algorithm versus 7.3 *d.c.* for the one coming from the sweep. Comparing both results to the constant $C_{D,datum} = 2.2\ d.c.$, contribution from the momentum to the total drag is substantial and results in only around 10 d.c. in total. This might lead to a conclusion that regarding core sizing, more relevant parameter could be the weight, since the analyzed ultralight aircraft has only 170 kg of payload [34].

Weight

The GA design is lighter at $2.15\,\text{kg}$, compared to $2.48\,\text{kg}$ for the Normal Sweep. This corresponds to a mass saving of approximately $0.33\,\text{kg}$ (0.2% of the payload) in favor of the GA design.

Coolant temperatures

Both designs start from the same inlet temperature 40°C. GA design has an outlet temperature 22.77°C, whereas one chosen from the cloud achieves 22.60°C. Hence, the second one removes slightly more heat as a result of slightly higher heat rejection.

Geometric Dimensions (w, t, h)

In the Genetic Algorithm design, the width is $w = 0.224\,\text{m}$, thickness is $t = 0.032\,\text{m}$, and height is $h = 0.350\,\text{m}$, employing $AR = 7$ diffuser based on the (constant) inlet height of $0.05\,m$. In the sweep design, the width is $w = 0.191\,\text{m}$, thickness is $t = 0.040\,\text{m}$, and height is $h = 0.343\,\text{m}$. In other words, the GA solution opts for a wider and shallower core, with higher frontal area, whereas the hand-picked solution uses a narrower but thicker core, trading frontal area for core thickness. Size of the original heat exchanger estimated in the section method, is very similar in terms of width and thickness but smaller in terms of height (170 mm estimated).

Trade-Off Summary

The Genetic Algorithm design is lighter (6.16 kg) but sacrifices approximately 0.07 kW of cooling capacity and incurs slightly higher drag (5.33 N). In contrast, the other, chosen design delivers higher cooling (6.997 kW) and lower drag (5.14 N) at the cost of about 0.28 kg extra mass.

Selection Criteria

If minimizing mass is the primary objective, the Genetic Algorithm design (6.16 kg) is preferable. If maximizing heat removal (or minimizing drag) is critical, there exists a better design on the cloud (6.997 kW, 5.14 N, 6.4386 kg) which would be the better choice.

Sanity checks

For sanity checks of the specific stages of the system, the tool plots flow conditions at inlet and outlet of each component. Figures 4.11-4.14 present flow conditions for the GA design and Figure 4.15 gives a quick outlook on a bulk size of the components and the system (lengths of inlet and outlet are currently only a visual parameter). This evaluation can be used to perform further validation of the system.

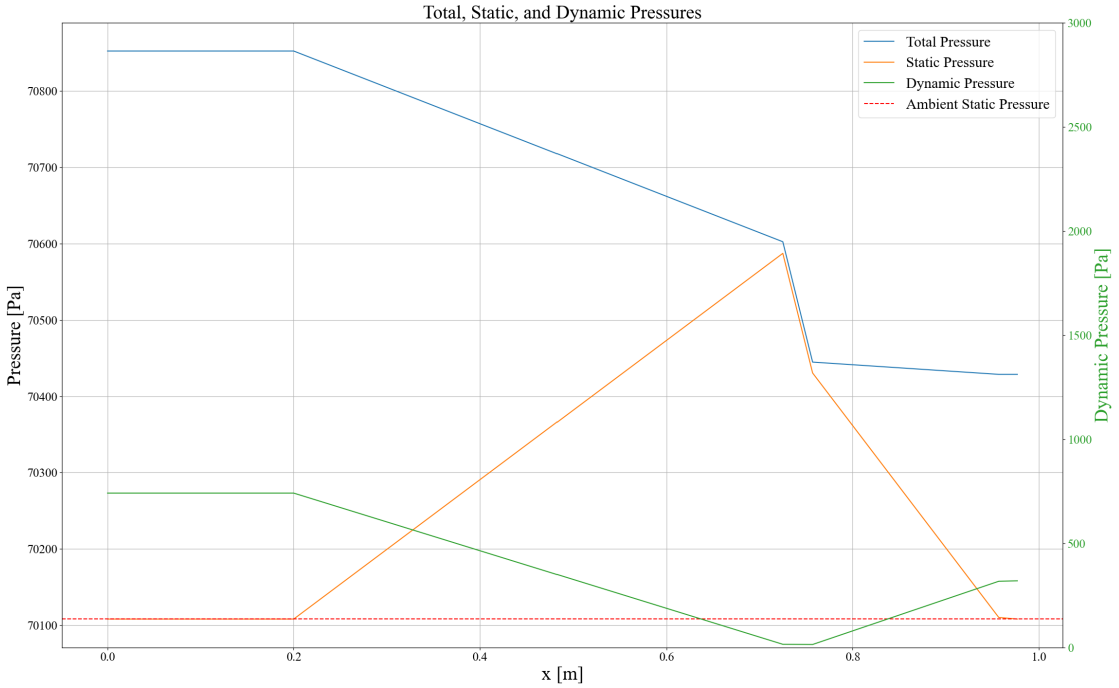

Figure 4.11: Pressure distribution through the cooling system - $c_{p,outlet} = 0$, GA

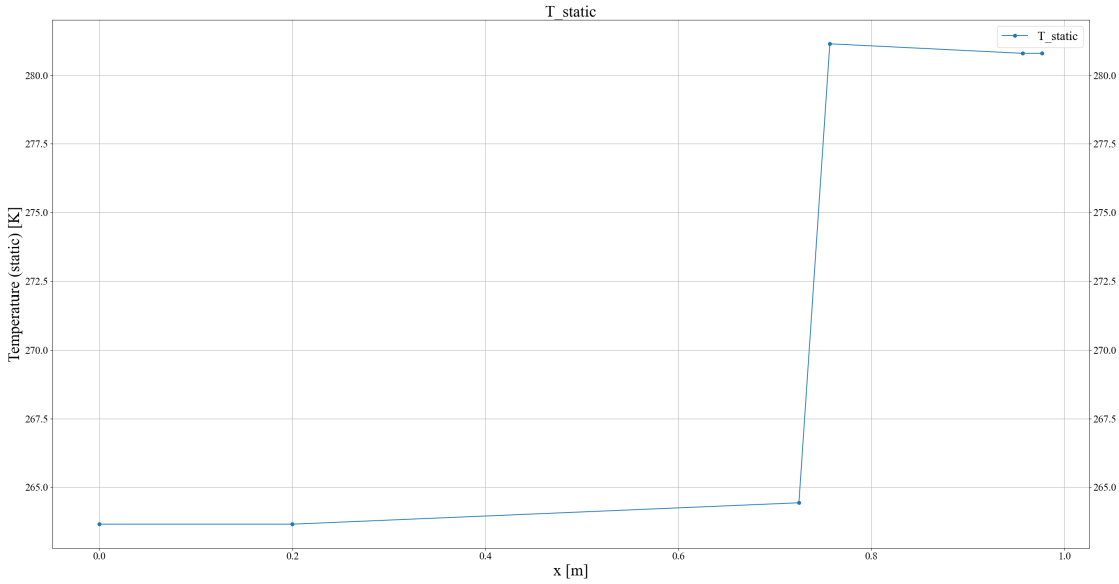

Figure 4.12: Temperature distribution through the cooling system - $c_{p,outlet} = 0$, GA

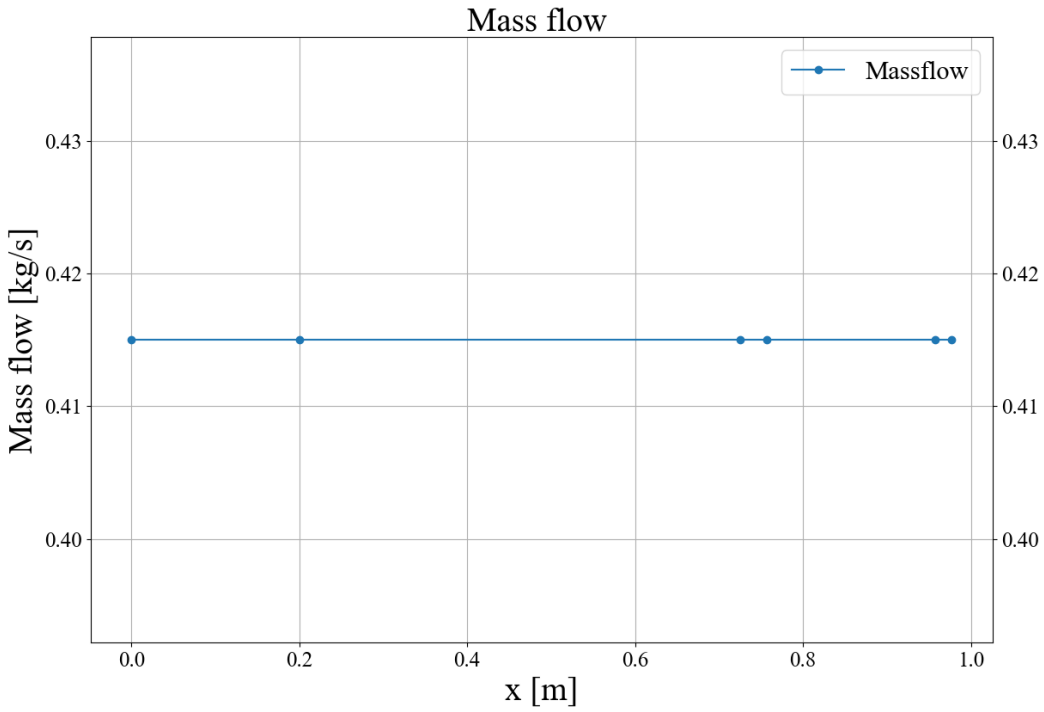

Figure 4.13: Mass flow through the cooling system - $c_{p,outlet} = 0$, GA

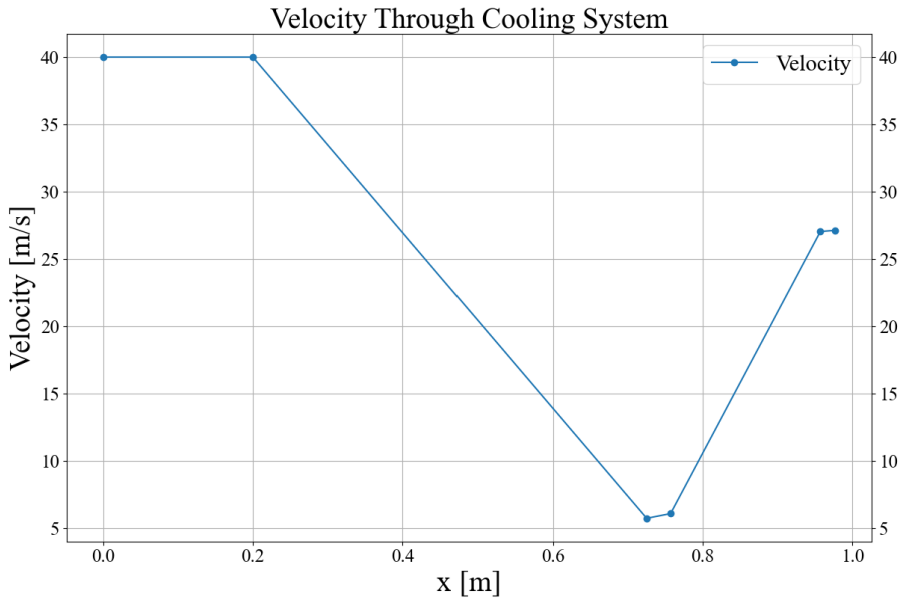

Figure 4.14: Velocity distribution through the cooling system - $c_{p,outlet} = 0$, GA

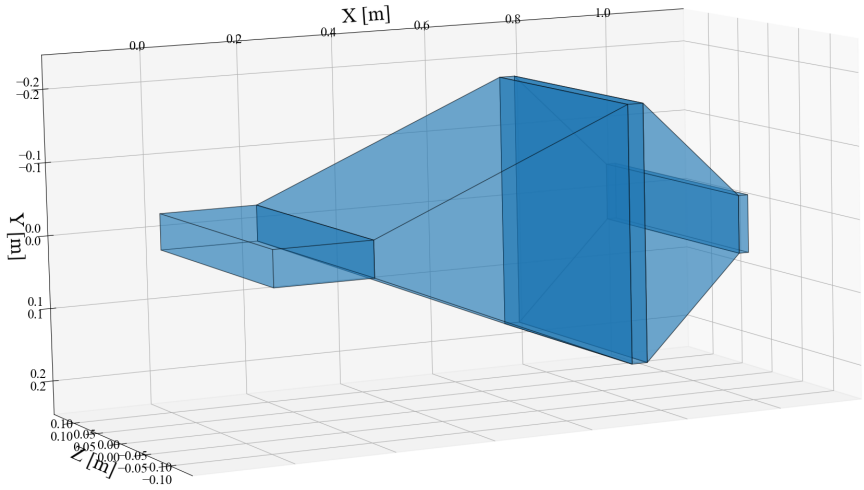

Figure 4.15: Bulk size of the cooling system - $c_{p,outlet} = 0$, GA

4.3.2 Design for negative c_p

Imposing negative c_p at the oulet, as if there was for example recirculation caused by the outlet flap, leads to lower cooling drag due to the momentum [42]. Important note is that that the real advantage of this configuration would be at configurations with higher total pressure drops in the system - so more extreme designs with smaller length of the diffuser, thicker heat exchanger taking less space. What isn't taken in consideration in this study is the drag that would the recirculation and flap impose on the system, which might increase the total C_D well beyond what is taken into account by the current implementation. That's why this configuration should be further studied and implemented for example using surrogate model philosophy presented in this thesis.

Table 4.6 presents output from GA as if the design was made for the negative c_p at the outlet. It converged to heat transfer in very similar proximity to 7 kW, but of a different width, thickness, height combinations resulting in slightly different weights.

Table 4.6: Genetic Algorithm results for varying $c_{p,\text{out}}$

$c_{p,\text{out}}$	Q [kW]	Drag [N]	$C_{d,\text{cooling}}$ [d.c.]	Weight [kg]	T_{out} [°C]	w [m]	t [m]	h [m]
0	6.931	5.33	7.58	2.15	22.770	0.224	0.032	0.350
−0.1	6.944	4.01	5.68	2.379	22.735	0.196	0.038	0.342
−0.2	6.946	2.95	4.19	2.287	22.730	0.210	0.035	0.350

4.4 Design from Velis Electro

Analysis of the approximate design that is employed at Velis Electro has also been conducted in order to estimate accuracy of the tool and its applicability. This time

tool has been run in the analysis mode which provides characteristics of chosen design.

Initial analysis shown that for $c_{p,outlet} = 0$, total pressure drop in the system, mainly due to the heat exchanger, leaves not enough dynamic pressure for the flow to reach required mass flow at the outlet. One of the possible solutions that Velis is using, is applying suction at the outlet to help the flow. Assuming $c_{p,outlet} = -0.1$, system of exactly this size is getting realizable.

To achieve better alignment with the design, one further assumption regarding the coolant temperature must be made. As shown in Figure 4.16, the inverter's temperature is actually 3–4 °C higher than that of the coolant flowing out of its cold plate. Extrapolating this behaviour to the motor–coolant thermal interface, we assume a coolant outlet temperature of 36 °C instead of 40 °C, which reduces the theoretical heat-transfer requirement to 5.35 kW.

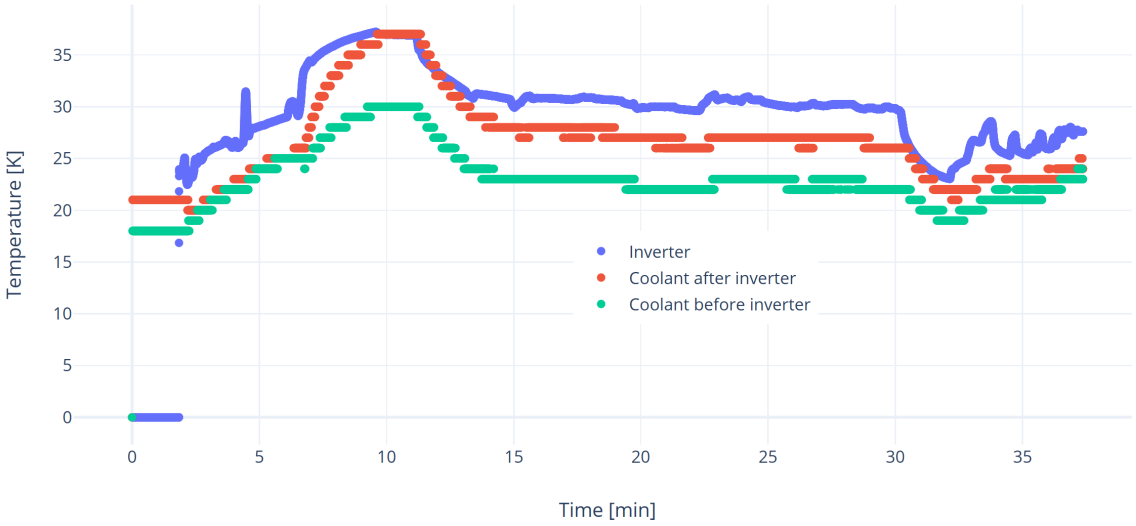

Figure 4.16: Pipistrel Velis Electro flight data - Inverter related temperatures

The results of the analysis for the flight conditions at which the data were logged are presented in Table 4.7.

Table 4.7: Results of the reverse engineered ram-air cooling system

$c_{p,\text{out}}$	Q [kW]	Drag [N]	$C_{d,\text{cooling}}$ [d.c.]	Weight [kg]	T_{out} [°C]	w [m]	t [m]	h [m]
−0.1	4.280	8.30	11.76	1.15	24.30	0.180	0.04	0.180

According to the tool, heat exchanger employed at Veli Electro is able to cool down the coolant to the temperature of $24.3°C$ while contributing 11.76 drag counts to the total drag of the aircraft, due to low velocity at the outlet. Although the drag is higher than the designs for the 7 kW requirement proposed before, its weight has been estimated as 1.15 kg which is around two times lower.

4.5 Velis Electro vs. GA vs. SLSQP

Finally, a comparison of the optimisation results for the heat-rejection value determined in the previous analysis was carried out to assess the accuracy of the gradient-based algorithm.

A difficulty with SLSQP, owing to its gradient-based nature, is the choice of the initial guess vector x_0, which strongly influences the solution to which the algorithm converges. When the system is infeasible because the total pressure drop is too high, a drag penalty is applied. Because the drag function possesses many local *minima*, initialising the SLSQP algorithm with a large HE-core thickness causes it to become trapped in a penalised local minimum (Figure 4.17a). If, instead, the algorithm is started from the minimum allowable thickness, it converges to a feasible optimum that satisfies the constraint tolerances (Figure 4.17b).

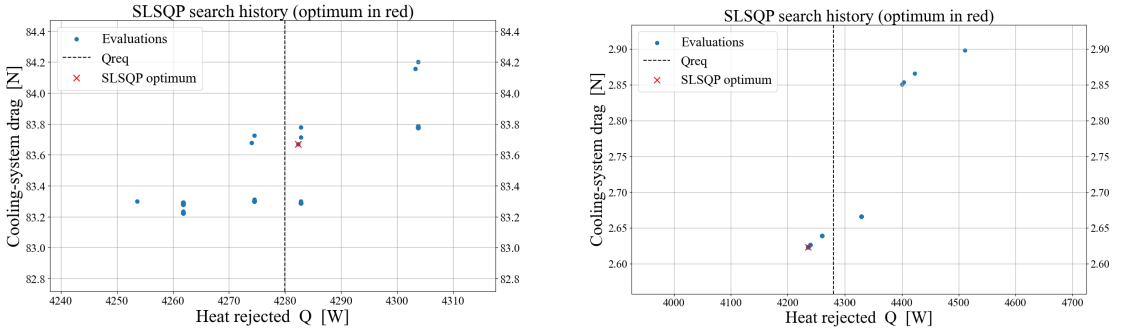

(a) Infeasible local minimum (high initial total pressure drop)

(b) Feasible local minimum (low initial total pressure drop)

Figure 4.17: Effect of the initial guess vector on the SLSQP solution

This behaviour is a known drawback of algorithms that rely on gradient information [24]. Techniques such as *basin hopping*, which performs large jumps away from a local minimum in the hope of landing in another basin of attraction [53], could be explored in future work to improve the global-minimum search.

The feasible designs obtained with SLSQP and the GA are summarised in Table 4.8. Both algorithms converged to designs within a 1.5 % error band, which had been set as the tolerance for the required Q. Because the objective for both optimisers was drag minimisation, their designs are roughly 500–600 g heavier than the configuration used on the Velis Electro, but they achieve a reduction of 7–8 drag counts.

Table 4.8: Design comparison for SLSQP, GA, and Velis Electro

Configuration	Q [kW]	Drag [N]	C_d [–]	Weight [kg]	$T_{h,\text{out}}$ [°C]	w [m]	t [m]	h [m]
Velis Electro	4.280	8.30	11.76	1.150	24.30	0.180	0.0400	0.180
SLSQP	4.236	2.62	3.722	1.708	24.43	0.150	0.0292	0.350
Genetic Algorithm	4.245	2.693	3.821	1.623	24.40	0.159	0.0270	0.350

5

Conclusion and future work

Main goal of the work was to establish the modular pre-sizing framework. Each element of the cooling system has its design and sizing intricacies which might seem easy to describe yet are complicated to implement as a part of a inter-dependent sizing routines and optimizers, often being case specific. That's why the work has concluded with the implementation of detailed integral model of heat exchanger, coupled through CFD with the trumpet shaped diffuser, simplified models of the remaining components and fully operational three different design-optimization routines that have been compared. On the software engineering side, tool allows for relatively easy expansion and calibration of the component physics due to its pipeline architecture.

5.1 Applicability of the tool

The pre-sizing tool was run in two modes: as a design optimizer within a defined design space, and as an analysis of a single configuration.

In optimization/pre-sizing mode, GA proved reliable for identifying a near-optimal layout when considering the lowest-drag objective and can be further refined by adjusting the relative weighting of weight or any other evaluation parameters. In most cases, the overall size of the cooling system differs only slightly from the Pipistrel Velis reference design—especially given the number of assumed input parameters. The greatest deviation occurs in the core height, which is twice that of the original design. This discrepancy likely stems from differences in the actual flow pattern and from the specific fin geometry (data for fins of this size and shape were not available in [23]) used in the Velis heat exchanger. Required heat transfer might also be lower which would result in lighter, smaller designs, like the one discussed during reverse analysis.

SLSQP gives results similar to GA but is dependent on the initial guess due to the multi-modal nature of the cooling system. This approach requires further development in order to reach higher level of reliability.

The analysis of the Velis' system approximation yielded accuracy satisfactory for the pre-sizing tool, yielding the coolant outlet temperature within 1.3°C of the value inferred from real flight data. As mentioned before, this difference might come from all the assumptions on the unknown parameters done throughout the way.

Regarding the hot-day conditions, without transient analysis of coolant temperature inside the loop, only limited simplified analysis is possible for this case. Going from $\Delta T_{ISA} = -5°C$ to $\Delta T_{ISA} = 25°C$ would have to come in as a $30°C$ offset to the coolant temperature flowing in to the radiator, which gives the same temperature difference between air and coolant yielding almost the same heat transfer and $T_{coolant,out} = 54.14°C$ below the limit of $60°C$ stated in engine TCDS [31].

5.2 Further tool development

To increase the accuracy of the tool, more refined models of the inlet, nozzle and outlet can be implemented as well as more HE flow configurations and fin geometries to allow for more layers of the design space analysis. Because increasing the area ratio unavoidably enlarges the frontal area, thereby increasing external installation drag, this aerodynamic penalty should be accounted for within the optimisation loop so that geometrical gains are not pursued at the expense of overall aircraft performance. System- or component-level experimental validation should also be a top priority in terms of future development.

5.2.1 Surrogate-Model Implementations

The interaction between the heat exchanger and diffuser explored in this thesis can be extended by developing surrogate models for other component combinations and their coupled effects. For example, one avenue is to examine different outlet geometries, including variable flap designs that modulate downstream static pressure to establish more favorable pressure gradients within the cooling circuit. Another promising direction is to integrate a fan element, commonly found in aircraft thermal-management systems (as in the Pipistrel Velis Electro), into the surrogate-model framework, enabling rapid assessment of fan performance, placement, and control strategies on overall system behavior. Furthermore, the studies that already have been done, could be continued using more diffusing duct geometries, fine 3D computations, LES turbulence model, or exact HE geometrical model (not porous media source term).

5.2.2 Transient analysis

A logical extension of the present tool is a time and altitude-resolved simulation that follows the loop through an entire mission profile. Such a model would compute the instantaneous heat rejected by every component, include their thermal inertia, interconnecting ducting or adjustable inlet/outlet, tracking the temperature history of each element. To do so it must store the mass and mean specific heat of each component, together with the fluid inventory in the pipes and HE header, so that energy balance can be integrated in time.

5.2.3 Advanced optimization algorithms

The current optimization routines form a solid foundation, but further refinement is possible. Future work should introduce a multi-objective genetic algorithm that optimizes thermal effectiveness, drag, and weight as separate objectives, yielding a Pareto-optimal set of designs. Post-processing selection methods can then identify the preferred solution in a similar but more efficient way than the current parameter-sweep method.

5.3 Experimental Validation

To ensure that the numerical and surrogate models faithfully represent real-world performance, future work should include a targeted experimental campaign. A wind-tunnel rig equipped with interchangeable heat-exchanger cores, diffuser geometries and fan modules would allow systematic measurement of airflow distribution, pressure drop and convective heat transfer under controlled conditions.
Key elements of the experimental program could include:

- **Heat-exchanger core tests:** Characterise pressure-loss and thermal effectiveness over a range of air and coolant mass-flows. Use precision pressure taps and embedded thermocouples to build local correlations for validation and calibration of the tool.
- **Diffuser interaction studies:** Install the diffuser upstream of the core and vary back-pressure (e.g. via adjustable flaps) to quantify its impact on core mass-flow distribution and overall cooling effectiveness. Particle-image velocimetry (PIV) or smoke visualization can reveal separation or recirculation zones.
- **Fan integration experiments:** Incorporate representative fan blades or small electric blower units and measure performance maps (pressure rise vs. flow rate) when coupled to the core–diffuser assembly. This data will inform surrogate models of fan–system matching and control strategies.
- **System-level verification:** Assemble a full cooling-loop prototype and instrument for temperature, flow rate and power consumption. Compare overall cooling capacity and system pressure drop against model predictions across operating points representative of in-flight conditions.

Data from these tests will not only validate the individual component models but also enable refinement of the integrated surrogate framework, reduce model uncertainty and improve confidence in final design recommendations.

Bibliography

[1] NLR (2025), Destination 2050 – Roadmap (NLR-CR-2024-416).

[2] European Commission (2011), Flightpath 2050, Publications Office, doi:https://data.europa.eu/doi/10.2777/50266.

[3] Graver, B., Rutherford, D., and Zheng, S. (2020), CO2 emissions from commercial aviation: 2013, 2018, and 2019, International Council of Clean Transportation report.

[4] Gnadt, A. R., Speth, R. L., Sabnis, J. S., and Barrett, S. R. H. (2019), Technical and environmental assessment of all-electric 180-passenger commercial aircraft, *Progress in Aerospace Sciences*, Vol. 105, pp. 1–30, doi:https://10.1016/j.paerosci.2018.11.002

[5] Wolleswinkel, R. E., de Vries, R., Hoogreef, M. F. M., and Vos, R. (2024), A New Perspective on Battery Electric Aviation, Part I: Reassessment of Achievable Range, in Proceedings of the AIAA SCITECH 2024 Forum (Article AIAA 2024-1489), American Institute of Aeronautics and Astronautics Inc. (AIAA), doi:https://10.2514/6.2024-1489.

[6] de Vries, R., Wolleswinkel, R. E., Hoogreef, M. F. M., and Vos, R. (2024), A New Perspective on Battery-Electric Aviation, Part II: Conceptual Design of a 90-seater, AIAA Scitech 2024 Forum, Orlando, FL, USA.

[7] Perry, D. (2024), Heart reveals ES-30 redesign as it switches to off-the-shelf hybrid powertrain, Flight Global https://www.flightglobal.com/air-transport/heart-reveals-es-30-redesign-as-it-switches-to-off-the-shelf-hyb/rid-powertrain/158291.article

[8] Heart Aerospace, Our mission, https://heartaerospace.com/our-mission/

[9] Heart Aerospace, media bank, https://heartaerospace.com/media-bank/

[10] West S., Curry C. (2022), Decarbonizing Aviation, BloombergNEF

[11] Staack, I., Sobron, A., and Krus, P. (2021), The potential of full electric aircraft for civil transportation: from the Breguet range equation to operational aspects, *CEAS Aeronautical Journal*, Vol. 12, doi:https://10.1007/s13272-021-00530-w.

[12] Hall, D. K., Greitzer, E. M., Dowdle, A. P., Gonzalez, J. J., Hoburg, W. W., Lang, J. H., Sabnis, J. S., et al. (2019), Feasibility of Electrified Propulsion for Ultra-Efficient Commercial Aircraft Final Report, NASA Report CR–2019-220382.

[13] van Heerden, A. S. J., Judt, D. M., Jafari, S., Lawson, C. P., Nikolaidis, T., and Bosak, D. (2021), Aircraft Thermal Management: Practices, Technology, System Architectures, Future Challenges and Opportunities, *Progress*

in Aerospace Sciences, Vol. 128, Article 100767, Elsevier Ltd., doi:https://doi.org/10.1016/j.paerosci.2021.100767.

[14] Asli, M., König, P., Sharma, D., Pontika, E., Huete, J., Reddy Konda, K., Mathiazhagan, A., Xie, T., Höschler, K., and Laskaridis, P. (2024), Thermal management challenges in hybrid-electric propulsion aircraft, *Progress in Aerospace Sciences*, Vol. 144, doi:https://10.1016/j.paerosci.2023.100967.

[15] Coutinho, M. (2023), A review on the recent developments in thermal management systems for hybrid-electric aircraft, *Applied Thermal Engineering*, Vol. 227, doi:https://10.1016/j.applthermaleng.2023.120427.

[16] Gkoutzamanis, V. G., Tsentis, S. E., Valsamis Mylonas, O. S., and Kalfas, A. I. (2022), Thermal Management System Considerations for a Hybrid-Electric Commuter Aircraft, March 17 doi:https://10.2514/1.T6433.

[17] Gibson A.H., Peddie W. (1911), On the resistance to Flow of Water through Pipes or Passages having Divergent Boundaries, University College Dundee.

[18] V. Gnielinski (2013), On heat transfer in tubes, International Journal of Heat and Mass Transfer, https://doi.org/10.1016/j.ijheatmasstransfer.2013.04.015

[19] Idelchik I.E. (2008), Handbook of Hydraulic Resistance 4th Edition Revised and Augumented.

[20] John D. Anderson (2006), Fundamentals of Aerodynamics 4th Edition, McGraw-Hill

[21] John D. Anderson, Jr. (2003), Modern Compressible Flow With Historical Perspective 3rd Edition, McGraw-Hill

[22] Crane Co. (2013), , Flow of fluids through valves, fittings and pipe, Technical Paper no. 41.

[23] W.M. Kays, A.L. London (1984) Compact Heat Exchangers, second ed., McGraw-Hill

[24] Joaquim R. R. A. Martins and Andrew Ning. (2021) Engineering Design Optimization. Cambridge University Press ISBN: 9781108833417.

[25] Rohsenow, Harnett, Cho (1998), Handbook of Heat transfer, McGraw-Hill

[26] International Organization for Standardization (1975), Standard Atmosphere, ISO 2533:1975

[27] Brelje B.J., Jasa J.P., Martins J.R.R.A., Gray J.S., Development of a Conceptual-Level Thermal Management System Design Capability in Open-Concept, University of Michigan Department of Aerospace Engineering and NASA Glenn Research Center.

[28] D. J. Cerantola, A. M. Birk (2015), Experimental Validation of Numerically Optimized Short Annular Diffusers J. Eng. Gas Turbines Power. 137

[29] Coletti, F., Verstraete, T., Bulle, J., Van der Wielen, T., Van den Berge, N., and Arts, T. (2013). Optimization of a U-Bend for Minimal Pressure Loss in Internal Cooling Channels—Part II: Experimental Validation. Journal of Turbomachinery, 135(5), 051016.

[30] Capitão Patrão, A., Jonsson, I., Xisto, C., Lundbladh, A., and Grönstedt, T. (2024), Compact heat exchangers for hydrogen-fueled aero engine intercooling and recuperation, Applied Thermal Engineering 243, 122538.

[31] EASA, Pipistrel Vertical Solutions d.o.o., (2020), Type-Certificate Data Sheet for type E-811 268MVLC Engine, TCDS No.: EASA.E.234 Issue: 01
[32] EMRAX d.o.o., EMRAX 268 Motor Datasheet, https://emrax.com/e-motors/emrax-268/
[33] Pipistrel Velis Electro product's website (accessed 12-05-2025), `https://www.pipistrel-aircraft.com/products/velis-electro`
[34] Pipistrel (2022), Velis Electro Pilot's Operating Handbook, Revision A 01
[35] Pipistrel, Genuine Pipistrel OEM Spare Parts - online interactive spare parts and assemblies catalogue, `https://ipc.pipistrel.si/Shop`, accessed May 2025
[36] Sealand flight school's gallery, `https://www.sealandflight.com/gallery-pipistrel-velis-electro/`, accessed May 2025
[37] Mark Drela (1996),Aerodynamic sof Heat Exchangers for High-Altitude Aircraft, AIAA, Journal of Aircraft Vol. 33, no. 1, p.176-184
[38] Nicholas K. Borer, Trong Bui, Andrew D. Smith (2023), Cruise Propulsion System Thermal Analysis for NASA's X-57 "Maxwell" Mod II Configuration, NASA
[39] ESDU (1976), ESDU 76027 – Introduction to design and performance data for diffusers
[40] ESDU (1987), ESDU 87015 – Performance improvement of axial diffusers for incompressible flow
[41] ESDU (1986), ESDU 86002 – Drag and pressure recovery characteristics of auxiliary air inlets at subsonic speeds
[42] F. M. Rogallo (1941), Report No. 713 - Internal-flow systems for aircraft, National Advisory Committee for Aeronautics
[43] Jesus, A. B., Takase, V. L., and Vinagre, H. T. M. (2004). CFD Evaluation of the Discharge Coefficient of Air Outlets in the Presence of an External Flow. In Proceedings of the 10th Brazilian Congress of Thermal Sciences and Engineering (ENCIT 2004), Braz. Soc. of Mechanical Sciences and Engineering, Rio de Janeiro, Brazil
[44] Metacomp Technologies, ICFD++ User Manual
[45] SciPy documentation - regular grid interpolator `https://docs.scipy.org/doc/scipy/reference/generated/scipy.interpolate.RegularGridInterpolator.html`
[46] SciPy documentation - minimize `https://docs.scipy.org/doc/scipy/reference/generated/scipy.optimize.minimize.html`
[47] DEAP library documentation `https://deap.readthedocs.io/en/master/`
[48] Henk K. Versteeg and Weeratunge Malalasekera (2007), *An Introduction to Computational Fluid Dynamics: The Finite Volume Method*, 2nd ed., Pearson Education Limited
[49] Schubauer, G.B., and Spangenberg, W.H. (1949). Effect of Screens in Wide-Angle Diffusers. NACA Report 949, National Advisory Committee for Aeronautics.
[50] Meredith, F.W. (1935). Note on the cooling of aircraft engines with special references to ethylene glycol radiators enclosed in ducts. British ARC Reports and Memoranda No. 1683, London, England

[51] Rahul Damodhar Rakhade (2012), An Experimental Investigation to Control the Flow Emerging from a Wide Angle Diffuser, K. K. Wagh Institute of Engineering Education and Research

[52] Matweb - Material property data, Aluminum 3003-O properties, https://matweb.com/search/DataSheet.aspx?MatGUID=fd4a40f87d3f4912925e5e6eab1fbc40&ckck=1

[53] Wales, D J, and Doye J P K (1997), Global Optimization by Basin-Hopping and the Lowest Energy Structures of Lennard-Jones Clusters Containing up to 110 Atoms. Journal of Physical Chemistry A 101, 5111.

DEPARTMENT OF MECHANICS AND MARITIME SCIENCES
CHALMERS UNIVERSITY OF TECHNOLOGY
Gothenburg, Sweden 2025
www.chalmers.se

CHALMERS
UNIVERSITY OF TECHNOLOGY